Ramsey Imaging of Optical Dipole Traps

and its applications in building a
3D optical lattice

Dissertation
zur
Erlangung des Doktorgrades (Dr. rer. nat.)
der
Mathematisch-Naturwissenschaftlichen Fakultät
der
Rheinischen Friedrich-Wilhelms-Universität Bonn

von
Gautam Ramola
aus
Ranari, Indien

Bonn, 2021

Angefertigt mit Genehmigung der Mathematisch-Naturwissenschaftlichen Fakultät der Rheinischen Friedrich-Wilhelms-Universität Bonn

1. Gutachter:	Prof. Dr. Dieter Meschede
2. Gutachter:	Prof. Dr. Stefan Linden
Tag der Promotion:	01.09.2021
Erscheinungsjahr:	2021

Abstract

In this work, I present the experimental realization of two-dimensional state-dependent transport of cesium atoms trapped in a three-dimensional optical lattice. Leveraging the ability to state-dependently transport atoms, I demonstrate microwave photon mediated sideband cooling to the motional ground state along two dimensions. Once cooled down to the vibrational ground state, we use these atoms as sensitive probes to detect both magnetic field gradients and optical field inhomogeneities, by means of Ramsey interferometry. This enables us to perform Ramsey imaging of optical dipole traps, an essential technique which helps in the precise alignment of optical beams inside the vacuum cell.

In the first part of the thesis, I introduce the main experimental apparatus of the Discrete Quantum Simulator (DQSIM) machine, as our experiment is known, with emphasis on the technical improvements over the past few years, such as increasing the atom filling in our optical lattice from double digits to a few thousand. Using these atoms as magnetic probes, I confirm the expected magnetic shielding factor of about 2000 from the mu-metal shielding enclosing the vacuum cell. I finally discuss the control we have over the internal state of the atoms, with a measured Rabi frequency of $\Omega \approx 2\pi \times 200\,\mathrm{kHz}$.

In chapter 3, I introduce the concept of state-dependent transport, which forms the basis of most experiments planned with the DQSIM machine. I go on to discuss the polarization synthesizer, the technical backbone of the state-dependent optical lattices. The polarization synthesizer allows us to create any arbitrary polarization state of light, by independently controlling the phase and amplitude of each circular polarization component of a linearly polarized optical lattice beam. With two such polarization synthesizers implemented in the experiment, I report on the experimental realization of state-dependent transport in two dimensions. This is followed by the demonstration of microwave photon mediated ground state cooling in two dimensions, where we achieve a ground state population of about 95% along each dimension.

In the following chapter, I introduce the Ramsey spectroscopy technique, a mainstay of high precision experiments. Using Ramsey spectroscopy, I investigate some sources of dephasing in our experiment, from inhomogeneous magnetic fields to differential light shifts. Based on these Ramsey measurements, I show that we can achieve coherence times greater than a millisecond if we restrict the region of interest in our optical lattice. Exploiting the high precision Ramsey interferometry further, in chapter 5, I introduce a versatile technique for the precise in-vacuo reconstruction of optical potentials. This Ramsey imaging technique is used to image the four laser beams that form our three-dimensional lattice, helping us align them with micrometer precision. In the final chapter, I summarize the work done in this thesis and discuss some future experiments that are planned for the DQSIM machine, from plane selection to two-dimensional quantum walks.

Parts of this thesis will be published in the following article:

[1] G. Ramola, R. Winkelmann, K. Chandrashekara, W. Alt, D. Meschede, and A. Alberti, *Ramsey imaging of optical traps*, Phys. Rev. Applied **16**, 024041 (2021) (10.1103/PhysRevApplied.16.024041)

Contents

"Man masters nature not by force but by understanding. This is why science has succeeded where magic failed: because it has looked for no spell to cast over nature."

— *Charles Brownowski*

CHAPTER 1

Introduction

Quantum mechanics, the fundamental theory describing the microscopic world, has come a long way in the last century, from being a subject of academic interest to becoming a ubiquitous and integral part of our daily life. The first quantum revolution, initiated by our understanding of the laws of quantum physics, led to the development of lasers and transistors, which find applications in smartphones, global positioning systems and magnetic resonance imaging (MRI), to name a few. We are now in the midst of the second quantum revolution, where rather than being spectators to quantum phenomena, we can precisely control and manipulate individual quantum systems [2–4]. Such unprecedented ability to engineer and control quantum systems has led to the creation of a diverse field of quantum technologies, encompassing areas such as metrology [5–8], computation [9–13], and simulation [14–16].

Simulating large quantum systems is a hard task for even the best supercomputers [17]. However, these complex systems can be simulated experimentally using controllable quantum systems [18]. Quantum simulations show promise in addressing questions across many domains of physics, from the microscopic world of condensed matter physics (not accessible via classical computation) to large scale cosmology [19] (not directly tractable in the laboratory). To address questions in condensed matter physics, the simulator should contain many particles (bosons or fermions) that can be confined in some region in space (e.g., optical lattice) [20]. Furthermore, one must be able to initialize the quantum simulator to a known quantum state and then engineer interactions with either external fields or between the different particles. Finally, one must be able to perform a measurement (e.g., fluorescence imaging) to detect the final state of the simulation.

Ultracold atoms in optical lattices are a promising candidate that fulfill the aforementioned requirements for quantum simulation [21–29], having already demonstrated their capability to realize topological systems [30], probe quantum transport [31, 32], and investigate quantum magnetism [33]. Besides this top-bottom approach to addressing physical problems, cold atom systems also show great potential in the quest for building a fault tolerant quantum computer, where a bottom-up approach requires individual control of the quantum state of every atom (or 'qubit') in order to perform operations in a programmable way [34, 35]. Quantum computers will have wide-ranging applications, some of which include drug design and development [36–38], cryptography [39], meteorology [40] and operations research. Currently, the state-of-the-art quantum computers are still Noisy Intermediate-Scale Quantum (NISQ) devices [41] which have been demonstrated on many platforms such trapped ions, superconducting qubits, cold atoms, photons, quantum dots and vacancy centers in diamond [42]. Cold atom based NISQ devices offer several advantages; all qubits are identical, the system is scalable to thousands of qubits [35], individual qubits can be rapidly and accurately controlled using electromagnetic waves [43–47] and precisely detected

using fluorescence imaging [48–51], and most importantly qubits in close proximity do not affect each other's quantum states unless intentionally made to [52, 53]. Such NISQ devices are the stepping stone to building fault-tolerant quantum computers in the future.

To this end, our group has designed and built a two-dimensional (2D) discrete quantum simulator based on an ensemble of cesium atoms. Atoms are trapped and cooled to the vibrational ground state [54] in a 2D spin dependent optical lattice [55–57](see chapter 3). We can control all degrees of freedom of the trapped atoms [58] : their number, position, internal state and vibrational state. A high numerical aperture (NA) objective [59] enables site-resolved imaging and addressing of individual atoms. The novelty of our experiment is the state-dependent transport, whereby atoms in two different internal states can be independently maneuvered in position space. A natural application of the state-dependent lattice, coupled with control over the internal state of the atom, is a quantum walk [60, 61], the quantum counterpart of the classical random walk. Introduced in 1993 by Aharonov et al. [62], quantum walks have piqued the interest of theorists and experimentalists alike [63–66] with applications in quantum simulations (e.g., simulating topological phases [63, 67–69]), quantum search algorithms [70–73] and universal quantum computing [74–76]. With respect to quantum computing, the ability to independently address and steer the qubits on a 2D plane showcases the scope for building programmable quantum circuits [77].

In this work, I present the first experiments demonstrated using the 2D discrete quantum simulator. In chapter 2 I briefly introduce the key components of the experimental setup with emphasis on improvements, such as an enhanced loading of atoms into the optical lattice and a magnetic shielding with a measured suppression of around 2000. In chapter 3, I demonstrate the deterministic state-dependent transport of atoms in two-dimensions with our polarization synthesized optical lattices. Furthermore, I present the measurement of Frank-Condon factors for various openings of our state-dependent lattice, and compare them with theoretical expectations to illustrate the level of control we have over our system. Chapter 3 concludes with the first results of microwave photon mediated sideband cooling along two dimensions, where we cool around 95% of the atoms to the ground state along either direction.

In chapter 4, I discuss techniques to characterize the different dephasing sources in our experiment, from magnetic field fluctuations to inhomogeneous light shifts. Maintaining long qubit coherence is a challenge for quantum simulators and computers alike, since decoherence limits the number of useful operations that can be performed on a quantum system. In chapter 5 I present the results of in-situ Ramsey imaging of dipole traps, where we perform interferometric measurements on atoms in a dipole trap to map out its potential landscape. By performing Ramsey spectroscopy, we are able to precisely measure the vectorial differential light shifts between two hyperfine states as a function of the polarization ellipticity of the dipole beam. Owing to the high precision of Ramsey spectroscopy, we uncover the non-linear response of the atoms to the changing ellipticity caused due to the spatial distribution of the atomic cloud. Ramsey imaging allows us to align the different beams of the three-dimensional lattice with micrometer precision. In the final chapter (chapter 6), I summarize the work done in this thesis and discuss the near term plans with the 2D discrete quantum simulator, from plane selection to two-dimensional quantum walks.

CHAPTER 2

Experimental setup and techniques

Ultimately, the success of quantum technologies lies in our ability to control and manipulate quantum systems, in our case atoms. Needless to say, a significant effort has been put into advancing our experimental setup to improve our control of these quantum particles. Much of this setup has been discussed in the thesis of my predecessor, Stefan Brakhane [78]. In this chapter I will briefly summarize the key experimental components, stressing on the changes made to the previous system. Some of the improvements implemented are the enlargement of the magneto optical trap (MOT) for a higher loading of atoms into the optical lattice (see section 2.2.1), a new laser system for both the optical lattice and the MOT (see section 2.3), and the addition of an electro-optic modulator (EOM) to increase the dynamic range of the intensity locks for the optical lattices.

2.1 Vacuum apparatus

Cold atom experiments are performed in well isolated systems to minimize interactions with the environment, thus giving us greater control. To minimize collisions of atoms with gases present in the atmosphere, these experiments are performed in vacuum conditions, where all unwanted gases are pumped out of the system, leaving only a dilute concentration of the atoms to be probed, in our case cesium atoms.

Besides the requirement for a ultra high vacuum[1] (UHV), atoms also need to interact with a variety of laser beams, requiring that the vacuum system provide direct optical access by featuring many windows. Since light-matter interactions at the atomic level require a fine tuning of the light properties, extra care must be taken to ensure these are not affected by the presence of the viewports. Distortions in the wavefront quality of the laser adversely affect the profile of the optical traps seen by the atoms. Likewise, distortions in the polarization state of the laser beam due to birefringence of the glass cell can lead to unwanted vectorial light shifts [79–81].

Birefringence is particularly detrimental to our experiment since we rely on the precise synthesis of polarization states of the optical lattice beams for transporting atoms (see chapter 3). Incidentally, we measure the vectorial light shifts using atoms to extract the birefringence of two of the windows of the glass cell (discussed in section 4.3.1). For vacuum cell windows, the most dominant source of birefringence is the stress induced birefringence (caused by external stress on the window from mounting screws, pressure differences,and mismatched expansion coefficients of the other vacuum components). Stress-induced birefringence is inhomogenous across the window surface,making it very difficult to

[1] UHV is defined as pressures $<1 \times 10^{-9}$mbar

compensate by feed-forward methods. In order to minimize stress-induced birefringence (while also being compatible with ultra-high vacuum conditions), a state of the art vacuum glass cell with a dodecagonal geometry was designed and built by our group [82]. The windows of this vacuum cell are made of SF57 glass, which exhibits very low stress-induced birefringence. Furthermore, a low outgassing thermally cured epoxy adhesive [2] is used to bind the twelve windows. The vacuum cell sustains a pressure of 3×10^{-10}mbar while the birefringence of each window is $\Delta n < 10^{-7}$.

2.2 Cooling and trapping

2.2.1 Magneto optical trap

The magneto-optical trap (MOT), first demonstrated in 1987 [83], is perhaps the most widely used trap for neutral atoms. Using a combination of magnetic field gradients and optical fields, atoms at room temperature are collected from a dilute background vapour and simultaneously cooled and compressed towards the center of the trap, reaching temperatures below 1 mK and sizes up to a few mm. Working on the principle of Doppler cooling and magnetic trapping, the MOT can keep the atoms confined for long times, making it an ideal source of cold atoms for loading into our optical lattice.

Doppler cooling

Doppler cooling is a mechanism to cool atoms using the radiation pressure of laser light [84]. Proposed in 1975 [85, 86], this technique is widely used since its first experimental realization in 1978 by Wineland et al. [87]. It makes use of the radiation pressure exerted by photons on an atom when they are scattered by it. The scattering rate depends on the detuning to the atomic transition; a smaller detuning leads to an increase in the rate, with the highest scattering achieved for photons that are on resonance. An atom moving towards a red-detuned laser source will experience a frequency closer to resonance, leading to a higher scattering rate. As a result, the atom receives a net momentum kick in the direction of the laser beam since the recoil momenta from the emitted photon averages out to zero. This resultant force can be approximated to have a linear dependence on the velocity, resembling a viscous friction force. The continuous absorption and remission of photons cannot, however, cool the atoms down to 0 K, there is a limit arising from the fact that in the random process of spontaneous emission, the mean squared velocity, $\langle v^2 \rangle$, is not zero. Hence there is always some heating associated with the multiple absorption-emission cycles and the lowest achievable temperature, known as the Doppler temperature T_D, is when the heating and cooling rates are in equilibrium, given by the natural linewidth, Γ, of the transition: $T_D = \hbar\Gamma/2k_B$. For our chosen D2 transition of cesium, Γ corresponds to $2\pi \times 5.2$ MHz resulting in a Doppler temperature of 125 μK. The Doppler temperature is, however, not the lowest achievable temperature in a MOT. When the many sublevels making up an atomic state, and their AC Stark shifts due to the MOT beams are considered, polarization gradient cooling dominates, which allows us to reach temperatures much below the Doppler limit, approaching the recoil temperature [88–90].

Position dependent force

A position dependent force, which pushes the atoms toward the trap center, is realized by introducing a linearly inhomogeneous magnetic field, such as that produced by a quadrupole magnetic field. To understand the working principle, we can consider the 1D case with the transition between $J_g = 0 \rightarrow J_e = 1$ [91]. The magnetic field causes a splitting of the excited state due to the Zeeman effect, as shown in

[2] EpoTek H77

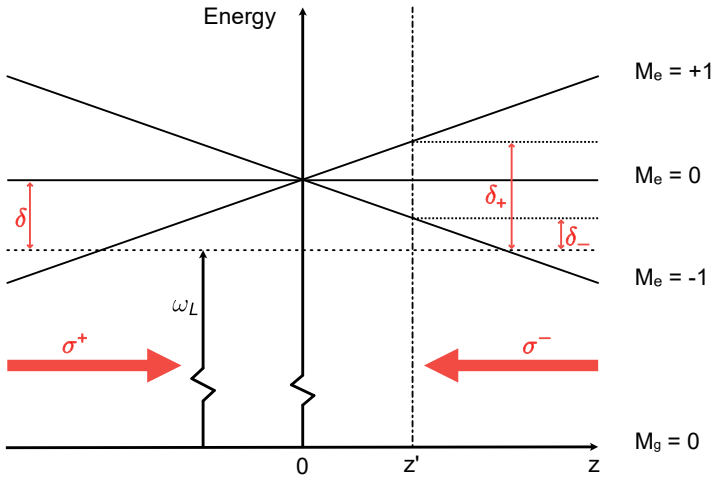

Figure 2.1: Schematic of a MOT in 1D, where ω_L is the laser frequency with a detuning of δ to the $M_g = 0 \rightarrow M_e = 0$ transition. At position z', because of the Zeeman shift in the inhomogenous magnetic field, the detuning δ_- is smaller than δ_+, hence the atom is more likely to scatter photons from the σ^- beam, which pushes it towards the center of the trap.

figure 2.1. The two counter-propagating laser beams are red-detuned and orthogonal in their polarization circularity. At position z', the state $M_e = +1$ is shifted up while the state $M_e = -1$ is shifted down from their energy levels for the magnetic field B>0. Therefore the state $M_e = -1$ is closer to resonance and more likely to scatter photons from the σ^- beam, pushing the atom towards $z = 0$. For $z < 0$ the roles are reversed and $M_e = +1$ is closer to resonance, again leading to the atoms being pushed to the center (this time by the σ^+ beam). This 1D case can be generalized to a 3D case for any $J_g \rightarrow J_e = J_g + 1$ transition, with a pair of counter-propagating beams in each dimension .

MOT setup

The MOT setup consists of three pairs of counter-propagating laser beams that are red-detuned with respect to the D2 transition of cesium. The quadrupole magnetic field is generated by a pair of aluminum coils in anti-Helmholtz configuration, with a resulting field gradient of $9.31 \times 10^{-4}\,\mathrm{T\,cm^{-1}\,A^{-1}}$. In addition, we have three pairs of Helmholtz coils (compensation coils) oriented along the three orthogonal directions. These coils are used for generating a homogeneous bias magnetic field as well as for shifting the trap center of the MOT. All these coils, along with the vacuum cell, are enclosed in a two layer magnetic shielding made of a nickel-iron alloy called Mu-metal, as seen in figure 2.2.

The MOT is created roughly 1 mm below the optical lattice. Once loaded with atoms, it is transported to the position of the lattice by changing the magnetic field strength of the compensation coils along the vertical direction over a duration of 1 ms. This transport is performed in the bright, i.e., the MOT beams are on and continuously cooling during the transport. Transport in the bright requires the MOT beams to be present at both the loading position and the position of the lattice, which is 150 µm away from the surface of the objective lens. Consequently, a portion of the MOT beams clips at the edge of the objective, creating uncontrollable interference patterns at the position of the lattice. To circumvent this problem, the horizontal MOT beams have a knife edge introduced in the beam path, in a 4-f configuration, such that the knife edge is imaged at the position of the objective, hence minimizing any clipping [78].

To enhance the loading of atoms into the lattice (from a few tens to a few thousands), we increased

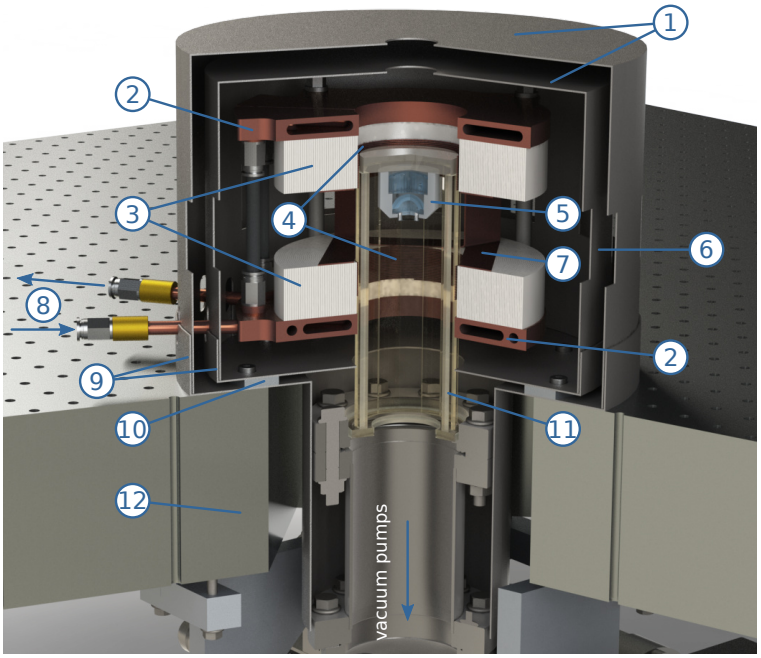

Figure 2.2: A rendering of the cross-section of the mechanical setup. The image is taken from [78], where a detailed description of each element can be found.

the capture range of the MOT. This was done by increasing the beam waist of the MOT from 1.1mm to 4.3mm by changing to a larger collimator[3]. While this was sufficient for the horizontal beams, one of the vertical MOT beams traverses through our objective lens, hence it had to be reshaped in order to have a collimated beam at the position of the MOT. Three 2" lenses were chosen (using a MATLAB based ray tracing software[4]) to shape the MOT beam before it enters the objective so that it is magnified and collimated at the position of the MOT.

2.2.2 Optical molasses - polarization gradient cooling

Once the atoms have been loaded into the optical lattice, two pairs of tightly focused illumination beams are used in the horizontal plane to cool and illuminate the atoms for fluorescence imaging. The illumination beams are overlapped with the horizontal optical lattice beams with customized pickup plates[5](reflectivity of 6 % for both s- and p- polarized light), going through the same optical path as the lattice beams, thereby being tightly focused to a waist of 25 µm in the vertical direction and 75 µm on the horizontal plane. The tight waist and good overlap with the lattice beams ensures that there is no stray light caused by clipping at the objective. The phases of these illumination beams are scrambled with piezo mirrors in order to avoid moire patterns in the images, which occur due to the interference with the lattice beams.

The illuminations beams are in lin⊥lin configuration, creating a spatial polarization gradient along the beam axis. In the absence of a magnetic field, this configuration is well suited for the widely used polarization gradient cooling [89, 92]. Over a distance of $\lambda/2$, where λ is the wavelength of the laser, the

[3] C40APC-B : Thorlabs, Inc.
[4] developed by Dr. Andrea Alberti
[5] Altechna

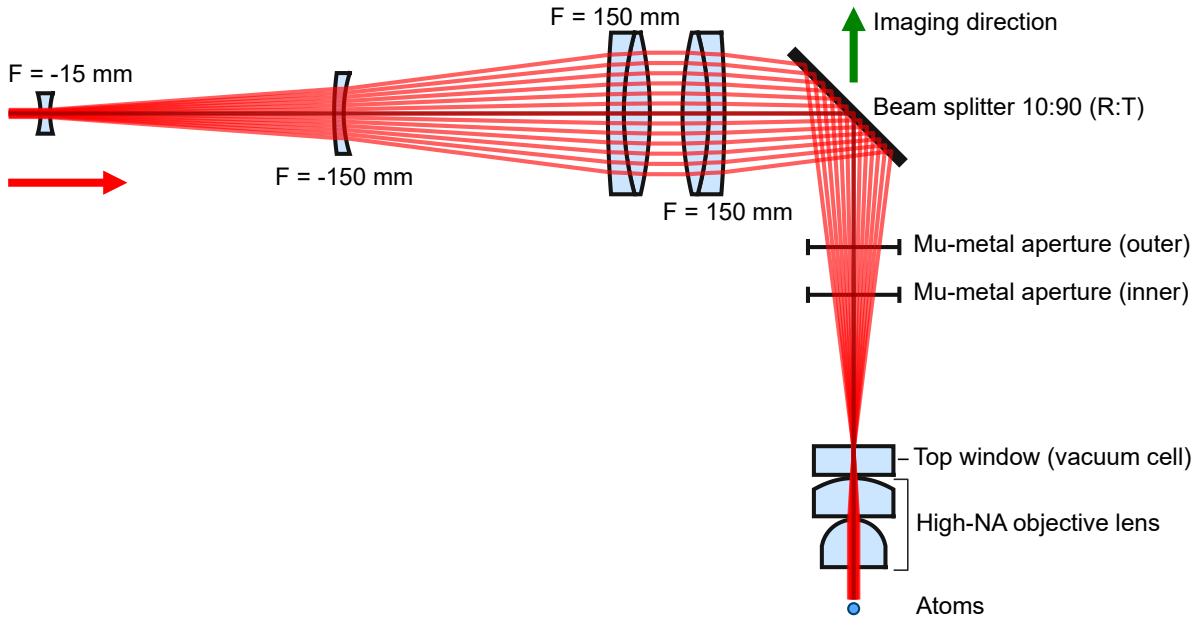

Figure 2.3: A scaled representation of the optical system for the top MOT beam. A collimated beam is sent through a telescope that shapes it in order to compensate for the effect of the objective lens, such that the beam is again collimated at the position of the atoms. The limitation to how large we can magnify the input beam is given by the two apertures of the mu-metal shielding. The ray tracing software developed by Dr. Andrea Alberti was used for choosing the right lens combination, by minimizing the optical wavefront distortion while maximizing the strehl ratio for a given magnification, as well as plotting.

polarization changes from lin$\rightarrow\sigma^-\rightarrow$lin$\rightarrow\sigma^+\rightarrow$lin. As the atoms traverse this region, the energies of the ground-state sublevels oscillate, due to the AC-Stark shift contribution from the different polarizations. As the atom moves out of the local minimum it starts to climb a hill due to polarization gradients in the light fields, resulting in a conversion of its kinetic energy to potential energy. As it approaches the top of the hill, the polarization has changed and a different sub-level is the lowest energy state. The atom is thus pumped into this new low energy state and potential energy it had gained climbing up the hill is radiatively dissipated. Thus the atom is always climbing up hill and losing energy until it is cold enough that it has no energy to climb up the hill. This process is aptly named 'Sisyphus laser cooling', after the greek myth of Sisyphus [93].

2.3 Laser system

The field of experimental cold atom physics largely owes its existence to the continuous development of lasers since the 1960s [94], so much so that the choice of atomic species used in experiments depends on the availability of lasers with the desired wavelengths to drive atomic transitions. For our applications, lasers must have low intensity and phase noise, since both these noise sources contribute to decoherence in our experiments [95]. To that end, we employ state-of-the-art lasers in our experiment, for both the MOT and the optical lattice. These are installed on an optical table (*laser table*), from where optical fibres are drawn over to another optical table (*experimental table*), where the rest of the experiment is situated.

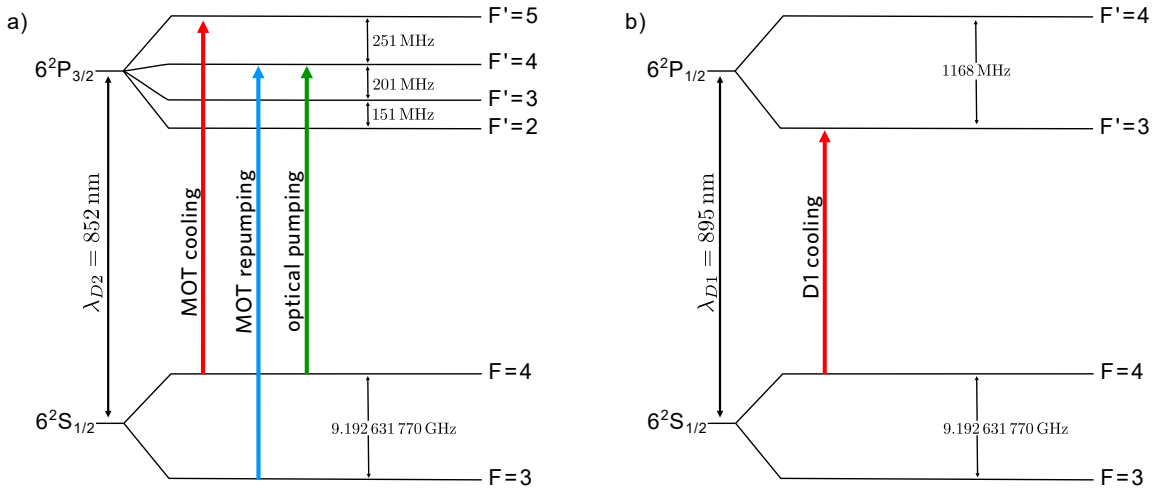

Figure 2.4: A simplified level scheme showing the relevant optical transitions on the a) D2 and b) D1 lines of cesium. The MOT cooling and repumping transitions are used for the MOT as well as the polarization gradient cooling. The D1 cooling line is used to cool atoms along the vertical direction while imaging the atoms. The optical pumping transition is used for preparing atom in the state $|F = 4, m_F = 4\rangle$.

2.3.1 Magneto optical trap laser system

The MOT laser system consists of two lasers tuned close to the D2 line of cesium ($\lambda_{D2} = 852$ nm), one for the cooling transition (*cooler*) and the other for the repumping transition (*repumper*). The *cooler* is red detuned by $\approx 2\Gamma$[6] to the cooling transition (chosen to be $|F = 4\rangle \rightarrow |F' = 5\rangle$, which forms a closed transition). The majority of the cooling laser power is employed for the molasses beams that are used for the MOT. The rest is used for the four beams necessary for polarization gradient cooling (also on the cooling transition) and for the optical pumping beam (which is shifted to the $|F = 4\rangle \rightarrow |F' = 4\rangle$ transition). Although the cooler works on the $|F = 4\rangle \rightarrow |F' = 5\rangle$ transition, occasionally, off-resonant scattering ($|F = 4\rangle \rightarrow |F' = 4\rangle \rightarrow |F = 3\rangle$) will pump atoms into their $|F = 3\rangle$ state. Furthermore, during fluorescence imaging, we use the $|F = 4\rangle \rightarrow |F' = 4\rangle$ transition on the D1 line along the vertical direction, which results in a stronger pumping into the $|F = 3\rangle$ state. In order to bring atoms back into the cooling cycle (and to continually fluoresce), we use the *repumper*, tuned to the $|F = 3\rangle \rightarrow |F' = 4\rangle$ transition, which is overlapped with the MOT cooling beams (a scheme with all the relevant transitions are shown in figure 2.4).

The *repumper* laser is a home-built interference filter laser based on a design reported by Baillard et al. [96], with which we achieve a line width smaller than 10 kHz. A more detailed characterization of this laser design can be found in René Reimann's doctoral thesis [97]. While the *cooler* laser was initially a similar interference filter laser [78], due to the limited output power of around 40 mW, we upgraded to a Ti:sapphire laser (Matisse CR[7]), outputting a power of ≈ 1 W at 852 nm. The Matisse CR is pumped by a 15 W pump laser[8] at 532 nm.

Both the *cooler* and *repumper* are actively frequency-locked to a spectroscopic signal from a polarization spectroscopy setup in a retro-reflected configuration [98–100]. Both these lasers are sent through an

[6] Γ is the natural line width of the D2 transition and corresponds to $2\pi \times 5.22$ MHz.
[7] Sirah Lasertechnik
[8] Millenia 20eV, Spectra Physics

acousto-optic modulator[9] (AOM) in order to control their intensity and frequency. While both the MOT and fluorescence imaging are reasonably insensitive to deviations in the frequency of the *repumper*, the frequency of the repumper plays an important role during microwave mediated sideband cooling, where the light shifts due to the *repumper* can change the optimum cooling frequency of the microwave (see Chapter 3). The AOM also allows for pulse shaping of the beam, essential for operations such as pulsed sideband cooling. The *cooler* intensity and detuning are both fine tuned using the AOM for optimal cooling and imaging. In addition, the AOM is used to tune the cooling laser frequency to the resonance condition for the purpose of state detection, where atoms in $|F = 4\rangle$ are resonantly heated out of the trap, leaving behind the atoms in $|F = 3\rangle$.

2.3.2 Optical lattice laser system

The lattice laser system consists of two lasers, a Ti:Sapphire laser (Matisse CS[10]) for the horizontal lattice, and a high power, single-frequency, continuous-wave solid-state laser (Mephisto MOPA[11]) for the vertical lattice. The Matisse CS is operated at a wavelength of 866 nm and outputs around 6 W of laser light. The Matisse CS is locked to a reference cavity with side-of-fringe locking and the desired wavelength is set while measuring it on a wavemeter[12]. The schematic of the laser distribution for the lattice laser is shown in figure 2.5. After passing through a Faraday isolator[13], a pickup plate[14](R=6%) is used to divert some of the beam for use in the optical phase lock loop (OPLL) system of the lattice (explained in chapter 3). The beam transmitted through the pick-up plate is then sent through an electro-optical modulator (EOM), which is part of an intensity lock loop, used for suppressing laser intensity noise as well as controlling the amount of laser power that is sent to the experimental table. After passing through the EOM, the laser beam is distributed into four paths using half-wave plates and polarizing beam splitters (PBS)[15], with three of the paths corresponding to the three horizontal lattice beams, leading to the optical fibers that go to the experimental table. The fourth path leads to an optical fiber connected to the wavemeter.

2.4 State preparation and manipulation

All experiments we perform are based on the assumption that the atoms are a two-level system, where the two states correspond to $|\uparrow\rangle = |F = 4, m_F = 4\rangle$ and $|\downarrow\rangle = |F = 3, m_F = 3\rangle$. We typically begin by optically pumping the atoms in $|\uparrow\rangle$ using a σ^+ polarized beam tuned to the transition $|F = 4\rangle \rightarrow |F' = 4\rangle$ (see Fig. 2.4). For the σ^+ light, $|F = 4, m_F = 4\rangle$ is a dark state of the optical pumping process, and within a few tens of milliseconds of optical pumping, we are able to pump >99% of the atoms in $|\uparrow\rangle$. The success of optical pumping relies on how pure the σ^+ polarization of the beam is. This depends, in turn, on its circularity (which is measured by means of a rotating polarizer) and how well aligned it is with the quantization axis (which is ensured by adjusting the orientation of the quantization axis using the compensation coils).

Qubit operations are performed by resonant microwaves that are tuned to the resonance frequency (≈9.2 GHz) between the two qubits for a given quantization field strength of 3 G. The microwave radiation is directed at the atoms by a waveguide that is located close to the vacuum cell, inside the mu-metal

[9] AOMO 3080-122, Gooch & Housego
[10] Sirah Lasertechnik
[11] Coherent Inc.
[12] High Finesse
[13] Linos
[14] Altechna
[15] PBS102, Thorlabs Inc.

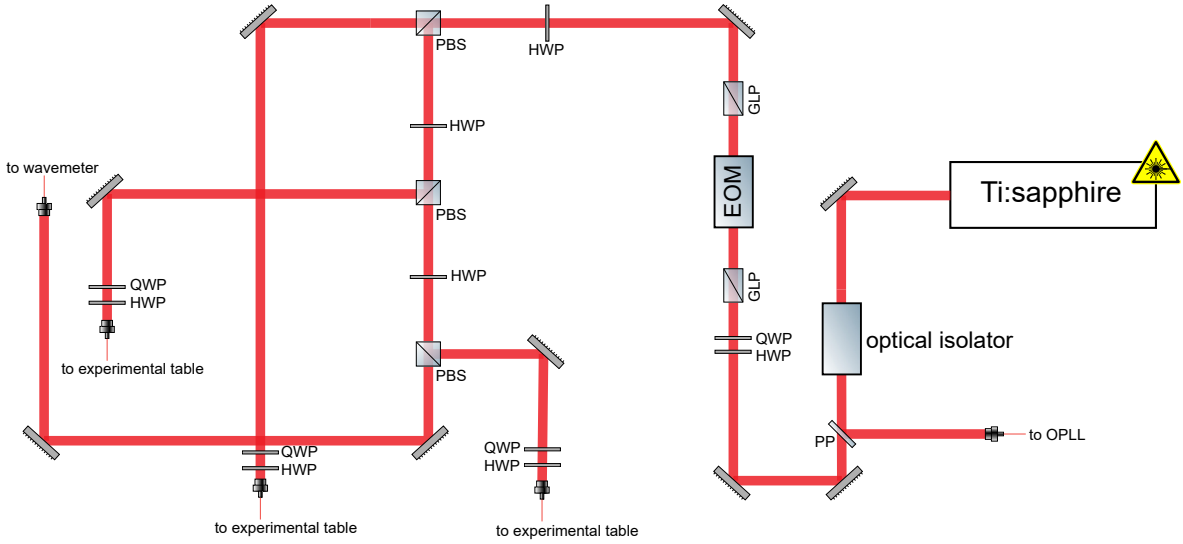

Figure 2.5: Schematic of the laser distribution system for the horizontal optical lattice. The light picked up from the pickup plate (PP) is directed to the optical phase lock setup on the experimental table. The light is picked up before the electro-optical modulator (EOM) so that there is no variation in the intensity of light going to the phase lock. A half-wave plate (HWP) and a quarter-wave plate (QWP) are used in combination to optimize the linearity of the light hitting the glan-laser polarizer (GLP).The EOM is part of an intensity feedback loop used to suppress noise from the laser and also control the light being sent to the experimental table through the three fibers, one for each optical lattice beam. The distribution into the three fiber is done using HWPs and polarizing beam splitters (PBS) as a variable attenuator.

enclosure. Its frequency is generated by mixing the output of a local oscillator[16] running at 9.04 GHz with the output of an arbitrary waveform generator[17](AWG) tuned to 160 MHz. The AWG is used to modulate the frequency and the phase of the microwave signal. The mixed signal is sent through an attenuator (used to turn off the microwave radiation) before being amplified by a high power amplifier to generate the signal with powers up to 41 dBm. The emitted radiation can have any arbitrary time pulse shape defined by the AWG; the primary pulse shapes used in our experiment are the rectangular, Gaussian and the Blackman-Harris.

The microwave operations can be best explained on a Bloch sphere representation [101]. The area under the microwave pulse determines the angle of rotation on the Bloch sphere. In our experiment, there are two important rotations that are widely used, the first is the π-pulse, where the atom in state $|\uparrow\rangle$ is brought to state $|\downarrow\rangle$ and the second is the $\pi/2$-pulse, where the atom initialized in state $|\uparrow\rangle$ is brought to the equator of the Bloch sphere, corresponding to $\frac{|\uparrow\rangle+|\downarrow\rangle}{\sqrt{2}}$. The correct π and $\pi/2$-pulse condition is found by performing Rabi oscillations, as shown in Fig. 2.6(a) where the duration of the microwave is scanned for a fixed amplitude and frequency (which is on resonance). The maximum Rabi frequency achievable in our system is 210 kHz. On fulfilling the π-pulse condition, we are able to completely transfer all atoms from $|\uparrow\rangle$ to $|\downarrow\rangle$, as shown by the microwave spectrum in Fig. 2.6(b).

[16] PLDRO, MITEQ
[17] M3300A, Signadyne

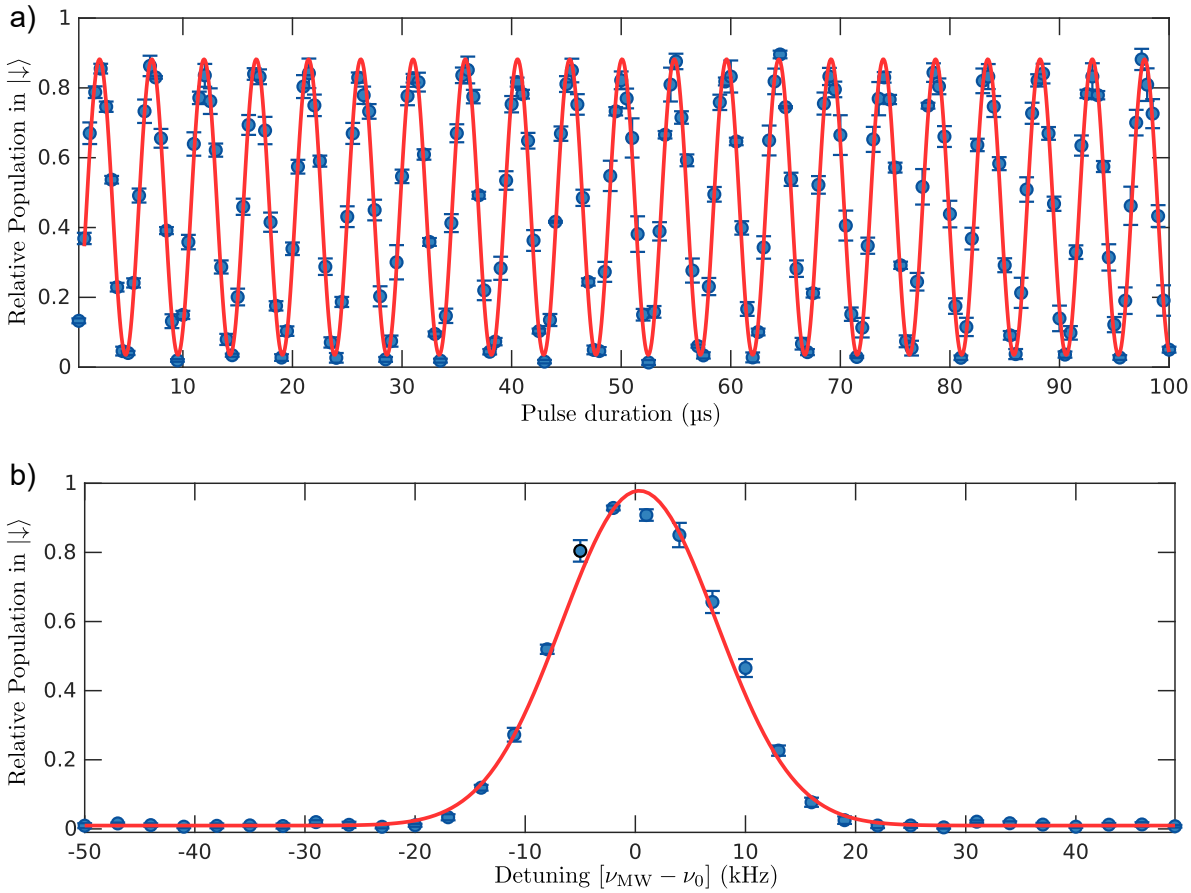

Figure 2.6: (a) Rabi oscillations on between the states $|F = 4, m_F = 4\rangle$ and $|F = 3, m_F = 3\rangle$ using microwaves (see text). The Rabi frequency extracted from the fit (solid red line) is 210 kHz. (b) A microwave spectrum, performed with a Gaussian shaped microwave pulse fulfilling the π-pulse condition. The frequency of the microwave pulse, ν_{MW} is tuned around the resonance frequency ν_0. The solid red line is a fit with a Gaussian.

2.4.1 Magnetic shielding

To maintain long coherence times for a superposition state of our qubits, it is necessary to keep them as isolated from the environment as possible. The vacuum system plays a role in isolating the atoms from other atoms and molecules present in the environment. Likewise, the two-layer shielding in our experiment plays the role of shielding our magnetically sensitive states against stray magnetic fields, that are a dominant source of decoherence [95]. The shielding is made of a nickel-iron soft magnetic alloy called 'Mu-metal', which has a high relative permeability $\mu_r \approx 30,000$. The shielding factor was experimentally measured earlier with a three-axis fluxgate magnetometer Mag-03[18] and a permanent magnet, and found to be $S = 1530^{+1620}_{-100}$ along the transverse direction [78].

We make a more precise measurement by performing spectroscopy on atoms to find out the shielding factor of the two-layer mu-metal shielding. A coil was wrapped multiple times around the experimental enclosure and a current sent through it such that the magnetic field lines cross the experimental setup.

[18] Bartington Instruments Ltd.

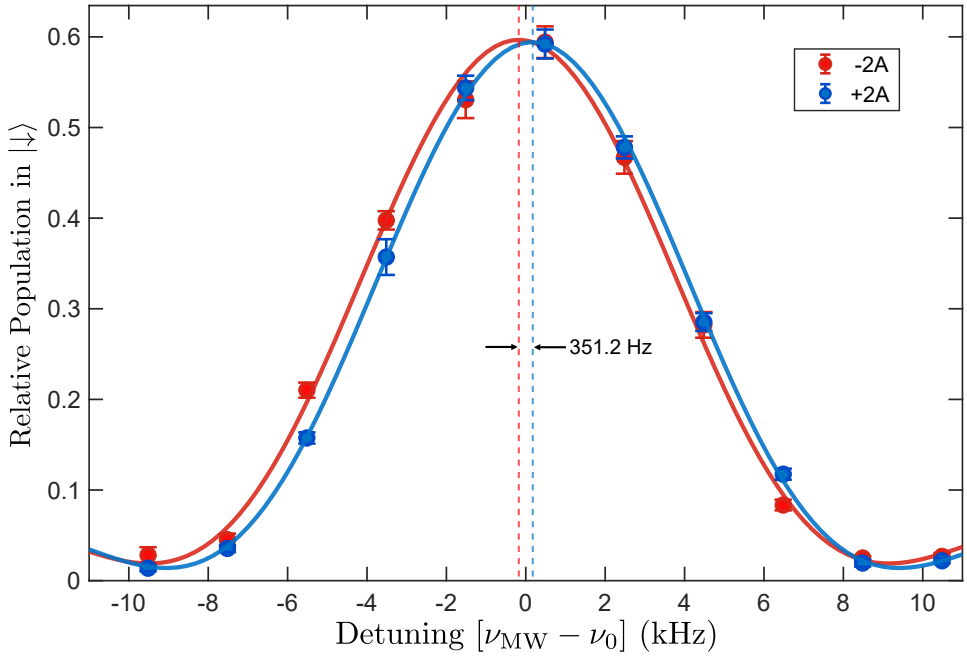

Figure 2.7: Microwave spectra to determine the frequency shift induced by the external magnetic fields to calculate the suppression of the mu-metal shielding. The spectrum is taken while sending 2 A of current clockwise (red) and anti-clockwise (blue) around the experimental enclosure. The magnetic field corresponding to the measured frequency shift of 351.2 Hz (extracted from the Gaussian fits (solid lines) to the data) is compared to the field measured outside the two layer mu-metal shielding (with a fluxgate magnetometer), giving us a suppression of around 2000.

The magnetic field outside the mu-metal shielding is measured using a fluxgate magnetometer FLC100[19] while the magnetic field inside the mu-metal shielding is measured by tracking the resonance frequency shift of atoms, due to the Zeeman effect, using microwave spectroscopy, as shown in figure 2.7. 2 A of current is passed through the coils in both clockwise and anti-clockwise direction, and the shielding factor is calculated by dividing the change in magnetic field measured by the fluxgate sensor by the change derived from the spectroscopy measurements. Reversing the direction of the magnetic field ensures that the suppression is measured only for the known applied field.

The measured frequency difference between the two configurations is 351.2 Hz, as shown in figure 2.7. The frequency shift expected without the mu-metal shielding, derived from the magnetic field measured by the fluxgate sensor, is 714.2 kHz. The transverse suppression of the two-layer mu-metal shielding measured by the atoms is 2035^{+589}_{-374}, compatible with results from simulations of the system [78].

2.5 Imaging system

Imaging atoms in the optical lattice is one of the core steps in our experimental sequences. Both the number of atoms and their positions are crucial information, since they provide insight into the physical processes that occur in an experimental sequence. Recent advancements in the field have enabled the fluorescence detection of single atoms [48, 49, 102–104]. The key component in these experiments,

[19] Stefan Mayer Instruments GmbH & Co.

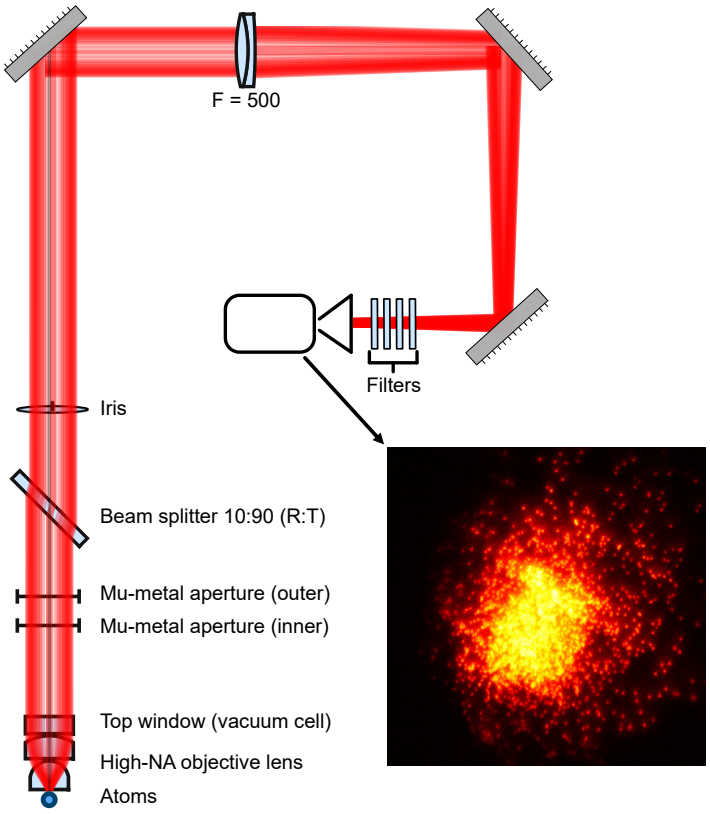

Figure 2.8: Schematic of the imaging setup. Fluorescence collected by the objective lens, at a distance of 150 µm from the the trapped atoms, is transferred through a custom made beamsplitter (transmission of 90% for 852 nm) followed by a motorized iris, before being focused down onto a camera with a lens of focal length $f = 500$ mm. A set of filters are placed in front of the camera to ensure that the light from the vertical lattice (at 1 064 nm) and from the vertical cooling beam (at 895 nm) do not impinge on the camera chip. A typical fluorescence image of atoms trapped in a 3D lattice is shown in the inset, for a reduced numerical aperture of ≈ 0.35.

enabling single atom imaging, is a high resolution optical microscope with a large numerical aperture (NA), typically greater than 0.60. According to the Abbe criterion, the diffraction limit of resolution is $\lambda/2\text{NA}$, where λ is the imaging wavelength. Hence for lattice constants larger than $\lambda/2\text{NA}$, it is possible to achieve single site detection of atoms. While making the lattice constant larger would seem like an obvious solution for single site detection, short lattice constants are desired in most cold atom experiments, for example in experiments that require a large number of atoms for a fixed field of view, or those which rely on tunneling between sites, since the tunneling rate decreases exponentially for larger distances. This makes the development of better microscopes one of the desirable routes of achieving single site resolution. It must be noted, however, that there are techniques of super-resolution microscopy that achieve single site detection even when the lattice constant is smaller than the optical resolution [51]. Not only does a high NA objective lens enable single site detection, it is also used for single site addressing [105, 106]. We have designed a state of the art microscope objective in our group for imaging on the D2 line of cesium (852 nm) with a record NA of 0.92 [59]. This gives us a resolution of 460 nm, well below the lattice constant of 612 nm. Further information regarding the design, assemble and characterization of the objective lens can be found here [82, 107, 108].

The high NA objective lens is installed inside the vacuum cell (see figure 2.2) and has a working distance of 150 µm and a depth of focus ($\lambda/(2\mathrm{NA}^2)$) of ±250 nm. The illumination collected from the atoms is collimated into a beam of diameter 22 mm and sent through a motorized iris IBM 65[20], which is used to control the effective numerical aperture of the system (and hence its depth of focus). The beam is then focused onto an electron-multiplying CCD camera iXon Ultra 897[21] using a lens of focal length $f_{\mathrm{lens}} = 500$ mm (as shown in figure 2.8) that determines what the magnification factor is. Given that the effective focal length of the objective system is $f_{\mathrm{obj}} = 11.96$ mm for our current setup, the magnification is

$$m = \frac{f_{\mathrm{lens}}}{f_{\mathrm{obj}}} = 41.8$$

It must be noted that the imaging system has been designed to have $f_{\mathrm{lens}} = 1{,}250$ mm, however, for all the results shown in this thesis, we have used $f_{\mathrm{lens}} = 500$ mm in order to have a larger field of view of the atoms (100 µm × 100 µm). Furthermore, since the extent of trapped atoms in the vertical direction is greater than the designed depth of focus of the objective (±250 nm), we reduce the iris aperture in order to have an effective numerical aperture of ≈ 0.35. These are the settings we will work with for the entirety of this thesis. Once we have plane selection in along the vertical lattce (as discussed in the thesis of Richard Winkelmann [109]), we will revert back to the settings with NA=0.92.

During imaging, atoms are illuminated by four horizontal beams at 852 nm (set to the $|F = 4\rangle \rightarrow |F' = 5\rangle$ transition) that are overlapped with the optical lattice beams. Two bandpass filters for 852 nm (MaxLine laser[22]) and two notch filters for 1 064 nm are placed in front of the camera in order to suppress stray light (all wavelengths other than 852 nm) from hitting the camera chip.

[20] Owis GmbH
[21] Andor
[22] Semrock Inc.

CHAPTER 3

Transporting atoms in a two-dimensional state-dependent optical lattice

Any application that a cold atom machine is used for, be it quantum simulation [14, 15, 110], quantum computation [111–113], or quantum metrology [114, 115], has a common underlying theme, to quote from Feynmans's prescient talk in 1959 [116] : 'manipulating and controlling things on a small scale'. In the spirit of this endeavor, and based on the theoretical proposals from 1999 [57, 117], coherent transport of atoms based on their internal state (state-dependent transport) was first demonstrated for rubidium atoms by Mandel et al. [56]. Following this first experimental realization, a state-dependent transport scheme for cesium was developed in our group [60]. While transporting neutral atoms has been possible earlier by translating an optical lattice [118], a key improvement has been made in our system to be able to transport atoms over arbitrary distances based on their internal state. This state-dependent transport has opened the avenue for discrete time quantum walks in position space [60], new microwave-mediated resolved sideband cooling techniques [119], and atom interferometry with single atoms [120]. In this chapter, I present the scheme and first results of our state-dependent two dimensional optical lattice, which expands to two dimensions the previous work done in our group [121]. Furthermore, I present the first results of microwave mediated cooling to the vibrational ground state along two axis of the trap and measurements of the Franck-Condon factors, both enabled by the state-dependent transport.

3.1 State-dependent transport

The implementation of state-dependent transport works on the principle that two internal states of the atom (constituting our qubit) interact with two independent optical potentials that can be translated without affecting each other. The dipole potential is created by the ac Stark shift when an atom interacts with the light field. Depending on the detuning of this light field, the potential is either attractive (red-detuned) or repulsive (blue-detuned) [122].

To understand how this vector polarizability dependence on detuning is used to our advantage, we consider the fine structure of the cesium ground state $^2S_{1/2}$, as shown in 3.1a). Our two internal states are denoted by

$$|\uparrow'\rangle = |J = 1/2, m_J = +1/2\rangle \qquad |\downarrow'\rangle = |J = 1/2, m_J = -1/2\rangle$$

In the presence of a light field, the light shifts are dominated by the contribution of the first two excited states $^2P_{1/2}$ and $^2P_{3/2}$, the transitions to which are the D1 and D2 lines, respectively. A linearly polarized laser beam interacting with the atoms, with a wavelength between the D1 and D2 lines, can

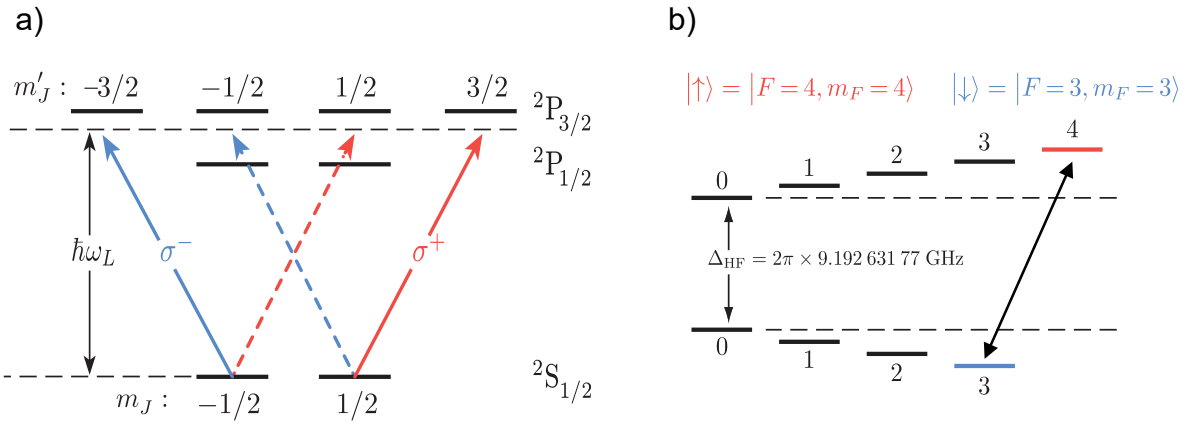

Figure 3.1: (a) Fine structure representation of the cesium ground state. The two colors indicate possible transitions of circularly polarized light at the frequency $\hbar\omega_L$. This frequency is set between the D1 and D2 transitions, such that the potential contributions from the $m_J = \pm 1/2$ magnetic sublevels of the two excited states cancel each other out. (b) The outermost zeeman sublevels of the hyperfine manifold of the cesium ground state are chosen as the two states of the effective two level system with $|\uparrow\rangle = |F = 4, m_F = 4\rangle$ and $|\downarrow\rangle = |F = 3, m_F = 3\rangle$.The degeneracy of the Zeeman sublevels is lifted by applying a magnetic field such that the transition frequency between the two levels is sufficiently far away (>1 MHz) from the other transition frequencies.

be decomposed into a superposition of σ^+ and σ^- polarized light fields. This light field is red-detuned to the $^2S_{1/2} \rightarrow {}^2P_{3/2}$ transition (creating an attractive potential) and blue-detuned to the $^2S_{1/2} \rightarrow {}^2P_{1/2}$ transition (creating a repulsive potential). For a particular wavelength of the light field, termed the 'magic wavelength', the contribution from the excited states with $J = 3/2$ and $m'_J = \pm 1/2$ is canceled out by that of the states with $J = 1/2$ and $m'_J = \pm 1/2$. This leaves the case where the atom in the ground state only sees the potentials created by the outermost states of the $^2P_{3/2}$ excited state. Atoms in the the state $|\uparrow'\rangle$ are trapped in the attractive potential created by the σ^+ light field while atoms in the state $|\downarrow'\rangle$ are exclusively trapped in the optical potential created by the σ^- light field.

In reality, we have to consider the nuclear spin of cesium $I = 7/2$, which results in a hyperfine structure. We use the outermost Zeeman sublevels of the two hyperfine manifolds of the cesium ground state as our qubit in the experiment

$$|\uparrow\rangle = |F = 4, m_F = 4\rangle \qquad |\downarrow\rangle = |F = 3, m_F = 3\rangle \tag{3.1}$$

The two states, when written in terms of the fine structure basis states are

$$\begin{aligned} |\uparrow\rangle &= |I = 7/2, m_I = 7/2\rangle \otimes |\uparrow'\rangle \\ |\downarrow\rangle &= \sqrt{\frac{7}{8}}\,|I = 7/2, m_I = 7/2\rangle \otimes |\downarrow'\rangle + \sqrt{\frac{1}{8}}\,|I = 7/2, m_I = 5/2\rangle \otimes |\uparrow'\rangle \end{aligned} \tag{3.2}$$

From the above relation we can infer that while $|\uparrow\rangle$ has a definite spin orientation, i.e., a defined m_J, the state $|\downarrow\rangle$ is an admixture of both $|\uparrow'\rangle$ and $|\downarrow'\rangle$ with opposite m_J. This means that for the proper detuning of the laser, atoms in state $|\uparrow\rangle$ will only be affected by the σ^+ light field while atoms in state $|\downarrow\rangle$ will see a mixture of the σ^+ and σ^- light fields, with the contribution from σ^- being the dominant one. There is a possibility to choose a detuning such that the state $|\downarrow\rangle$ only experiences the σ^- light field and $|\uparrow\rangle$ experiences an admixture of the two circular polarization components, but there exists no detuning where

the both states can be trapped independently by each of the two circular polarizations [123]. For our experimental setup, we choose a 'magic wavelength' of $\lambda_L = 865.9\,\text{nm}$, where the potentials of the qubit states are

$$\begin{aligned} U_\uparrow &= U_{\sigma^+} \\ U_\downarrow &= \frac{7}{8}U_{\sigma^-} + \frac{1}{8}U_{\sigma^+} \end{aligned} \tag{3.3}$$

The trap depths of the individual lattices created by two circular polarizations are deep enough (~1 MHz) that we can neglect tunneling for our chosen experimental parameters. Furthermore, the traps are sufficiently deep such that when they are translated in position space, the atoms trapped in them can follow along. The cross-talk seen by $|\downarrow\rangle$ from the σ^+ light manifests as a wobbling of the potential $U_{|\downarrow\rangle}$ during transport, however, the detrimental effects of such wobbling, as on the coherence of the state, can be overcome by means of optimal control [124].

3.1.1 State-dependent transport in one dimension

For the sake of simplicity, I will first begin by illustrating the state-dependent transport scheme for the one-dimensional case. In essence, the one-dimensional state-dependent lattice is constructed using two counter-propagating laser beams, where the polarization state for one of the two beams is synthesized by independently controlling the intensity and the phase of the two circularly polarized constituents of the beam. The optical lattice is tuned to the 'magic' wavelength of 866 nm. To create a one-dimensional lattice with control over the two spin-dependent potentials, two co-propagating beams of orthogonal circular polarization (creating a linearly polarized beam) are overlapped with a counter-propagating laser beam that is linearly polarized (which can be decomposed into the σ^+ and σ^- beams with equal amplitude), with the quantization axis defined by a weak magnetic field directed parallel to the lattice axis. The two circular components from each direction interfere to form two sub-lattices, one each for σ^+ and σ^- polarization, and their potential along the longitudinal direction is given by

$$\begin{aligned} U_+(x,\phi) &= U_0 \cos^2(kx + \phi_+) \\ U_-(x,\phi) &= U_0 \cos^2(kx - \phi_-) \end{aligned} \tag{3.4}$$

where $k = 2\pi/\lambda_L$ is the wave-vector of the laser, U_0 is the maximum trap depth, x the position coordinate and $\phi_+(\phi_-)$ is the phase of the $\sigma^+(\sigma^-)$ sub-lattice, respectively. Both of the counter-propagating lasers originate from the output of an optical fiber, ensuring that the transverse profile for both the σ^+ and σ^- sub-lattices is identical and that, therefore, atoms in both $|\uparrow\rangle$ and $|\downarrow\rangle$ see the identical potential in the transverse direction. Along the longitudinal direction, the potentials of the σ^+ and σ^- sub-lattices, although identical in shape, are not constrained in their position: any phase difference between the two circular polarizations would correspond to a relative displacement between the two sub-lattices. Such phase fluctuations typically arise due to environmental disturbances (acoustic and mechanical) and they have to be actively suppressed in order to have a closed lattice (the condition where the two sub-lattices are superimposed over each other). This active stabilization of the phases ϕ_+ and ϕ_- is akin to stabilizing a Mach-Zehnder interferometer, since, as shown in Fig. 3.3, the two orthogonally polarized circular beams are split from a laser beam and then recombined later on before entering the vacuum cell.

We implement an optical phase lock loop (OPLL) to stabilize the phases of the σ^+ and σ^- beams, achieving a relative position stability between the two potentials in the order of ≈1 Å. The phases $\phi_\pm$ of the two circularly polarized beams are independently stabilized against a common optical reference. Furthermore, the OPLL is also used to deterministically translate either of the sublattices by changing

the phases $\phi_{\pm}$, where the distance moved by the potential $U_{\pm}$ is given by

$$\Delta x_{\pm} = \frac{\phi_{\pm}}{2\pi} \times \frac{\lambda_L}{2} \tag{3.5}$$

Therefore, when the phase $\phi_{\pm}$ is changed by 2π, the potential $U_{\pm}$ is translated by one lattice site, $\lambda_L/2$. Since the optical lattice potential is deep, when translated, the atom trapped in it is also carried along with no tunneling effects. The OPLL is further explained in 3.2.1.

3.1.2 State-dependent transport in two dimensions: scheme

State-dependent transport in two dimensions is an extension of the scheme illustrated above. However, the geometry of the two-dimensional lattice is significantly different than in the one-dimensional case. The two-dimensional state-dependent lattice consists of three laser beams, where two of them are counter-propagating (HDT1 and HDT3) and a third is orthogonal (HDT2) to the two, as shown in Fig. 3.2. The counter-propagating beams are polarization-synthesized and the polarization of the third beam is fixed to be linear and perpendicular to the plane in which the three beams traverse. The quantization axis is aligned parallel to the two counter-propagating beams.

Fig. 3.2 illustrates the configuration for the 2D state-dependent lattice. The two synthesized beams, aligned along coordinate x, have wave-vectors $\vec{k}_1$ and $\vec{k}_3$ with controllable phases $\phi_{1,\sigma_+}, \phi_{1,\sigma_-}$ and $\phi_{3,\sigma_+}, \phi_{3,\sigma_-}$ of the circular components, respectively. The orthogonal beam with wave-vector $\vec{k}_2$ is fixed in polarization. There are some features that stand out in this configuration as compared to the 1D case. Firstly, changing the phase $\phi_{1,\sigma_\pm}$ and $\phi_{3,\sigma_\pm}$ of the synthesized beams translates the lattices along y′ and x′, respectively. These coordinates that are rotated by 45° with respect the lattice coordinates y and x. Second, owing to the rotated coordinate system, the lattice constant of the 2D lattice is increased by a factor of $\sqrt{2}$, now corresponding to $\frac{\lambda_L}{\sqrt{2}}$, which means a phase change of $\Delta\phi_{1,\sigma_\pm} = 2\pi$ corresponds to a translation of 612 nm along the y′ axis and a phase change of $\Delta\phi_{3,\sigma_\pm} = 2\pi$ corresponds to a translation of 612 nm along the x′ axis . Lastly, for the same amount of total laser power, the trap depth for the three beam interference is $U_0 = 1.5 \times U_{1D}^0$, where U_{1D}^0 is the trap depth for the 1D lattice.

Intuitively, one can already expect that the two-dimensional potential created by the three beam interference is not isotropic. With all beam intensities being equal, the two counter-propagating beams confine the atoms tighter. As shown in Fig. 3.2, the elliptical trap potential of the 2D lattice has two eigen-frequencies, one along the coordinate x ($\omega_{\text{HDT1-3}}$) and the other along coordinate y(ω_{HDT2}). The Hamiltonian for our system, when all phase angles are set to zero[1], corresponds to

$$H(x,p) = \frac{p^2}{2m_{Cs}} - U_0 \frac{3 + 2\cos(4\pi x/\lambda_L) + 2\cos[2\pi(x-y)/\lambda_L] + 2\cos[2\pi(x+y)/\lambda_L]}{9}, \tag{3.6}$$

where U_0 is the trap depth, λ_L the lattice wavelength, m_{Cs} the mass of the cesium atom, p the momentum, and x and y the position. For atoms confined to the bottom of the trap, we can approximate the individual potential wells to be harmonic, and derive the two trapping frequencies

$$\begin{aligned} \omega_{\text{HDT1-3}} &= \sqrt{\frac{4\pi U_0}{\lambda_L m_{Cs}}}, \\ \omega_{\text{HDT2}} &= \frac{1}{\sqrt{3}}\omega_y, \end{aligned} \tag{3.7}$$

[1] The complete Hamiltonian with the dependence on phase angles is given in Appendix A

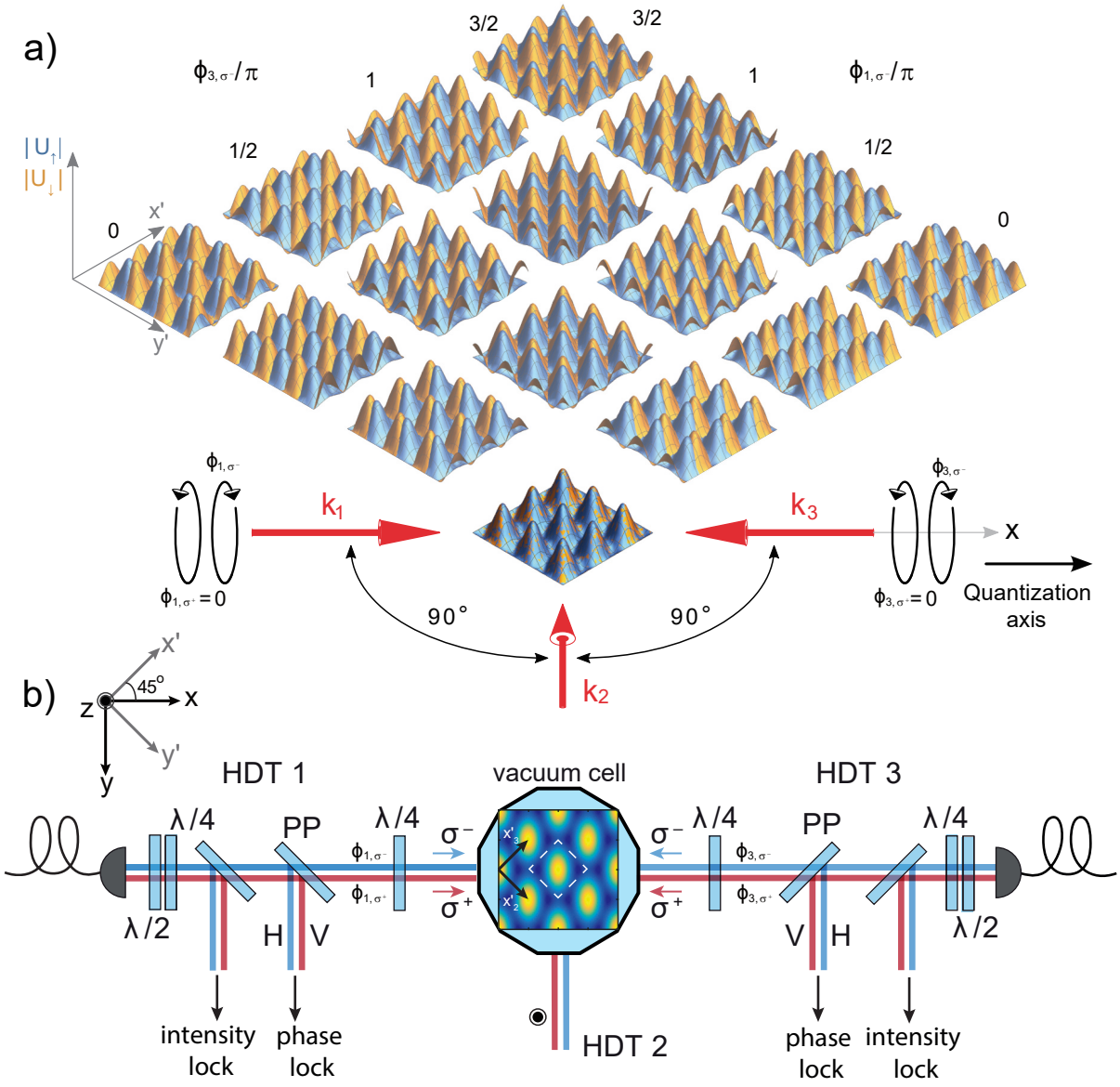

Figure 3.2: a) Two dimensional state-dependent transport scheme. The optical lattice is created by three interfering laser beams (in red), with wave-vectors $\vec{k}_1$,$\vec{k}_2$ and $\vec{k}_3$. This lattice can be decomposed into two sublattices, one created by σ^+ polarized components of the beams to trap $|\uparrow\rangle$ (blue) and the other created by the σ^- components to trap $|\downarrow\rangle$ (orange), with the quantization axis parallel to the two counter-propagating beams. Atoms are trapped in the region of maximum intensity, which correspond to the peaks in the lattice structure. By controlling the phase angles $\phi_{1,\sigma_\pm}$ and $\phi_{3,\sigma_\pm}$ of the circular constituents of the counter-propagating beams, it is possible to traverse the entire 2D plane. This figure adapted from [78]. b) A top-view schematic of the laser setup for the state-dependent lattice. HDT1 and HDT3 are the two polarization synthesized beams. Two orthogonal linearly polarized beams output from the optical fiber are sent through two pickup plates (PP) to reflect off some light for intensity and phase locking. The transmitted beams are sent through a quarter-wave plate to convert them to left and right circularly polarized beams before interfering to form the lattice. HDT2 is vertically linearly polarized. The unit cell is oriented 45° with respect to the laser beam axes. The trapping potential (shown in inset) is elliptical, with a stronger confinement along HDT1-3.

where m_{Cs} is the mass of the cesium atom, U_0 the trap depth and λ_L the wavelength of the optical lattice laser. To displace the potential for $|\downarrow\rangle$ along the direction y (parallel to HDT2), the phases of the two σ^- beams have to be changed in the same direction ($\pm\phi_{1,\sigma^-}$,$\pm\phi_{3,\sigma^-}$) and to displace it along x, the phases of the two σ^- beams have to be changed in opposite directions ($\pm\phi_{1,\sigma^-}$,$\mp\phi_{3,\sigma^-}$).

3.2 Polarization synthesizer

The polarization synthesizer is the key technological development that enables us to have total control over the position and depth of the optical lattice for each circular polarization. A thorough description of the polarization synthesizer, used for the one-dimensional state-dependent lattice, can be found in [107, 121]. In this section, I will briefly describe the polarization synthesizer used in our 2D lattice setup. The polarization synthesis setups for both the beams HDT1 and HDT3 are identical. For creating any arbitrary polarization, we need to control both the intensity and the phase of the circular polarizations that constitute one lattice arm. The chain of elements used for doing so is illustrated in Fig. 3.3, for HDT3. The laser beam is first split into the two orthogonal linear polarizations,vertical(•) and horizontal (↔), using a polarization beamsplitter (PBS). The two beams are sent through acousto-optical modulators (AOMs)[2], with a center frequency of 80 MHz, which can modulate their phase and amplitude. The 1st order of the AOMs output is sent through Wollaston prisms (WP) to further clean the polarizations before being recombined (again using a WP) and coupled into a polarization maintaining optical fiber[3]. The two orthogonal polarizations are coupled into the slow and fast axes of the polarization maintaining fiber. Maintaining the polarization of the light as it is transported in the fiber is essential since we want to have independent control over the two polarizations, and any cross talk in the polarizations will manifest as cross-talk between the σ^+ and σ^- sub-lattices during transport. However, one cannot have zero cross-talk between the two polarizations. We use a combination of $\lambda/2$ and $\lambda/4$ plates to best optimize the incident polarization state entering the fiber in order to limit the cross-talk extinction ratio[4] between the two polarizations to $\approx 10^{-5}$.

At the output of the fiber, a pickup plate (PP[5]) is used to pickup 6% of the incident light (for both • and ↔ polarizations) that is used for the intensity lock. Since the pickup plates are in the path of the optical lattice it is essential that they do not distort the polarization state of the beam passing through. Distortions of the polarization can be caused by stress-induced birefringence on the plates or their mounting angle, which can lead to mixing of the two polarizations. The pickup plates were mounted independently on a test bench setup where the figure of merit used to optimize their mounting was the extinction ratio achieved simultaneously in transmission ($\sim 10^{-7}$) and reflection ($\sim 10^{-6}$) for an incident linear polarization, at least an order of magnitude better than previously achieved (in the 1D State-dependent transport lab). The picked off light is split in the two orthogonal polarizations using a wollaston prism and then focused onto a home-built ultra-low noise amplified photodetector [125]. The photodetector signal is sent to an arbitrary waveform generator and digitizer M3300A[6], with an integrated field programmable gate array[7] (FPGA) that has a programmable digital PID[8]-controller, which then steers the amplitude of the 80 MHz RF signal that drives the AOMs.

[2] AOM 3080-122, Gooch & Housego
[3] P3-780PM-FC-1, Thorlabs Inc.
[4] The cross-talk extinction ratio for a given polarization here is defined as the fraction of the intensity of the beam that is attributed to the other beam.
[5] Altechna
[6] Keysight Technologies
[7] Kintex-7K410T, Xilinx, Inc.
[8] PID : Proportional, Integral, Derivative

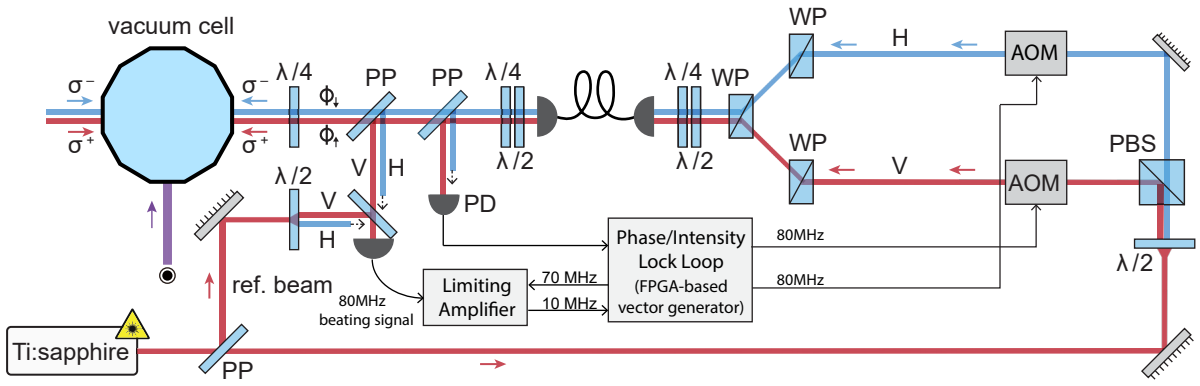

Figure 3.3: Schematic of the polarization synthesizer for one arm of the optical lattice. The output of the Ti:sapphire laser is sent through a pickup plate (PP) to pick off some light to be used as a reference. The transmitted beam is sent through a polarization beam splitter (PBS) to separate out the two orthogonal linear polarizations. Each of these beams is sent through an acousto optical modulator (AOM) before being recombined using a set of wollaston prisms (WP). The AOMs are used to modulate the intensity and phase of these two beams, and they operate at a central frequency of 80 MHz. The recombined beam is sent through an optical fiber to clean the mode and ensure perfect transverse overlap, with the two orthogonal components coupled into the two primary axes of the fiber. The combination of wave plates at the input end of the fiber is used to compensate for any polarization distortion due to the input collimator. Likewise, the wave plates at the output correct distortions caused by the output collimator. The output of the fiber is sent though two pickup plates, the first used for the intensity lock and the second for the phase lock. The light picked up for the phase lock is overlapped with the reference beam and the resulting beat signal detected on a photodiode (PD). The signals of the intensity and phase lock PDs are sent to the FPGA based vector generator, which in turn control the AOMs (more details in the text). The output of the fiber is finally sent through a quarter-wave plate to convert the linear polarization to circular, before entering the vacuum cell through one of the twelve windows. The figure is adapted from [121].

After passing through first pickup plate for the intensity feedback, the lattice is sent through another pickup plate, this one used for picking off light for the optical phase lock. The picked off beam is again sent through a wollaston prism to discriminate the two orthogonal polarizations. Each of the two orthogonally polarized beams is overlapped with a reference beam (that is picked up right at the output of the laser, and hence has not gone through any AOM) and focused onto a fast AC photodetector[9] with a bandwidth of 10 GHz. The photodetector picks up the beat signal between the lattice light and the reference laser beam, which corresponds to the difference of their frequency of around 80 MHz. This beat signal is passed through a bias-tee[10], to remove any DC component, and then amplified by a low noise amplifier[11]. The amplified signal is then fed into a limiting amplifier[12] which fixes the output voltage such that the error signal going to the PID controller does not modulate in amplitude. Otherwise, any change in the amplitude would affect the locking point of the phase feedback system and inadvertently lead to cross-talk between amplitude and phase. The output of the limiting amplifier is sent to a mixer[13], where it is mixed down to 10 MHz using a constant local oscillator frequency of 70 MHz. The 10 MHz signal is sent through a band pass filter[14] and amplified again before being sent to the M3300A module,

[9] G4176-03, Hamamatsu Photonics K.K.
[10] ZX85-12G-S+, Mini-Circuits
[11] ZFL-500HLN+, Mini-Circuits
[12] AD8306, Analog devices
[13] ZX05-1-S+, Mini-Circuits
[14] SBP-10.7+, Mini-Circuits

which implements a digital phase lock loop [126]. The phase lock steering signal controls the phase of the 80 MHz RF signal that drives the AOMs.

3.2.1 Digital intensity and phase control

Intensity and phase locks are required for controlling the trap depth and position of the optical lattice. In our experiment, we switched from analog to digital feedback control for the polarization synthesizer, benefiting from the versatility of the FPGA on the M3300A arbitrary waveform generator [126, 127]. As an example of how digitization is bringing about a change in the landscape of a laboratory, one single chassis containing two FPGAs replaced the nine analog PID controllers[15] and their accompanying electronics. The M3300A module consists of three primary blocks, an input block (digitizers to convert the analog input signals into bits for the FPGA to use), an FPGA (for digital signal processing) and an output block (arbitrary waveform generators, AWGs, that convert the FPGA outputs back into analog waveforms).

The input ports of the M3300A module have analog to digital converters (ADC) with a sampling rate of 100 MSa /s. The ADC is specified to have a resolution of 14 bits although, taking into account the readout noise, the effective resolution is $\approx$ 10.4 bits [127]. This noise of the input block led to the development of the ultra-low noise amplifier photodetector, which amplifies the measured laser noise above the input noise of the digitizer, compensating for the loss of resolution [125]. The digital signal from the input block is subtracted from the setpoint programmed by the user to generate the error signal (as a bitstream). This error signal is processed by the FPGA, where an intellectual property (IP) provided by the manufacturer is used for the PID controller. The FPGA computation adds 8 clock cycles to the feedback loop (1 cycle = 10 ns). The ouput of the FPGA is used to modulate the amplitude of a 80 MHz signal which is then sent to the output block, where a digital to analog converter (DAC) converts the bitstream into an analog 80 MHz RF signal. The DAC has a sampling rate of 500 MSa /s, a resolution of 16 bits and a bandwidth of 200 MHz. Both the input and output blocks introduce delays in the feedback, which amount to a total latency of 453 ns. The theoretical bandwidth of the digital controller is $\simeq$ 1.63 MHz [126]. In the experiment, we have tuned the lock to not be very aggressive, with a bandwidth of a few hundred kilohertz.

For the phase locking scheme, the 10 MHz signal converted by the ADC is sent through a digital phase/frequency discriminator (PFD), which compares the phase against an internal reference running at 10 MHz. The output of the PFD is the error signal that is sent to the digital PID IP, which further controls the phase of the RF output signal. The digital signal processing for the phase lock takes more time than the intensity lock scheme since the number of bits used in the FPGA is longer (meaning more clock cycles) and some operations in the signal processing (fast Fourier transform) are not performed in parallel, hence the bandwidth is lower. However, for both the phase and intensity lock, feedforward control can dramatically increase the bandwidth of the system [126]. The idea here is that if the system response is known, one can compensate it in real-time such that the dead time in the feedback loop can be removed when the system responds to change. Experimentally, we have been able to boost the intensity and phase lock bandwidth to $\simeq$3 MHz.

Intensity and phase noise

In addition to controlling the trap depth and position of the optical lattice, the intensity/phase lock play an important role in suppressing noise. For our setup, noise can be of two types, either common-mode (where both σ^+ and σ^- beams have the same noise profile) or differential noise (where the noise for the

[15] D2-125, Vescent Photonics

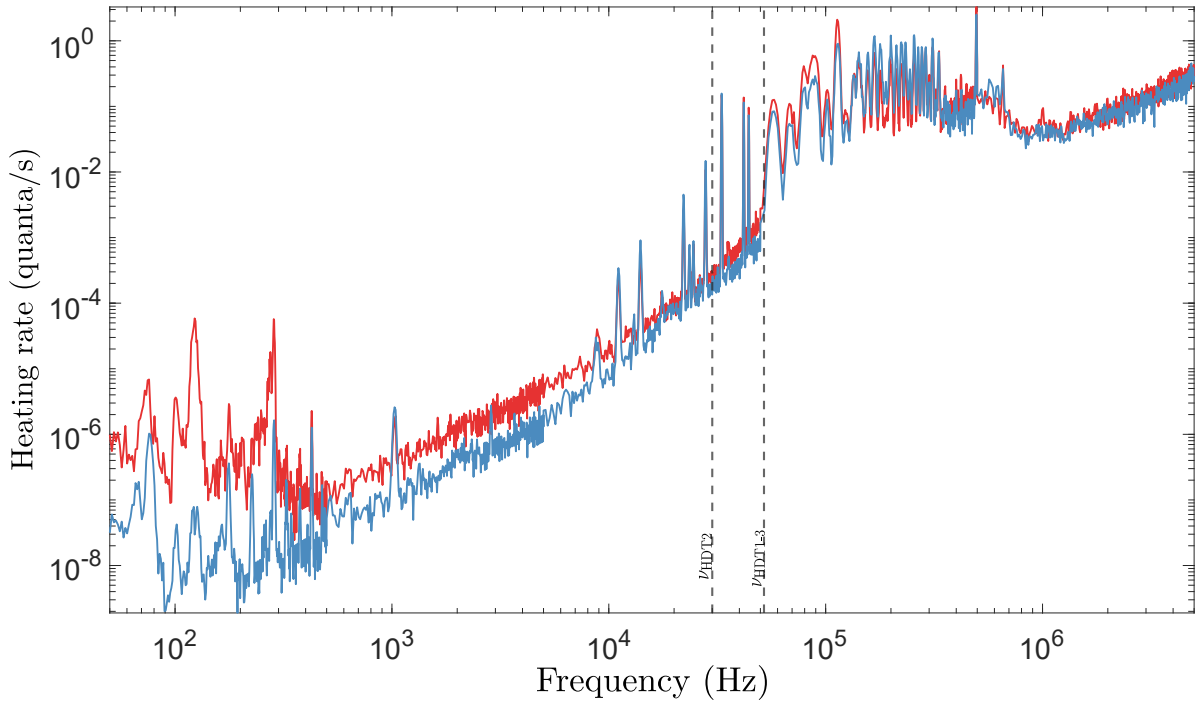

Figure 3.4: Heating rate contribution from the intensity noise of the σ^- component of the beam HDT1 (red) and HDT3(blue). The intensity signal is recorded by a photodiode and Fourier analyzed using a spectrum analyzer. The intensity noise power spectrum is converted to a heating rate following the model in [107]. The vertical dashed lines correspond to the trap frequencies, where the heating contribution is most relevant to our experiment. The heating contribution from the two beams is of the order of 10^{-4}quanta/s.

σ^+ and σ^- beams are independent of each other). Both common-mode and differential intensity/phase noise have a detrimental effect on the coherence of the atoms, as explained in [95]. Furthermore, phase noise manifests as a shaking of the lattice, with a possibility of resonantly heating the atoms out of the lattice [128, 129]. This is a parametric heating process, so the heating rate depends on the second harmonic of the trap frequency.

As discussed by Robens et al. [121], these fluctuations in the intensity and phase of the individual σ^+ and σ^- beams can be interpreted as a reduction in the degree of polarization of the optical lattice, which means a lower extinction ratio, ξ_{ext}, achievable with the polarization synthesizer. The extinction ratio can be related to the differential intensity noise by the following relation:

$$\xi_{ext} \approx \left(\frac{\Delta I}{2I}\right)^2 \tag{3.8}$$

where

$$\frac{\Delta I}{I} = \frac{I_+ - I_-}{I_+ + I_-} \tag{3.9}$$

Similarly, the extinction ratio is related to the phase noise by

$$\xi_{ext} \approx \frac{(\Delta\phi)^2}{4} \tag{3.10}$$

where $\Delta\phi = \phi_+ - \phi_-$, is the total differential phase noise within a given bandwidth. The differential phase is measured by installing a polarizer at 45° with respect to the polarization of the lattice beam. Intensity fluctuation in transmission can be attributed to the relative phase fluctuations between the σ^+ and σ^- components of the beam. Both intensity and phase noise contributions in our setup are compatible with the values presented in [121].

We perform an intensity noise measurement of each circular component of the synthesized lattice beams. Following [107], we convert the measured intensity power spectral density to a heating rate, as shown in Figure 3.4, for the σ^- component of HDT1 and HDT3. The heating contribution from the intensity noise is negligible, below 10^{-3} along both directions.

3.3 Experimental realization of two-dimensional state-dependent transport

In this section, I will present the results of the first experimental realization of transport in our experimental setup. All sequences in our experiment begin with loading atoms from the MOT to the optical lattice followed by polarization gradient cooling (see sec. 2.2.2). The atoms are then imaged in order to record their initial position. Following this, the atoms are prepared in $|\uparrow\rangle$ state by means of optical pumping (see sec. 2.4). To demonstrate state-dependent transport, only the σ^+ lattice is translated while the σ^- lattice is kept stationary. As shown in Fig. 3.5(a)-(h), the trajectory programmed is octagonal in shape. The orientation of the laser beams in marked in Fig 3.5(a). Atoms are translated along HDT1-3 (Fig. 3.5(b)) by synchronously changing the phase of the σ^+ components of both HDT1 and HDT3 beams in the same direction. The phase is ramped up by $2\pi \times 20$ radians over a millisecond corresponding to a distance of around 17 µm. In Fig. 3.5(c) only the σ^+ sublattice of HDT3 beam is translated, this moves the atoms along the lattice axis. Since atoms are imaged after every transport step, they can be scattered into other zeeman sublevels of both $|F = 4\rangle$ and $|F = 3\rangle$. Hence after every intermediate imaging step, the atoms are optically pumped back into $|F = 4, m_F = 4\rangle$. The transport along the octagonal geometry demonstrates that the atoms can be transported along any arbitrary direction on the 2D plane. Although Fig. 3.5 is a demonstration of state-dependent transport, to the skeptic, there is no clear evidence of the 'state-dependence'. In order to show that the two states can independently be transported, we perform a transport sequence where the $|\uparrow\rangle$ state and $|\downarrow\rangle$ state are transported in orthogonal directions, as shown in Fig 3.6. Currently we still have not implemented single site addressing of atoms [58], so we prepare the atoms in $|\uparrow\rangle$ and then wait for a certain duration for the population to have relaxed to a mixture of $|\uparrow\rangle$ and $|\downarrow\rangle$.

3.4 Cooling to the vibrational ground state

The first application leveraging our ability to state-dependently transport atoms is to cool them to the motional ground state. Atoms loaded into the optical lattice are initially cooled by polarization gradient cooling, bringing their temperature down to ~6 µK. At these temperatures, atoms still occupy higher vibrational states. When an ensemble of atoms trapped in an optical lattice occupy different vibrational states, they experience different shifts in their atomic resonance due to their interaction with the light field. These differential light shifts are a source of decoherence [130]. Furthermore, atoms that occupy different vibrational states are not *indistinguishable*, a requirement for various experiments, particularly those involving interferometry. These are some of the few considerations that necessitates motional control of atoms in the optical lattice.

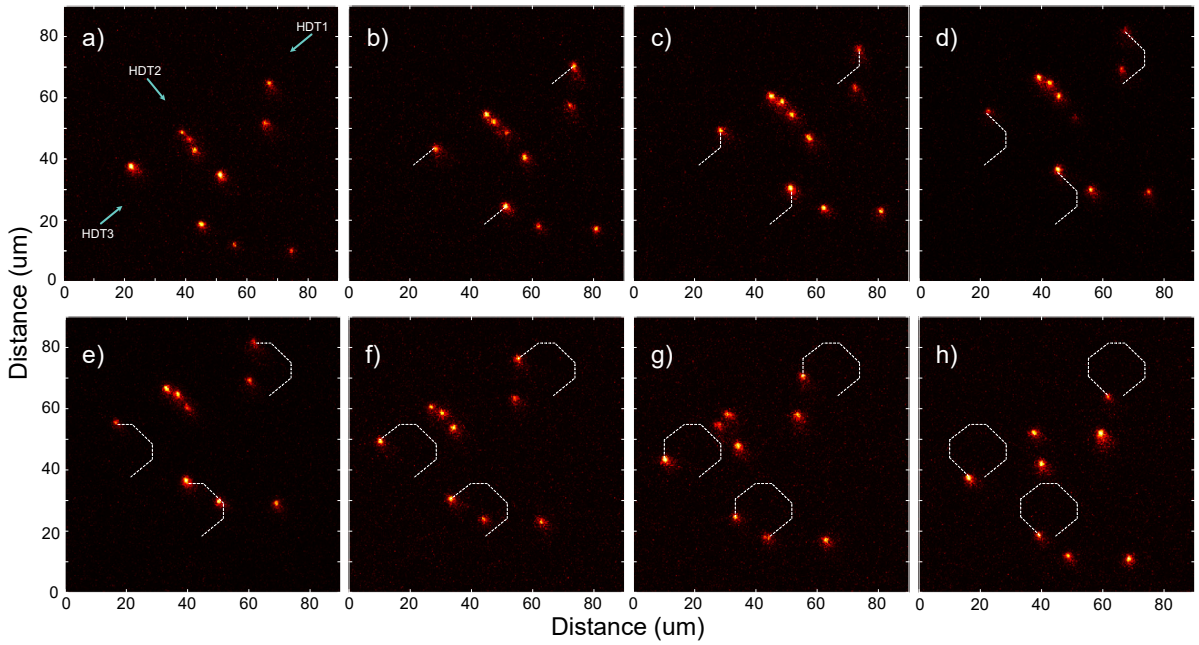

Figure 3.5: a)-h) State-dependent transport of $|\uparrow\rangle$ atoms along an octagonal trajectory, highlighted for three atoms. During this transport sequence over a few seconds, some (hot) atoms hop to neighboring sites and some are lost due to background collisions. The orientation of the three lattice beams is marked in a). All atoms are initialized to $|\uparrow\rangle$ before translating the σ^+ lattice, while the σ^- lattice is kept stationary.

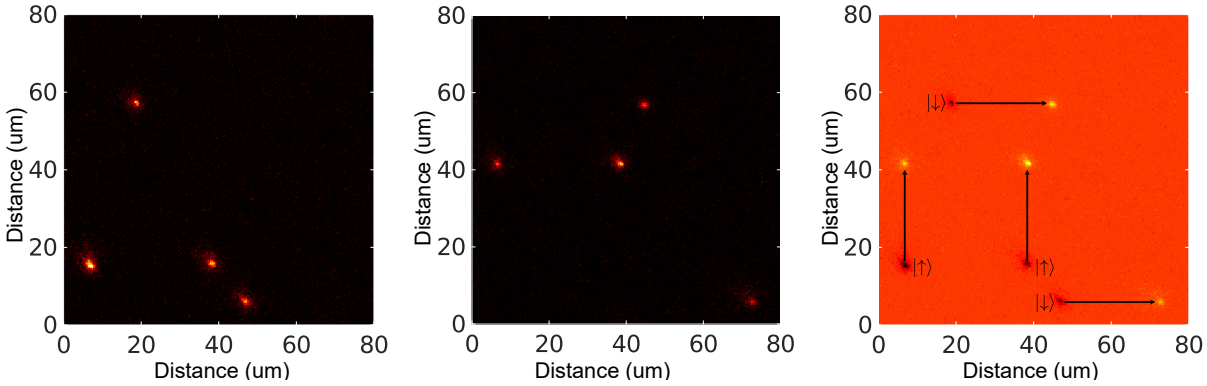

Figure 3.6: (a) The initial position of atoms after very sparse loading into the lattice. (b) Image of transported atoms. Atoms in state $|\uparrow\rangle$ are translated upward by 40 lattice sites upwards while atoms in state $|\downarrow\rangle$ are transported 40 lattice sites to the right. (c) shows the difference image ((b)-(a)) to highlight the transport.

Over the years, new techniques have been developed for cooling atoms to the vibrational ground state. Approaches include evaporative cooling, used to create BECs that transition to a Mott insulation state in a lattice [48, 105], resolved-sideband Raman cooling, where Raman coupling between the different vibrational states is utilized [131–135], and finally sideband-resolved microwave cooling, where the development of state-dependent potentials has enabled the use of microwaves to couple the different vibrational states [119, 136]. In this this section I will report on the sideband-resolved microwave cooling along the two dimensions in the horizontal plane. Along the vertical direction, we perform sideband-resolved Raman cooling, details of which can be found in [109].

3.4.1 Microwave mediated coupling of vibrational states

A typical microwave spectrum on the carrier transition has been shown is section 2.4, corresponding to the transition

$$|\uparrow, n\rangle \rightarrow |\downarrow, n\rangle$$

where $|\uparrow\rangle = |F = 4, m_F = 4\rangle$, $|\downarrow\rangle = |F = 3, m_F = 3\rangle$ and n is the vibrational level. For cooling atoms, the microwave has to drive the transition $|\uparrow, n\rangle \rightarrow |\downarrow, n'\rangle$, where $n' < n$. The two vibrational levels n and n' are orthogonal to each other, which means that the overlap integral $\langle\downarrow, n'|\uparrow, n\rangle$ is zero. To have a non-zero overlap, the orthogonality needs to be broken. For resolved Raman sideband cooling, this is done by the momentum shift operator, such that the transitions matrix element is proportional to $\langle\uparrow, n|e^{i\vec{r}\Delta\vec{k}}|\downarrow, n'\rangle$ where $|n\rangle$ and $|n'\rangle$ are the initial and final states, and $\Delta\vec{k}$ is the difference in the wavevectors of the two raman beams, oriented along $\vec{r}$. However, compared to the optical photons, a microwave photon has a large wavelength, of around 32 mm. This renders the microwave photon useless for momentum transfer when the two states $|\uparrow\rangle$ and $|\downarrow\rangle$ experience an identical potential:

$$\langle\uparrow, n|e^{i\vec{r}\Delta\vec{k}}|\downarrow, n'\rangle \approx \langle\uparrow, n|\downarrow, n'\rangle = 0 \tag{3.11}$$

In order to enable a microwave mediated sideband transition, we need to break the orthogonality between the two vibrational states by displacing them in position space. For a shift of Δx, the position shift operator is given by

$$\hat{T}_{\Delta x} = e^{-i\hat{p}\Delta x/\hbar} \tag{3.12}$$

where $\hat{p}$ is atom's momentum operator and $\hbar$ the reduced Planck constant. The overlap integral between the displaced states can be written as

$$I_n^{n'}(\Delta x) = \langle\uparrow, n|\hat{T}_{\Delta x}|\downarrow, n'\rangle \tag{3.13}$$

where $I_n^{n'}(\Delta x)$ is the Franck-Condon factor, widely used in molecular physics, which determines the coupling strength of the different vibrational transitions. In contrast to the Raman technique where the atoms are cooled by transfer of kinetic energy (momentum kick), the microwave sideband cooling technique dissipates energy by transferring potential energy by the displacement in positions space. The displacement operation is well suited to our experiment, since we can independently translate the potentials for $|\uparrow\rangle$ and $|\downarrow\rangle$ with nanometer precision.

3.4.2 Measuring Franck-Condon factors

The coupling strength between the vibrational states can be tuned by controlling the displacement Δx between the potentials. The Franck-Condon factors relate the Rabi frequency of the carrier for $\Delta x = 0$

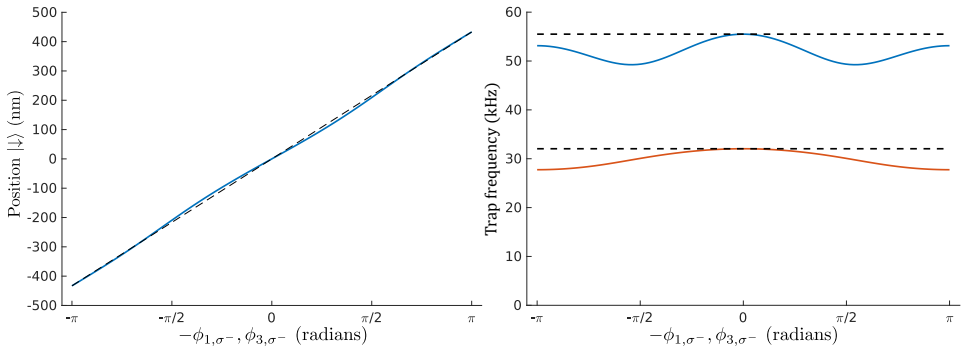

Figure 3.7: a) The non-linear trajectory of the potential for $|\downarrow\rangle$ as it is transported along HDT1-3 by simultaneously changing the phases ϕ_{1,σ^-} and ϕ_{3,σ^-}. The dotted line is plotted to emphasize the non-linearity. b) The corresponding variation in the trap frequency along HDT1-3 (blue) and HDT2 (orange) as the $|\downarrow\rangle$ lattice is translated.

$(n \rightarrow n)$ to that of the sideband for a given Δx $(n \rightarrow n')$ [137] :

$$\begin{aligned} \hbar\Omega_{R_{n,n'}} &= \langle F', m_F', n'|\hat{H}_F e^{-i\hat{p}\Delta x/\hbar}|F, m_F, n\rangle \\ &= \langle F', m_F'|\hat{H}_F|F, m_F\rangle \langle n'|e^{-i\hat{p}\Delta x/\hbar}|n\rangle \\ &= \hbar\Omega_{bare} \times I_n^{n'}(\Delta x) \end{aligned} \tag{3.14}$$

where $\hat{H}_F$ is the atom field interaction hamiltonian that acts on the internal degrees of freedom (F and m_F) and that gives us the bare Rabi frequency, Ω_{bare}, between the two states, in our case $|\uparrow\rangle$ and $|\downarrow\rangle$. $\Omega_{R_{n,n'}}$ is the Rabi frequency of the sideband transition. The ability to tune the Franck-Condon factor with relative ease in our experiment is in stark contrast to setups using Raman lasers for sideband spectroscopy, where the angle between the laser beams has to be changed to change the Franck-Condon factor.

We tune the Franck-Condon factors by displacing the lattice along the directions x_2 (along HDT2) and x_3 (along HDT1-3), see Fig. 3.2. The measurement begins with taking a microwave spectrum to determine the resonance frequency of both the sideband transition and carrier transition as a function of displacement. Due to the cross-talk between the σ^+ and σ^- polarizations for the $|\downarrow\rangle$ potential, the trap frequencies for $|\downarrow\rangle$ change as the potential is translated, as shown in Fig. 3.7(b). The displacement is computed based on the phase of the lattice. Changing the phase of the two counter-propagating synthesized beams by 2π, translates the potential to by λ_L. However, it must be noted, as shown in Fig. 3.7(a), that the distance translated by the potential doesn't scale linearly with the phase.

The trap frequencies for the trap depth we work at are ~ 55 kHz (along HDT1-3) and ~ 32 kHz (along HDT2). In order to ensure that the Rabi oscillation we measure for the sidebands do not include any carrier transitions due to broadening, we make sure that the Rabi frequency is lower than the trap frequencies. Hence, all the measurements are taken with a reduced microwave amplitude, such that the Rabi frequency of the carrier is around 12 kHz. Fig. 3.8 shows a Rabi oscillations for 1st order sidebands along HDT1-3 and HDT2. The signal is fitted with the following function [137] :

$$P_{|\downarrow\rangle}(t) = A_0(1 + \exp(-\sqrt{t/\tau_{\text{decay}}})\sin(\Omega_{R_{n,n'}}t + \phi_{\text{offset}})) + bg \tag{3.15}$$

where $P_{|\downarrow\rangle}$ is the population in state $|\downarrow\rangle$, τ_{decay} is the decay constant of the Rabi oscillations with frequency $\Omega_{R_{n,n'}}$. From the measured Rabi frequencies we can extract the Franck-Condon factors for lattice openings in the two orthogonal directions, shown in Fig. 3.9. The data, in figure 3.9, is in good agreement with the

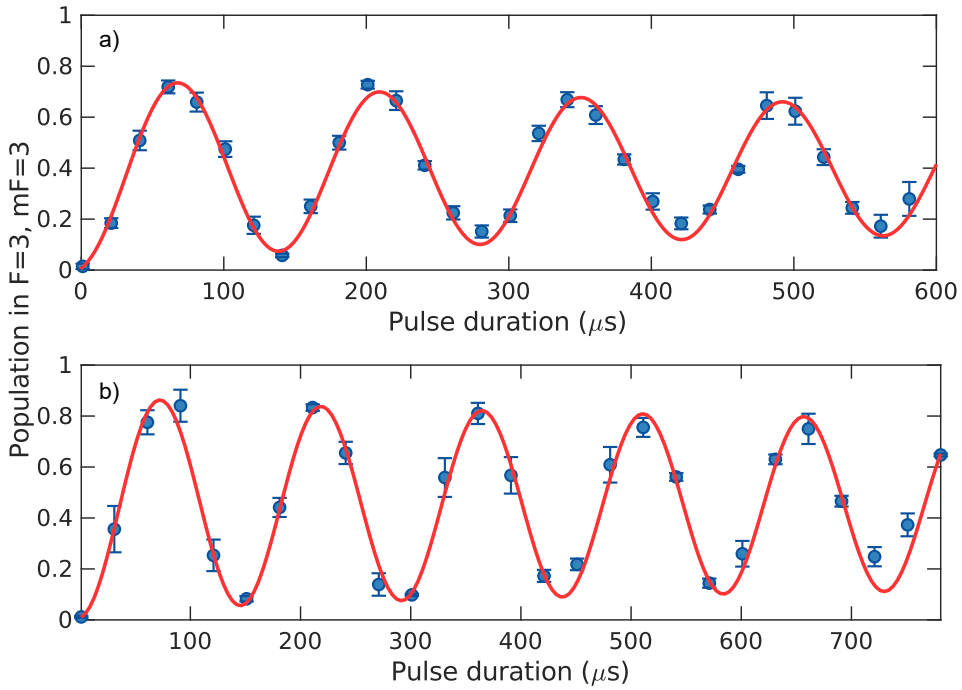

Figure 3.8: Rabi oscillations on the sideband transitions $|\uparrow,0\rangle \leftrightarrow |\downarrow,1\rangle$ fitted with equation 3.15 (solid red lines). a) The σ^- lattice is displaced along HDT1-3 with phase ϕ_{1,σ^-} and $-\phi_3,\sigma^-$ set to 28.8°, corresponding to $\Delta x_{\text{HDT1-3}} = 61.34$ nm. The Rabi frequency measured is $2\pi \times (7.1 \pm 0.03)$ kHz. b) The σ^- lattice is displaced along HDT2 with phase ϕ_{1,σ^-} and ϕ_3,σ^- set to 28.8°, corresponding to an opening $\Delta x_{\text{HDT2}} = 53.20$ nm. The Rabi frequency measured is $2\pi \times (6.8 \pm 0.02)$ kHz.

theoretical prediction of the Franck-Condon factors for our 2D lattice geometry, which accounts for the change in the depth of the potential $U_{|\downarrow\rangle}$ and the non-linear dependence of Δx on the polarization angle, shown in Fig. 3.7.

While the depth of $U_{|\uparrow\rangle}$ remains constant for the translation of the potentials, the trap depth $U_{|\downarrow\rangle}$ becomes shallower as the potential is displaced. This means that the resonance condition of the carrier is red-detuned to that when the lattice is closed. The resonance frequency of the carrier and the 1st order transition along the direction HDT1-3 are plotted in Fig. 3.10. The measured shift agree very well with the theoretical calculations, allowing us to confidently use the theoretical model for calculating the Franck-Condon factors for the higher order transitions.

3.4.3 Sideband resolved microwave cooling

The concept of microwave photon mediated coupling between the vibrational states has been introduced in 3.4.1. With the knowledge of the Franck-Condon factors for the different transitions, we are equipped with the tools to perform sideband cooling using microwaves. In this section, I will introduce the experimental procedure for sideband-resolved microwave cooling and show the results we have achieved with our setup so far.

After polarization gradient cooling of the atoms trapped in the lattice, they occupy the first ten vibrational states. The atoms are then optically pumped to the $|\uparrow\rangle$ state (explained in 2.4). The lattice is

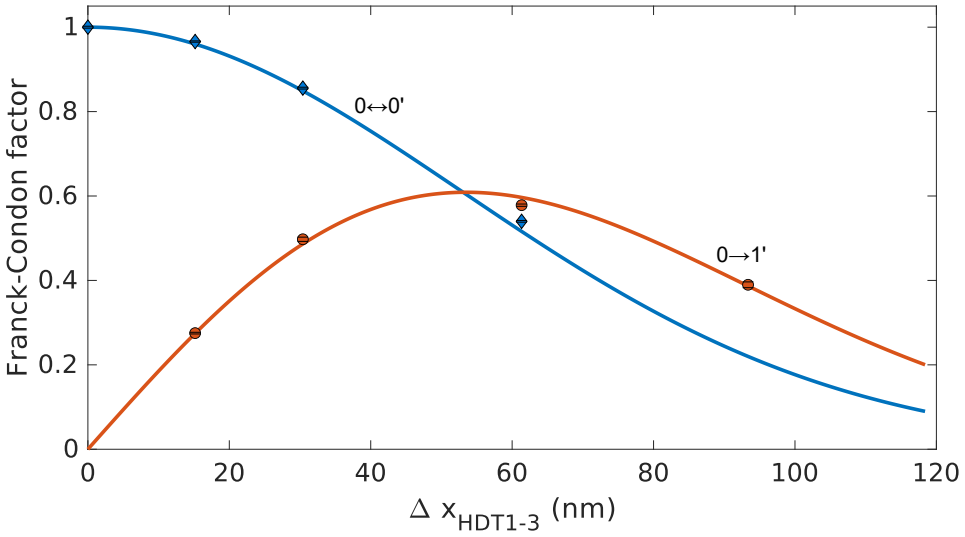

Figure 3.9: Measurement of the Franck-Condon factors for the carrier transition ($0 \rightarrow 0'$) and the 1st order sideband ($0 \rightarrow 1'$) along HDT1-3 for a displacement along HDT1-3. The data points are the ratios of the Rabi frequencies measured for different openings to the bare Rabi frequency. The solid lines are the theoretical calculations based on the lattice model.

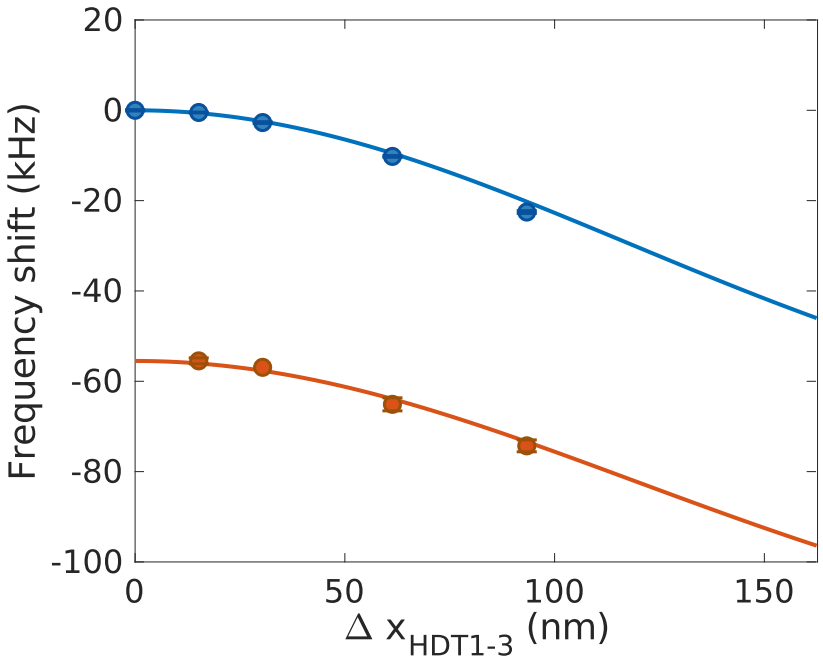

Figure 3.10: Measurement of the shift in frequency of the carrier (blue) and 1st order sideband (orange) for different lattice openings along HDT1-3. This red shift of the transition frequencies is expected since the potential $U_{|\downarrow\rangle}$ becomes shallower as it moves away from the maxima of the σ^+ lattice, resulting in a decrease in the energy difference between $|\uparrow\rangle$ and $|\downarrow\rangle$. The solid lines are theoretical expectations from known trap parameters.

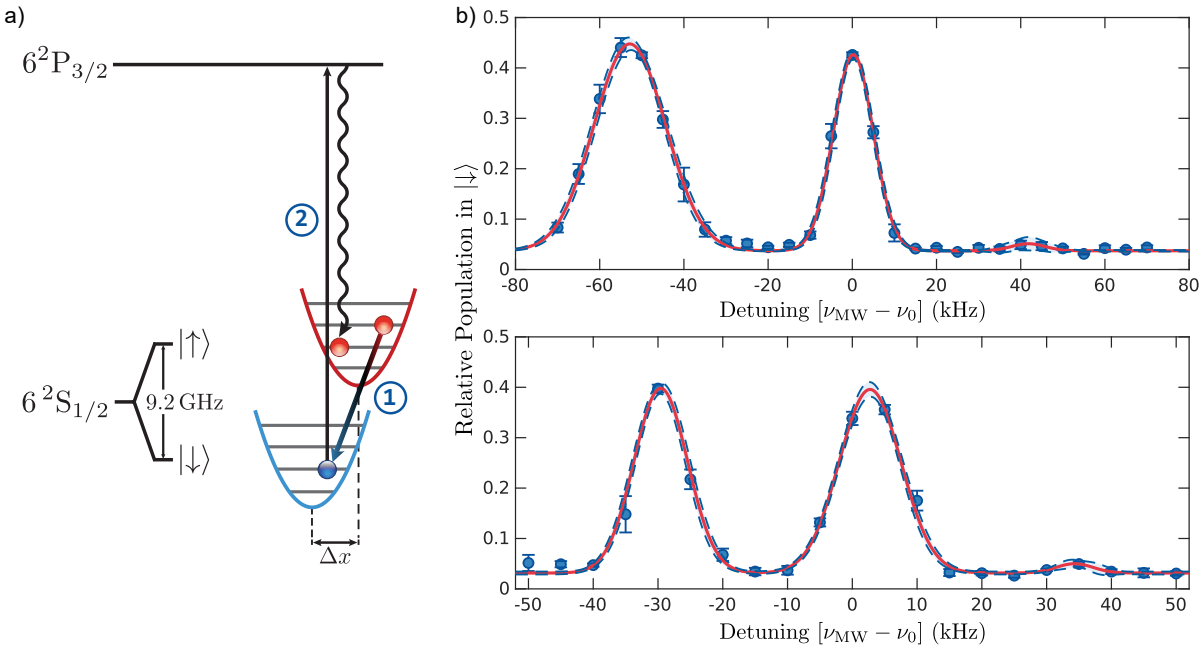

Figure 3.11: a) The microwave cooling scheme (Figure taken from [107]). The two potentials $U_{|\downarrow\rangle}$ and $U_{|\uparrow\rangle}$ are displaced with respect to each other to enable a microwave mediated transition from $|\uparrow, n\rangle \leftarrow |\downarrow, n-1\rangle$. A repumper is used to bring the atom back in state $|\uparrow\rangle$, maintaining the vibrational state, after which the cooling cycle repeats. b) A microwave sideband spectrum along HDT1-3 (top) and HDT2 (bottom). The spectrum is taken after microwave sideband cooling, which brings most atoms to the vibrational ground state. The occupation of the ground state can be computed from the ratio of the heating sideband to the cooling sideband (see text), and is about 95% in both cases.

then adiabatically shifted by a predetermined amount in the direction of HDT1-3 and the microwave is turned on to the transition $|\uparrow, n\rangle \rightarrow |\downarrow, n'\rangle$. Since this is the first cycle of cooling, to bring atoms quicker to the lower most vibrational states, the microwave is tuned to the resonance condition for $n \rightarrow n-2$. Hence the lattice is opened by an amount such that the Franck-Condon factor for the $n \rightarrow n-2$ transition is high. Once the atom has been transferred to the $|\downarrow, n'\rangle$ state, the cooling cycle is closed by a repumper photon, as shown in Fig. 3.11(a), which is resonant with the $|F = 3\rangle \rightarrow |F' = 4\rangle$ transition. The photon scattering event in the repumping process is the irreversible process in the cycle by means of which energy is removed from the system. For net cooling to occur, it is necessary that the vibrational state of the atom is preserved in the scattering process. This condition is fulfilled in the so called Lamb-Dicke regime, where the recoil energy of the scattered photon ($h\nu_{\text{recoil}}$) is much less than the spacing between the vibrational levels ($h\nu_{\text{trap}}$). The expression in terms of the Lamb-Dicke parameter, η, is [138]

$$\eta^2 = \frac{h\nu_{\text{recoil}}}{h\nu_{\text{trap}}} \ll 1 \tag{3.16}$$

We work in the Lamb-Dicke regime along both directions, HDT1-3 and HDT2, with $\eta^2_{\text{HDT1-3}} = 0.04$ and $\eta^2_{\text{HDT2}} = 0.07$.

After cooling along the direction HDT1-3 for around 10 ms, the lattice is opened along HDT2 (while closing along HDT1-3) and the same microwave cooling process is continued with the appropriate parameters for this direction. The cooling along HDT1-3 and HDT2 is alternated while decreasing the

cooling duration and also tuning the microwave to the $n = 1 \rightarrow n = 0$ transition. In the case where we cool along the third dimension, by means of sideband resolved Raman cooling, the microwave cooling sequences are interspersed with a Raman cooling sequences, for which the lattice is closed. It must be noted that in order to keep the atoms in the cooling cycle, they must be transferred to the outermost hyperfine level. To ensure that atoms that are scattered to other hyperfine levels are pumped back to $|\uparrow\rangle$, we also turn on the m_F pumping beam, which has been introduced in 2.4.

To finally measure the population in the vibrational ground state, we perform microwave spectroscopy on the cooled atoms as shown in Fig. 3.11(a). Before performing the spectroscopy, the lattice is opened along the direction we want to probe, in order to drive the sideband transitions. After a microwave π pulse is applied to bring the atoms from $|\uparrow\rangle$ to $|\downarrow\rangle$, atoms remaining in the state $|F = 4\rangle$ are pushed out by means of a resonant *push-out* beam. The microwave spectrum consists of three peaks: the central peak corresponds to the transition $|\uparrow, n\rangle \rightarrow |\downarrow, n\rangle$, the peak red-detuned to the carrier peak corresponds to the transition $|\uparrow, n\rangle \rightarrow |\downarrow, n+1\rangle$ (*heating sideband*) and the peak blue-detuned to the carrier corresponds to the $|\uparrow, n\rangle \rightarrow |\downarrow, n-1\rangle$ transition (*cooling sideband*). The two sideband spectra shown in Fig. 3.11(a) (along HDT1-3 (top) and HDT2 (bottom)) are taken after resolved sideband microwave cooling. As can be seen in the spectra, the *cooling sideband* is nearly non-existent. This is because once the atom populates the lowest vibrational state , $|\uparrow, n = 0\rangle$, there is no further cooling transition possible. Hence the atoms in $|\uparrow, n = 0\rangle$ remain in that state and are subsequently pushed out by the *push-out* beam. The spectrum lets us determine the final mean excitation number $\bar{n}$ by comparing the heights of the cooling and heating sidebands. With the assumption that the final motional states after cooling have a thermal distribution, $\bar{n}$ is given by [138, 139]

$$\bar{n} = \frac{h_{hsb}}{h_{csb} - h_{hsb}} \tag{3.17}$$

h_{hsb} being the height of the heating sideband and h_{csb} the height of the cooling sideband. This simple and robust method of determining $\bar{n}$ is independent of the duration of the microwave pulse, the rabi frequency of the carrier as well as the Lamb-Dicke parameter [138]. The ground state populations n_0 can be derived from $\bar{n}$, as is given by

$$n_0 = \frac{1}{1 + \bar{n}} \tag{3.18}$$

For our 2D lattice we are able to achieve a ground state population of $n_0^{\text{HDT1-3}} = 96.6 \pm 3.2\%$ along HDT1-3 and $n_0^{\text{HDT2}} = 94.9 \pm 2.1\%$ along HDT2. This corresponds to a 2D ground state population of $n_0^{2D} = n_0^{\text{HDT2}} \times n_0^{\text{HDT13}} \approx 92\%$. The ground state population can be further increased to >96% after addressing some of the heating mechanisms listed in [107, 119, 137], such as projection heating, discussed in the following section. Another limitation to achieving higher cooling efficiencies is the inhomogeneity of our trap, discussed in Chapter 4.

Heating rate measurements

To experimentally investigate the limitation to achieving close to 100% in the ground state, we measure the cooling and heating rates. The heating rates due to the intensity noise and phase noise of the lattice can be extracted from the noise measurements shown in section 3.2.1, and they are negligible. We further corroborate the calculated heating rates by performing a measurement with atoms. The atoms are sideband cooled close to the ground state and then after a given hold time a sideband spectrum is taken. The mean vibrational number is extracted from the spectrum and plotted as a function of hold time, as shown in Fig. 3.12. This measurement results in a heating rate of 0.39 ± 0.07 quanta/s along HDT13 and a heating rate of 0.18 ± 0.19 quanta/s along HDT2. The cooling rate measured along the two dimensions is 2.7×10^3 quanta/s. Following the explanation in [107], the mean vibrational occupation $\bar{n}$ can be given

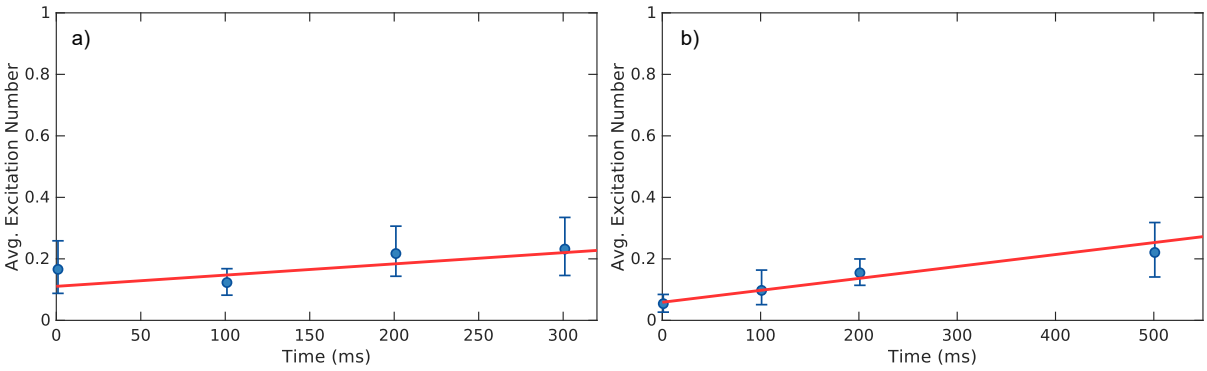

Figure 3.12: a) Background heating rate measurement along HDT2. All atoms are cooled close to the ground state along HDT2, following which they are held in the trap for a given duration before performing microwave sideband spectroscopy. Each data point corresponds to the average excitation number of the atoms extracted from a microwave sideband spectrum (see Eq. 3.17). We perform a linear fit to the data (solid red line) to extract a background heating rate of 0.18 ± 0.19 quanta/s. b) A similar measurement performed along HDT1-3, and the measured background heating rate is 0.39 ± 0.07 quanta/s.

by

$$\bar{n} = \frac{H_{\text{total}}}{C_{\text{total}} + H_{\text{total}}} \tag{3.19}$$

where H_{total} is the total heating rate and C_{total} is the total cooling rate. The heating caused by the phase and intensity noise is low enough to be able to achieve >99% population in the ground state. However, there is another important source of heating specific to our cooling scheme. When the potentials of $|\uparrow\rangle$ and $|\downarrow\rangle$ are displaced with respect to each other, there is an additional 'projection heating' [119]. The spatial difference between the potentials of the two internal states leads to a projection of the $|\downarrow, n\rangle$ state on any arbitrary state $|\uparrow, m\rangle$ compared to the case of identical potentials where the projection beyond $m = n, n \pm 1$ is negligible. The projection heating per microwave cooling cycle is

$$\Delta E_{\text{projection}} = \hbar\omega_{vib}\eta_x^2 \tag{3.20}$$

where $\eta_x = \Delta x/(2x_0)$ is the spatial Lambe-Dicke parameter. Δx is the displacement of the potential and x_0 is the rms width of the motional ground state. Ideally, when we open the lattice along one direction, the potentials should be overlapped along the orthogonal direction, however, we believe there might be some cross-talk in the phase locks while opening the lattice such that there is an opening along the orthogonal direction as well. This leads to uncompensated heating in the orthogonal direction while cooling along one direction. This heating rate was measured using a similar method as described above. The lattice was opened along HDT1-3 (HDT2) and sideband cooled for a certain cooling duration and then the lattice was opened along HDT2 (HDT1-3) to take a sideband spectra and calculate the mean vibrational occupation. While cooling along HDT13, the heating rate along HDT2 is 55 ± 6 quanta/s and while cooling along HDT2, the heating rate along HDT1-3 is 36 ± 5 quanta/s. These high cross-heating rates mean that with the current scheme of cooling, it will not be possible to simultaneously reach 99% in the ground state along both directions. From our cooling rate, we can assume that the least amount of duration we will require for the last cycle of cooling along either direction is ≈500 µs. If we cool along HDT2 as the last step of the cooling process, the best achievable population in the ground state along HDT1-3 will be limited to ≈98.2% , while cooling along HDT1-3 as the last step will leave us with

97.3% in the ground state along HDT2.

There are two alternate cooling schemes we plan to implement in order to overcome the limitation set by the projection heating. The first involves opening the lattice diagonal to the HDT2-HDT1-3 axis, such that we can address the sidebands along both directions simultaneously. In this scheme, we can either use a bichromatic microwave field where the two frequencies are set to the cooling transition along the two directions, or we can sweep the frequency of one microwave field to cover both cooling transitions. The latter was briefly tried in the lab but we did not reach a state of optimization where we could compare the advantage and efficacy of the scheme. The second cooling scheme involves pulsed sideband cooling [140]. In this scheme, the cooling and repumping sequences are performed sequentially. The lattice is opened along the direction of choice and a microwave pulse fulfilling the π condition on the cooling sideband is applied. Then the lattice is closed again and a repumping pulse is applied to complete the cooling cycle. The advantage of this scheme is that there is no projection heating since the repumping process only occurs when both potentials are overlapped. Furthermore, the frequency at which to set the microwave is independent of any possible light shifts from the repumping laser beam. To this end, we have installed an acousto-optical modulator to control the repumper beam such that it can be switched on/off within a microsecond, and the pulsed repumping scheme will be implemented soon.

3.5 Summary and outlook

In this chapter, I discussed the novel experimental scheme of state-dependent transport along two dimensions. I presented the first results from our lab of 2D state-dependent transport and the resultant application for cooling atoms to the ground state using microwave photons, achieving around 95% ground state population along two dimension. I further use the ability to transport to displace the two sub-lattices and measure the corresponding Frank-Condon factors, which determine the coupling strength of the different vibrational transitions.

In addition to opening up avenues for unique experiments, state-dependent transport also adds to our arsenal of techniques used in the experiment. For example, we can completely avoid the use of a 'pushout-beam' to heat out atoms in $|F = 4\rangle$, which is used in our state-detection. Instead, state-detection can be achieved by accelerating the σ^+ lattice until the atoms trapped in $|\uparrow\rangle$ are pushed out of the field of view. Based on [141], the 'catapult ramp' can be broken down into three sections, each of which are calculated based on given boundary conditions, such as the initial/final velocity, acceleration, and position. Fig. 3.13 shows an exemplary ramp. The first section of the ramp consists of moving the lattice from rest to a maximum acceleration, which corresponds to a maximum number of excitations we can permit the atom to have. The second part of the ramp consists of transporting the atoms with constant acceleration, during which the atoms acquire a high kinetic energy. The last section of the ramp entails decelerating the lattice and bringing it back to a 'closed lattice' condition. The idea here is that the atoms gain enough kinetic energy in the second part of the ramp so that they are not anymore trapped and continue to fly away as the lattice is being decelerated.

The entire catapult ramp can be completed in $\approx 10\,\mu s$. In comparison to our spin-relaxation time of $\approx 200\,ms$, the duration of the catapult is negligible, which means that we can be sure of only addressing atoms that were initially in $|\uparrow\rangle$. Once the catapult-ramp is complete, we have to wait for a few tens of milliseconds in order to let the atoms fly out of the region of interest. During this wait time, even if there are spin flips, the atoms that were initially in $|\downarrow\rangle$ will remain static while the rest fly out. The catapult technique has been tested in our setup with a 'state-detection' efficiency of ≈99.8%. There are many advantages the catapult technique has over the traditional state-detection where a laser beam resonantly heats out atoms in $|\uparrow\rangle$. The catapult method does not rely on any pushout laser beam, making the pushout

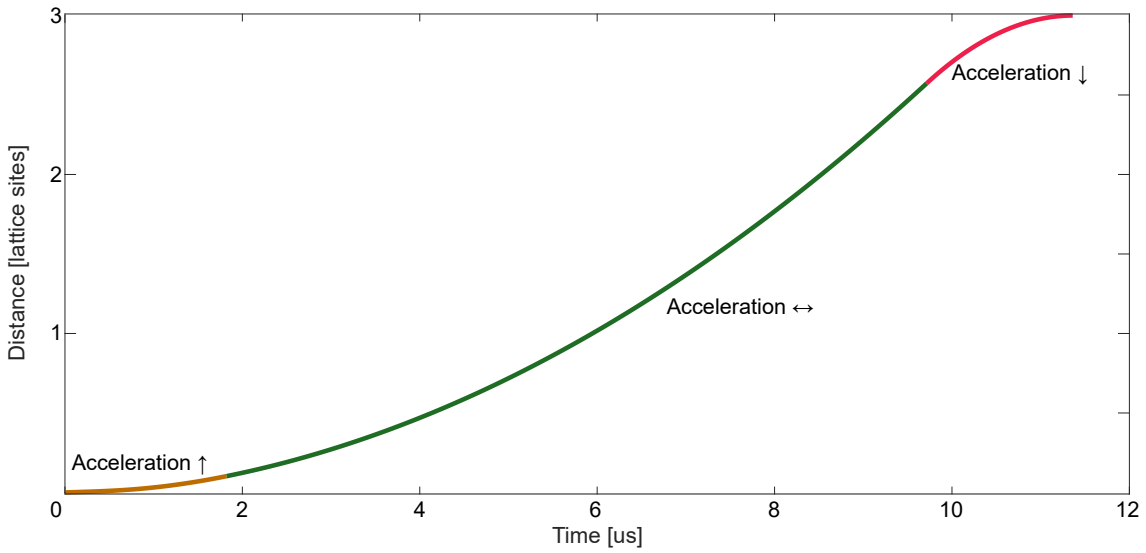

Figure 3.13: The trajectory of a 'catapult' ramp used to state-dependently expel atoms from the region of interest in a few µs. The ramp consists of three parts: with increasing (brown), constant (green) and decreasing (red) acceleration. The lattice itself is translated over three lattice sites, however the atoms gain enough kinetic energy to be released from the traps, and continue to fly out of the region of interest.

immune to any changes in laser power or frequency. Furthermore, the catapult ramp is much faster than the duration of a typical pushout pulse (500 µs), further lowering the probability of a push-out error due to spin relaxation. Lastly, the catapult allows us to either drag away atoms in state $|\uparrow\rangle$ or in state $|\downarrow\rangle$, while with the traditional pushout only atoms in $|\uparrow\rangle$ are resonantly heated out.

In addition to the catapult technique, state-dependent transport also allows us to reuse our atoms instead of expelling them out of the lattice. Here the process will involve transporting the atoms in either one of the states outside the region of interest (but still in the field of view) before taking an image. After the image, only atoms outside the region of interest can be addressed by means of a spatial light modulator, to prepare them in either $|\uparrow\rangle$ or $|\downarrow\rangle$, an then deterministically be brought back to either their original position or any other desired configuration inside the region of interest. Following this, a new experimental sequence can be begun without the need to load atoms from the MOT. Considering that $\approx 75\%$ of the run time of one experimental cycle is accounted for by the MOT loading, we will gain considerably when switching to reusing the atoms.

CHAPTER 4

Understanding qubit coherence using Ramsey spectroscopy

An ideal quantum system is perfectly isolated from the environment (information is not lost from the system) and remains coherent indefinitely. However, when the quantum system couples to the environment, there is a gradual loss of information from the system into the surroundings, termed decoherence [142]. Consequently, any system initially prepared in a quantum superposition eventually behaves as a classical statistical ensemble of the constituent states. Thus, to preserve the coherence of a system for long times, experimentalists have to devise tricks and methods to minimize the interaction with the environment.

Preserving coherence is a central goal of quantum physicists, and is particularly relevant for applications such as quantum metrology [143], quantum computing [12, 144, 145] and quantum simulation. To this end, much work has been done to study dephasing mechanisms in our research group [95, 130, 146]. Coherence plays a central role in the DQSIM experiment as well. From atom interferometry [120] to studying topologically protected states with quantum walks [68, 69], all measurements benefit from long coherence times. Our experiment was conceived keeping in mind the different physical origins of decoherence. For instance, to isolate our system from external magnetic field fluctuations, we have enclosed the vacuum cell in a two-layer mu-metal shielding (see sec. 2.4.1). Furthermore, we use an in-house designed ultra-low birefringence vacuum cell [82] to ensure that the differential light shift caused by the birefringence-induced ellipticity of our lattice beams is minimized. With these measures taken to isolate our system, we expect coherence times of the order of tens of milliseconds in our experiment. In this chapter, I will present the various techniques used to determine as well as counteract dephasing mechanisms in our experimental setup.

Inhomogenous and homogeneous dephasing

The spin dynamics of a two-level system under the influence of an environment or external field can be described by two phenomenological quantities, the spin relaxation time (with time constant T_1) and spin decoherence time (with time constant T_2). The T_1 time in our experiment is limited by photon scattering events due to the optical lattice lasers, and is of the order of 200 ms for our chosen experimental parameters. The transverse phase relaxation can be categorized into two types: homogeneous (with time constant T_2') and inhomogeneous (with time constant T_2^*) under certain limits [130] heuristically, and it is related to the two as

$$\frac{1}{T_2} = \frac{1}{T_2'} + \frac{1}{T_2^*} \tag{4.1}$$

Inhomogeneous dephasing is present only on account of the fact that we work with an ensemble of atoms. When resonance frequency conditions of the different atoms of the ensemble are detuned from each other, the quantum superposition of each atom evolves at a different rate, leading to a dephasing of the entire ensemble. These different resonance conditions are typically caused by the thermal distribution of the trapped atoms, such that fast and slow atoms undergo different amounts of light shift from the lattice beams, or from inhomogeneous light or magnetic fields across the ensemble of atoms. When such inhomogeneous dephasing is constant in time, it can be reversed with a spin echo, as shown in section 4.4.2.

On the other hand, homogeneous dephasing processes affect all atoms in the same way. Some of the common dephasing mechanisms are pointing instabilities of the trapping beam, intensity fluctuations, fluctuating homogeneous magnetic fields and heating of atoms in the trap. Unlike inhomogeneous dephasing, homogeneous dephasing is irreversible. In this chapter, I will present the various measurements conducted to understand the limitations of the coherence of our system, thereby showing that the maximum achievable coherence time in our system is 4.5 ms, using a spin echo pulse.

4.1 Ramsey interferometry

Initially devised to improve the spectral resolution of magnetic resonance by a factor of two, Norman Ramsey's interferometer [147] has played a ubiquitous role in atomic physics experiments, such as those concerning high-precision measurements, atomic clocks and experiments on atom entanglement [148]. Ramsey interferometry plays an important role in much of the work done in this thesis, from measuring coherences to imaging dipole traps (see chap 5).

In essence, the Ramsey spectroscopy sequence consists of the application of two coherent microwave pulses separated by a time interval t. The first microwave pulse, set to the $\pi/2$-condition, puts the atom in a coherent superposition of our two states, $|\uparrow\rangle$ and $|\downarrow\rangle$. After an evolution time t, a second $\pi/2$-pulses 'closes' the interferometer and the final state is projected onto either $|\uparrow\rangle$ or $|\downarrow\rangle$. Scanning the phase of the seconds $\pi/2$-pulse results in a Ramsey fringe, shown in Fig. 4.2. The contrast of this fringe is an indicator of the coherence, since any dephasing during the evolution time leads to to a reduction in the contrast of the interferometeric fringe.

The Ramsey technique can be visualized on the Bloch sphere, where north pole corresponds to state $|\uparrow\rangle = \begin{pmatrix}1\\0\end{pmatrix}$ and the south pole corresponds to the state $|\downarrow\rangle = \begin{pmatrix}0\\1\end{pmatrix}$, as shown in Fig. 4.1. We begin with preparing the Bloch vector in state $|\uparrow\rangle$. In matrix notation, the operations of the Ramsey scheme can be written as

$$\begin{aligned}
\hat{U}_{\pi/2} &= \frac{1}{\sqrt{2}}\begin{pmatrix}1 & i\\ i & 1\end{pmatrix} && \text{... initial } \pi/2\text{-pulse}\\
\hat{F}_{\Phi(t)} &= \begin{pmatrix}e^{i\Phi(t)/2} & 0\\ 0 & e^{-i\Phi(t)/2}\end{pmatrix} && \text{... free evolution for time t}\\
\hat{U}_{\pi/2,\phi_{\mathrm{rf}}} &= \frac{1}{\sqrt{2}}\begin{pmatrix}1 & ie^{i\phi_{\mathrm{rf}}}\\ ie^{-i\phi_{\mathrm{rf}}} & 1\end{pmatrix} && \text{... final } \pi/2 \text{ pulse with phase } \phi_{\mathrm{rf}}
\end{aligned} \tag{4.2}$$

The first $\pi/2$-pulse brings the block vector to the equatorial plane, where the vector precesses for time t, picking up a phase of $\Phi(t)$. The final $\pi/2$-pulse is applied with a variable phase ϕ_{rf}, which amounts to performing a $\pi/2$-rotation of the Bloch vector along a different axis determined by the choice of ϕ_{rf}. The Bloch vector is finally projected onto the state $|\downarrow\rangle$ by performing a measurement of the number of atoms

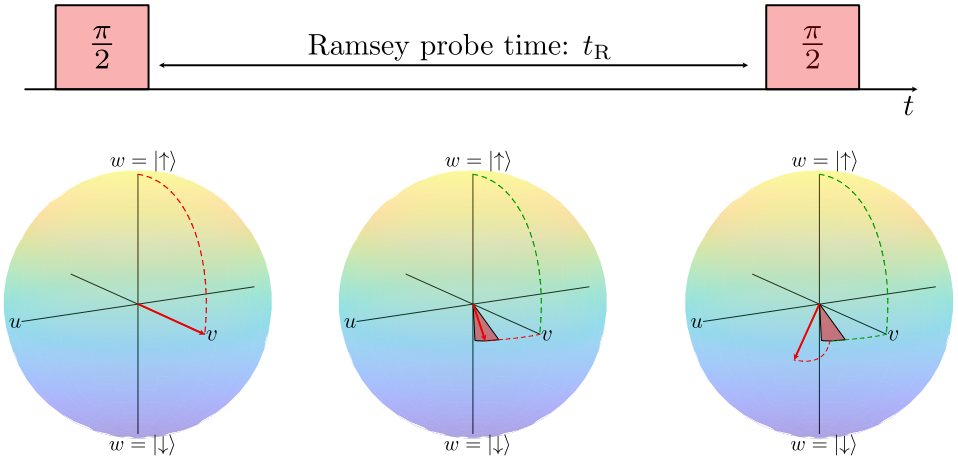

Figure 4.1: A Ramsey spectroscopy sequence represented on a Bloch sphere. The Bloch vector is initialized to the state $w = |\uparrow\rangle$. The first $\pi/2$ pulse rotates the vector to the equator, where it precesses on the equatorial plane with a phase $\Phi(t) = 2\pi(\nu_{mw} - \nu_{\Delta E})t$. The shaded region represents the the spread of Bloch vectors due to the fact that different atoms pickup different phases, leading to inhomogeneous dephasing. A final $\pi/2-$pulse is applied after time t_R along an axis determined by the phase of the microwave pulse, ϕ_{rf}.

populating state $|\downarrow\rangle$. Using the notation in Eq. 4.2, one can derive the expression for the Ramsey signal

$$\begin{aligned} P_{|\downarrow\rangle}(\phi_{\mathrm{rf}}, t) &= |\langle\downarrow| \hat{U}_{\pi/2,\phi_{\mathrm{rf}}} \hat{F}_{\Phi(t)} \hat{U}_{\pi/2} |\uparrow\rangle|^2 \\ &= \frac{1}{2}[1 + \cos(\phi_{\mathrm{rf}} + \Phi(t))] \end{aligned} \tag{4.3}$$

The phase acquired during the Bloch vector precession on the equator of the Bloch sphere can be written as $\Phi(t) = 2\pi(\nu_{\mathrm{mw}} - \nu_{\Delta E})t$ where ν_{mw} is the microwave frequency and $\nu_{\Delta E}$ is the frequency difference between the two states $|\downarrow\rangle$ and $|\uparrow\rangle$. Change in $\nu_{\Delta E}$ can be attributed to, e.g., light shifts or frequency shifts caused by magnetic fields. When taking an ensemble average of Eq. 4.3, we introduce the contrast term $C(t)$ and a survival probability term S to rewrite the Ramsey fringe model as [130]

$$P_{|\downarrow\rangle}(\phi_{\mathrm{rf}}, t) = \frac{S}{2}[1 + C(t)\cos(\phi_{\mathrm{rf}} + \Phi(t))] \tag{4.4}$$

It must be noted that the phase measured here is an ensemble average of the individual phases picked up by the atoms, and depends on the atom distribution (see chapter 5). The survival probability S is the probability of an atom remaining trapped in the lattice during the Ramsey sequence. This is typically close to 100% for our system, where the lifetime of atoms in the trap due to background gas collisions is on the order of tens of seconds as compared to the sub-millisecond timescale of the Ramsey sequence. Eq. 4.4 can be modified to account for a deviation of $\delta_{\pi/2}$ radians from an ideal $\pi/2$-pulse as well as $\delta_{\downarrow}$ error in the initial state preparation. The final expression for the Ramsey fringe is

$$P_{|\downarrow\rangle}(\phi_{\mathrm{rf}}, t) = S\left(\delta_{\downarrow} + \frac{1}{2}(1 - \delta_{\downarrow})\cos^2(\delta_{\pi/2})[1 + C(t)\cos(\phi_{\mathrm{rf}} + \Phi(t))]\right) \tag{4.5}$$

The expression for C(t) as an ensemble average of atoms with an energy distribution given by the three-dimensional Boltzmann distribution is derived in [130, 149]. Here an assumption is made that the evolution of the phase between the two $\pi/2$-pulses is characterized by the average differential light shift

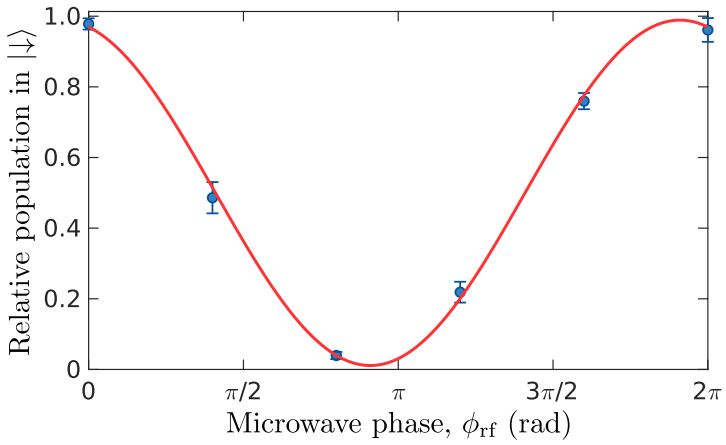

Figure 4.2: A typical Ramsey fringe, measured here for a Ramsey duration of 100 µs. The data is fit using the model described in Eq 4.5 (solid red line).

felt by the atoms. The Ramsey fringe contrast is then given by

$$C(t) = \left(1 + \frac{t^2}{\beta^2}\right)^{-3/2}, \quad \text{with} \quad \beta = \frac{2U_0}{k_B \mathrm{T} \delta_{ls,0}} \tag{4.6}$$

where U_0 is the trap depth, k_B the Boltzmann constant, T the temperature of atoms and $\delta_{ls,0}$ is the maximum differential light shift at the bottom of the trap. The T_2 time is defined to be the time taken for the contrast of the Ramsey fringe to fall to half the contrast at time zero, $C(T_2) = C(0)/2$. Hence, the contrast can be rewritten as

$$C(t) = \left(1 + \frac{t^2(2^{2/3} - 1)}{T_2^2}\right)^{-3/2} \tag{4.7}$$

In addition to this mechanism, there is also a loss of contrast by homogeneous dephasing mechanisms.

4.2 Measuring magnetic field drifts using Ramsey spectroscopy

One of the primary sources of dephasing in our experiments is magnetic field noise, which leads to a fluctuation in the frequency difference between the two states. Dominant sources of magnetic field noise are either in the electromagnets , used to generate the magnetic field for the quantization axis, or electronic devices in the vicinity of the experiment. The magnetic field noise of the electromagnets is caused by the current noise of the power supply, necessitating the need to stabilize them, for instance by using feedback loops [150]. To that end, we have implemented a current stabilizing feedback scheme [109]. To shield the atoms from magnetic noise from the environment, the vacuum chamber has been enclosed in a two-layer mu-metal shielding, as discussed in section 2.4.1, with a measured suppression of around 2000 for static fields.

Small magnetic field fluctuations in our laboratory are typically measured with a three-axis fluxgate magnetometer Mag-03[1]. However due to the mu-metal shielding enclosing our experiment, access to

[1] Bartington Instruments Ltd.

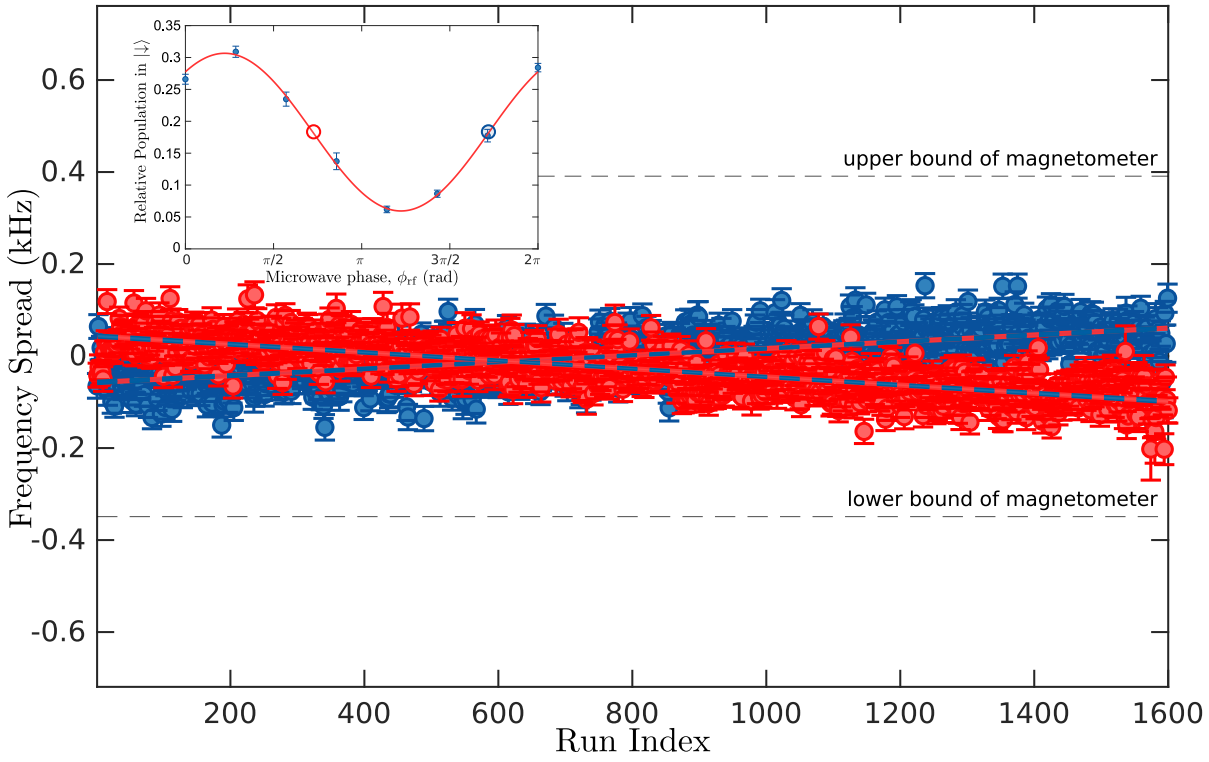

Figure 4.3: Measurement of the background magnetic field using the Ramsey magnetometer. Two points on the Ramsey fringe, at the point of maximum slope (see inset, circled red and blue), are continuously probed with the Ramsey spectroscopy sequence, by tuning to the corresponding microwave phase, ϕ_{rf}. The two points are π radians apart. The Ramsey spectroscopy is performed in 'free-fall', where all the light fields are turned off. In the presence of a changing magnetic field, the atoms acquire an additional phase $\Phi(t)$, shifting the Ramsey fringe by this amount. This shift in phase results in a proportional change in the population measured in $|\downarrow\rangle$ for the points we have chosen (the error bars are attributed to atom shot noise, see Appendix C). We convert any change in survival into a shift in frequency through the relation in Eq. 4.8. The upper and lower bounds of the magnetometer correspond to the values $\pm\pi$ for the accumulated Ramsey phase. The measurement is performed 1600 times, 800 times for each of the two microwave phases, corresponding to about 5 hours. We fit a line to the two measurement sets to extract the long term frequency drift, which is around 20 Hz/h. The phase spread $\Delta\phi$ gives us expected drop in contrast through Eq. 4.9.

the vicinity of the vacuum cell is difficult and hence we use the Ramsey scheme, to realize a Ramsey magnetometer, where the atoms are used as probes to measure the magnetic field fluctuations.

The measurement scheme consists of probing just a single point on the flank of the Ramsey fringe, at the point of steepest slope. Sitting on this point, any change in the relative population of atoms in $|\downarrow\rangle$ can be assumed to be linearly proportional to change in the phase of the Ramsey fringe. Hence, the scatter in relative population in $|\downarrow\rangle$ can be related to the fluctuation in the frequency difference between the states $|\uparrow\rangle$ and $|\downarrow\rangle$. The microwave frequency is set to the resonance frequency in free space for the given quantization field strength. Any phase acquired during the Ramsey spectroscopy sequence corresponds to a change in frequency of the resonance condition during the Ramsey probe time. The measurement is performed in 'free-fall', i.e. all light fields are turned off for the duration of the Ramsey probe time. This means that any frequency fluctuation during 'free-fall' can be attributed to the magnetic field. We repeatedly perform Ramsey spectroscopy for the point chosen on the Ramsey fringe for a few hours in

total and extract both the shot to shot fluctuation in the magnetic field as well as the long term drift in the magnetic field.

Prior to starting the measurement of the Ramsey magnetometer, we measure an entire Ramsey fringe to extract the background survival and contrast from the fringe for a given Ramsey probe time of 600 µs (inset in Fig. 4.3). Both the contrast and survival information are necessary to convert the population fluctuation into frequency shift, given by the expression:

$$\Delta\nu = \frac{\Delta P_{|\downarrow\rangle}}{SC\pi t} \tag{4.8}$$

where S is the background survival, C the contrast of the fringe for a Ramsey probe time of t, and $\Delta P_{|\downarrow\rangle}$ is the population measured in $|\downarrow\rangle$. From the fringe measurement, we also find out what the phase ϕ_{rf} of the second microwave $\pi/2-$pulse should be in order to be sitting on the point of steepest slope. For a phase $\Phi(t)$ acquired during a Ramsey sequence, the phase of the second $\pi/2-$pulse should be $\phi_{\text{rf}} = \Phi(t) + \frac{(2n+1)\pi}{2}$, where $n \in \mathbb{Z}$. We take measurements at two points of the fringe separated by π radians, as shown in figure 4.3, and we fit a line to the measured data to extract the long term drift in frequency, which is of the order of 100 Hz over five hours. The rms phase spread from the measurement is $\Delta\phi(t) = 0.21$ radians. The expected drop in contrast for such a phase spread corresponds to [95]

$$C(t) = e^{-\Delta\phi(t)^2/2} \tag{4.9}$$

which for our measured spread gives a contrast of 97.8% at 600 µs. This measurement shows that the contribution of magnetic field fluctuations to dephasing is negligible in our experiment, corroborating our expectations from the effort we have put in shielding our experiment from external magnetic fields as well as in stabilizing the current used to generate the quantization field.

4.3 Light shifts and dephasing

Light shifts are one of the fundamental aspects of field-matter interactions [79, 151, 152], used for cooling, trapping and manipulating atoms. However, there are cases where light shifts are detrimental and experimental efforts are geared towards avoiding them. For example, in optical lattice clocks, the lattice wavelength is chosen such that the light shifts felt by both clock levels are equal, thereby avoiding any change in the frequency spacing between the two levels [153, 154].

For our experiment too, differential light shifts are disadvantageous as they lead to dephasing between the states $|\uparrow\rangle$ and $|\downarrow\rangle$ [95]. Due to the fact that $|\uparrow\rangle$ is 9.2 GHz closer to the lattice laser frequency than the state $|\downarrow\rangle$, the two levels are shifted by different amounts leading to a change in the resonance condition [130]. Since the light shifts are proportional to the intensity of the laser beam, the resonance condition changes by an amount proportional to the light intensity. In the case of thermally distributed atoms, each atom experiences a different amount of lattice intensity based on their location in the potential well created by the optical lattice. Therefore, the ensemble of atoms, all picking up a different phase in the Ramsey spectroscopy sequence, undergo inhomogeneous dephasing, leading to short T_2^* times. The differential light shift induced dephasing can be reduced by cooling atoms to the 3D ground state, where we can assume all atoms undergo the same amount of differential light shift by virtue of being at the bottom of the potential and seeing the same intensity of laser light. Along with the scalar contribution to the light shift, imperfections of the polarization of the light field also cause a differential light shift, leading to additional dephasing [155, 156].

The total differential light shift (both scalar and vectorial components), δ, between our two states $|\uparrow\rangle$

and $|\downarrow\rangle$ is given by the expression:

$$\delta(\vec{r}, \epsilon) = (\eta_s + \epsilon\eta_v)U(\vec{r})/h, \tag{4.10}$$

where $U(\vec{r})$ represents the trapping potential at position $\vec{r}$, η_s is a constant factor accounting for the scalar contribution to the light shift [130] and η_v accounts for the vectorial contribution to the differential light shift [157] which comes into play when the lattice beam has a non-zero polarization ellipticity ϵ, defined as

$$\epsilon = \frac{I_R - I_L}{I_R + I_L}, \tag{4.11}$$

where I_L and I_R correspond to the intensities of the left and right circular polarization components of the laser beam, respectively. The scalar component of the light field is given by the expression [130]:

$$\eta_s = \Delta_{\mathrm{HF}}\left(\frac{3}{2\Delta_{\mathrm{D1}} + \Delta_{\mathrm{D2}}} - \frac{1}{\Delta_{\mathrm{D1}}} - \frac{1}{\Delta_{\mathrm{D2}}}\right) \tag{4.12}$$

where Δ_{HF} is the hyperfine splitting between the two states $|\uparrow\rangle$ and $|\uparrow\rangle$, and Δ_{D1} and Δ_{D2} are the lattice detunings from the D1 and D2 line respectively. The vectorial component is given by the expression [155]

$$\eta_v = (m'_{\mathrm{F}} g'_{\mathrm{F}} - m_{\mathrm{F}} g_{\mathrm{F}})\frac{\Delta_{\mathrm{D1}} - \Delta_{\mathrm{D2}}}{2\Delta_{\mathrm{D1}} + \Delta_{\mathrm{D2}}} \tag{4.13}$$

where m'_{F} (m'_{F}) and g'_{F} (g_{F}) are the magnetic quantum number and the g-factor associated with the state $|\uparrow\rangle$ ($|\downarrow\rangle$). For the electronic ground state of alkali atoms, $g'_{\mathrm{F}} = -g_{\mathrm{F}}$. In our experiment $g'_{\mathrm{F}} = 1/4$ and this results in a $\eta_s = 2.5 \times 10^{-3}$ and $\eta_v = 7/4$ for our lattice wavelength of 866 nm. Following [130], the T_2^* time for an ensemble of atoms with temperature T is given by

$$T_2^* = \frac{2\hbar}{\eta_s k_B T} \tag{4.14}$$

where k_B is the Boltzmann constant and $\hbar$ the reduced Plank constant. For a temperature of $T \sim 1\,\mu$K, we get an upper limit on the coherence time T_2 of ~ 6 ms, which is achieved for purely linearly polarized light, in the absence of vectorial light shifts, as can be seen in Eq. 4.10. However, in practice, it's not surprising to expect a non-zero ellipticity. The vectorial contribution of the light shift is stronger than that of the scalar contribution. An ellipticity in our lattice laser beams can either be a result of an imbalance of intensities in our polarization synthesizer or it could be induced by the stress-induced birefringence of the vacuum glass cell. In the next section we measure the stress-induced birefringence of the vacuum window, using atoms as probes.

4.3.1 In situ measurement of vacuum window birefringence

The stress-induced birefringence was previously measured by optical means using a linearly polarized probe laser passing through a window, and the new polarization state being projected onto a polarizer [82]. However, the measurement was performed in a test vacuum setup, which experienced different (and potentially smaller) mechanical stress compared to the DQSIM apparatus developed in this thesis, and the sensitivity of the measurement relied upon the achievable extinction ratio of the polarizer and the sensitivity of the photodiode used. In this section, I will present the in-situ measurement of the stress-induced birefringence Δn of a vacuum window and the orientation angle θ_0 of its optical axis, using Ramsey spectroscopy. This measurement is similar to previous work done in our group [155], however

with a higher precision owing to the use of Ramsey spectroscopy rather than microwave spectroscopy.

Ramsey spectroscopy plays a central role in this thesis as a technique used for high precision spectroscopy. We use the most sensitive probes at hand, the atoms, to measure the change in polarization induced by the vacuum window on a probe laser. While varying the angle θ of the incident linear polarization, we measure the light shift δ of a hyperfine transition by means of Ramsey spectroscopy, which behaves as

$$\delta \propto S_0 \epsilon \tag{4.15}$$

where the proportionality constant is determined by the atomic properties, ϵ is the ellipticity of the beam and S_0 denotes the Stokes parameter, which specifies the total intensity of light. In the Jones matrix formalism, the ellipticity can be rewritten as [155]

$$\epsilon = \sin(kL\Delta n)\sin(2(\theta - \theta_0)) \tag{4.16}$$

where k is the laser wave-vector, L is the thickness of the vacuum window . For alkali atoms, the two hyperfine states of the ground state can are denoted by

$$|a\rangle = |F = I + 1/2, m_F\rangle$$
$$|b\rangle = |F = I + 1/2, m'_F\rangle$$

with the quantization axis aligned along the direction of the probe beam. For a given ellipticity ϵ of the probe beam, the resonance frequency is shifted by [155]

$$\delta = \alpha \frac{\nu_2 - \nu_1}{(\nu_L - \nu_1)(\nu_L - \nu_2)} (g'_F m'_F - g_F m_F) S_0 \epsilon \tag{4.17}$$

where ν_L is the probe laser frequency, ν_1 and ν_2 are the resonance frequencies of the D1 and D2 lines of cesium, g_F and g'_F are the g-factors of the states $|a\rangle$ and $|b\rangle$, and $\alpha = c^2\Gamma_1/(32\pi^3 h\nu_1^3) \approx c^2\Gamma_2/(32\pi^3 h\nu_2^3)$ is the proportionality constant depending on the natural decay rates Γ_1 and Γ_2 of the doublet states, the speed of light c and Planck constant h.

From equation 4.17 it is clear that the light shift can only be measured for the case $g'_F m'_F \neq g_F m_F$, and that for a given intensity S_0 and ellipticity ϵ the sensitivity of the measurement $\beta = \delta/(S_0\epsilon)$ is higher for larger line doublet splittings ν_2-ν_1, making heavier atoms more sensitive. Furthermore, the sensitivity also depends on the laser frequency, with the measurement being more sensitive for laser frequencies close to resonance. The probe laser we use in the measurement is one of the polarization synthesized lattice beams which is tuned to the frequency of 866 nm. States $|a\rangle$ and $|b\rangle$ correspond to $|F = 3, m_F = 3\rangle$ and $|F = 4, m_F = 4\rangle$, respectively. For the chosen wavelength and hyperfine states, the sensitivity β corresponds to 50 kHz/(W/mm^2). The angle θ of the incident linear polarization of the lattice beam can be precisely tuned to any value, details of which are discussed in chapter 3.

The measurement scheme consists of loading atoms in our 3D optical lattice followed by turning on the quantization axis (≈3G), aligned parallel to the probe beam. The atoms are then optically pumped to the state $|F = 4, m_F = 4\rangle$, following which all beams except the probe laser beam are turned off. We then perform Ramsey spectroscopy on the atoms to measure the resonance condition between the two hyperfine states. The difference in the resonance frequency with and without ('free fall') the probe beam is the light shift. This light shift is measured as a function of θ, the angle of the incident linear polarization. The data, displayed in Figure 4.4a, shows the expected sinusoidal behavior, which is fit with a function

$$\delta = \delta_0 \sin(2(\theta - \theta_0)) \tag{4.18}$$

Window No.	Δn	Error Δn	θ_0 (°)	Error θ_0 (°)
1	6.11×10^{-8}	7.15×10^{-10}	6.15	0.01
2	1.22×10^{-7}	9.93×10^{-10}	9.27	0.01

Table 4.1: The birefringence and orientation of the optical axes for two windows of the vacuum cell, measured using trapping beams HDT1 and HDT3.

with the amplitude $\delta_0 = \beta S_0 \sin(kL\Delta n)$, where the thickness of the window, L, is known to be (5.0 ± 0.1) mm. From the fit we extract the birefringence Δn and the angle θ_0 of one of the optical axes. The measured values of Δn and θ_0 for the two windows we investigated are given in table 4.1.

From the sinusoidal fit, it is also possible to determine the scalar light shift δ_s, which is proportional to the trap depth U_0 and is independent of the angle of polarization

$$\delta_s = \eta_s U_0$$

where η_s is the proportionality factor. For a laser of frequency ν_L,

$$\eta_s = \left(-\frac{1}{\nu_L - \nu_1} - \frac{1}{\nu_L - \nu_2} + \frac{3}{2(\nu_L - \nu_1) + \nu_L - \nu_2} \right) \times \nu_{HF} \tag{4.19}$$

where ν_1 and ν_2 are the frequencies of the D1 and D2 lines of cesium, respectively, and ν_{HF} is the hyperfine transition frequency of cesium. For our probe laser at 866 nm, η_s correspond to 2.5×10^{-3}. Hence the offset of the sinusoidal fit from the 'free-fall' condition, when the frequency shift vanishes, can be attributed to the scalar contribution of the light shift. This statement holds true for the ideal case where we are incident with a perfectly linear polarization. However, in the case where the incident beam has a non-zero ellipticity, there will be an offset due to the vectorial light shift caused by the intrinsic ellipticity of the incident beam. The degree of linearity of the incident beam is measured using a polarizer[2], where we achieve an extinction[3], ξ_{ext}, of around 10^{-5}. However this measurement is limited by the spatial inhomogeneities across the surface of the photodiode chip[4] as well as the spatial inhomogeneity of the beam itself [121]. The degree of polarization of the probe beam is best visualized on a Poincaré sphere, where a linearly polarized beam corresponds to a Stokes vector along the equator. In our experiment, the linearly polarized probe beam is composed of two independent phase and intensity locked circularly polarized beams (see chapter 3 for further details). Any fluctuation in the phase of the two circular polarizations results in the Stokes vector moving along the equator, which does not change the ellipticity of the beam. On the other hand, any fluctuation in the intensity of either of the two circular polarizations moves the Stokes vector along the north-south direction, thereby changing the ellipticity of the beam. The extinction ratio due to the intensity noise can be related to the ellipticity by[158]

$$\epsilon^2 = 4\xi_{\text{ext}}$$

From the ellipticity induced by the intensity noise, we can estimate the light shift offset, δ_{off}, for our

[2] GL10-B, Thorlabs, Inc.
[3] ξ_{ext}=(I_{min}/I_{max}), where $I_{min}(I_{max})$ is the minimum(maximum) intensity transmitted through the polarizer.
[4] PDA-10A, Thorlabs, Inc.

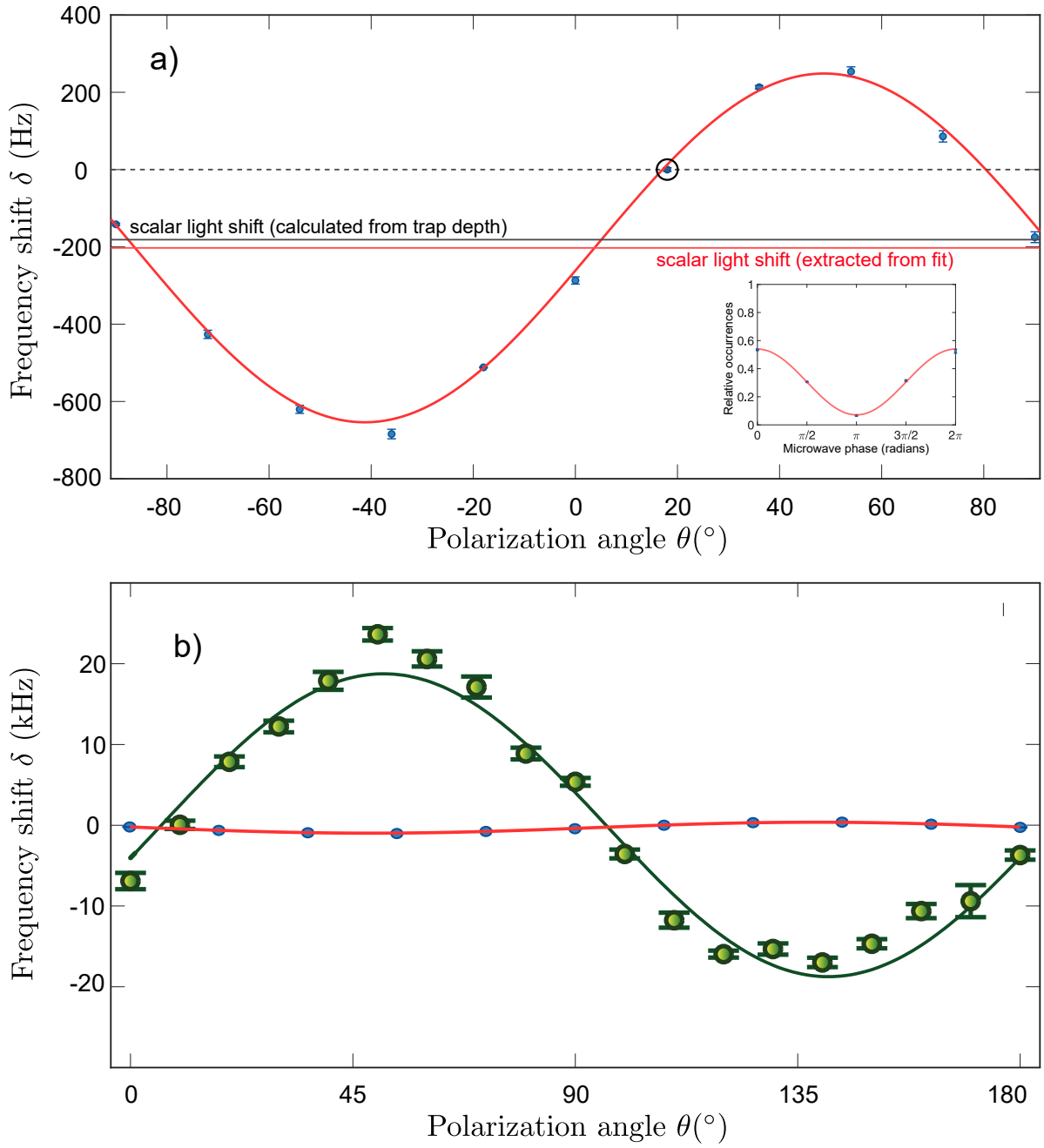

Figure 4.4: a) Light shift measured as a funciton of incident polarization angle θ for window 1. The data is fit with the sinusoidal function given in equation 4.18. The inset shows a typical Ramsey fringe, in this case for the circled data point. The scalar light shift is calculated from the known trap depth and plotted against the scalar light shift extracted from the fringe, which corresponds to the center of the fit. The discrepancy can be explained due to the non-zero intensity noise of the laser beam, explained further in the text.(b) shows a similar measurement performed using microwave spectroscopy (green) that is recorded with a commercial fused-silica ultra-high vacuum cell (, adapted from [155],), overlaid with the measurement shown in (a). The large reduction in birefringence for our vacuum cell window is evident from the reduction by a factor of around twenty in the amplitude of the sine curve. Both curves are obtained using a similar intensity of the probe beam. The error on the measured birefringence using Ramsey spectroscopy is smaller by a factor of eight compared to the measurement using microwave spectroscopy.

measurement as

$$\begin{aligned}\delta_{\text{off}} &= \frac{U_0}{h} \times \frac{\Delta I}{I} \\ &= \frac{U_0}{h} \times 2\epsilon \\ &= 4 \times \frac{U_0}{h} \times \sqrt{\xi_{\text{ext}}}\end{aligned} \tag{4.20}$$

where U_0 is the trap depth, h is the Planck constant, and $\Delta I/I$ characterizes the width of the distribution of $I_R - I_L$, where I_R and I_L are the two circular components creating our linearly polarized probe beam. Taking into account the values of the measured trap depth ($\approx$ 80 kHz) and the intensity noise limited extinction ($\approx 10^{-8}$) into equation 4.20, we get an offset in the light shift of around 30 Hz, which is in very good agreement with the experimental data.

4.3.2 Canceling light shifts

In the previous section (sec. 4.3.1), we have seen that our vacuum window birefringence is very low. However, we also can see in Fig. 4.4 that at an angle of incidence of 0° there is a residual light shift of around 300 Hz. Taking inspiration from precision metrology experiments where the differential light shifts are completely eliminated by choice of atomic states [114] or lattice laser properties [159, 160], we try to eliminate the light shifts using the polarization synthesizer. We induce an ellipticity in the laser beam such that the vectorial contribution to the light shift cancels out the scalar contribution to the light shift, similar to the work done in [160].

We make use of Ramsey spectroscopy, to precisely track the frequency difference between the two states. Since we intend to cancel out the light shifts such that the corresponding resonance frequency is the same as in free fall, we set the microwave frequency accordingly. The phase picked up during the Ramsey spectroscopy lets us compute the magnitude of the light shift. However, one has to be aware of the possibility of phase wrapping, which would occur if the light shift δ_{ls} fulfills the condition

$$|\delta_{\text{ls}}| > \frac{1}{t_R} \tag{4.21}$$

where t_R is the Ramsey interrogation time. There are two ways to avoid the phase wrapping, either t_R can be reduced (at the cost of losing precision) or a microwave spectrum can be taken in order to determine how large the light shift is. Once we know the scale of the light shift from the microwave spectrum, we can add this value to shift closer to resonance the microwave frequency used for Ramsey spectroscopy. This lets us determine the light shift with higher resolution while also avoiding any phase wrapping.

The measurement begins by precisely determining the resonance condition between the states $|\uparrow\rangle$ and $|\downarrow\rangle$ when the atoms are in free fall. The microwave is set to the expected resonance frequency for a quantization field strength of $\approx$ 3G, and Ramsey spectroscopy is performed in free fall while varying the Ramsey probe duration. The scheme of the spectroscopy in free fall follows the same procedure as one with the lattice, with the exception that all lattice beams are turned off before the first $\pi/2$-pulse of the Ramsey sequence is applied and they are turned back on after the last $\pi/2$-pulse of the Ramsey sequence is finished.

If the frequency of the microwave is exactly on resonance with the hyperfine splitting, we expect that the phase acquired for the different Ramsey probe times will be zero. However, if the microwave is detuned with respect to the resonance condition by δ_ν, we can expect that the phase picked up for a Ramsey probe time t_R is $\phi = 2\pi\delta_\nu t_R$. This function is fit to the data of phase versus Ramsey probe time as shown in Fig. 4.5(a). From the fit we infer that the frequency of the microwave is (881 ± 16) Hz red

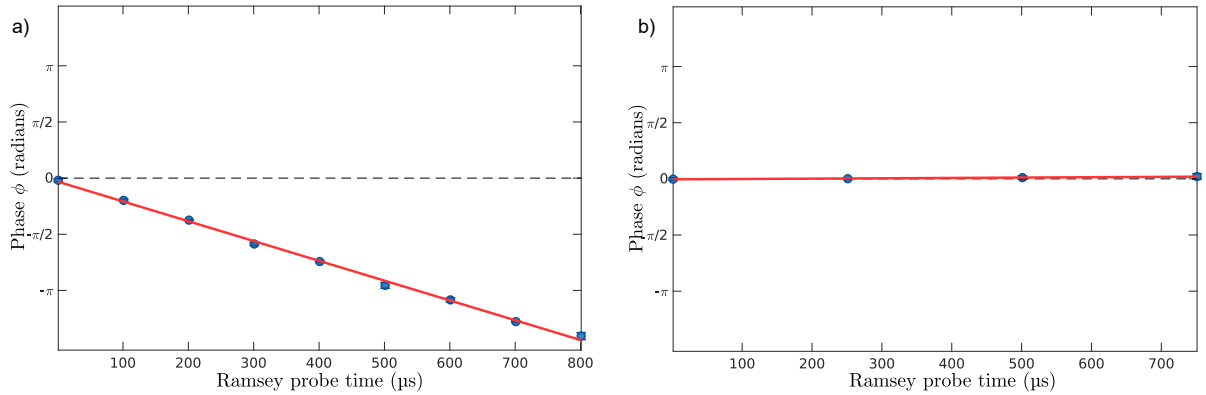

Figure 4.5: a) The phase acquired by atoms in a Ramsey spectroscopy sequence during free-fall as a function of the Ramsey probe time. The phase acquired ϕ is related to the detuning between the microwave rf frequency and the resonance frequency between the two states $|F = 4, m_F = 4\rangle$ and $|F = 3, m_F = 3\rangle$ through the expression $\phi = 2\pi\nu t$, where ν is the detuning and t the Ramsey probe time. The detuning of ~882 Hz extracted from a linear regression (solid red line) is used to correct the microwave rf frequency and set it to the resonance condition. b) The Ramsey measurement in free-fall is repeated with the adjusted microwave frequency,showing a reduction in detuning to ~16 Hz. This technique allows us to precisely determine the zeeman shift for our applied quantization field strength of 3G.

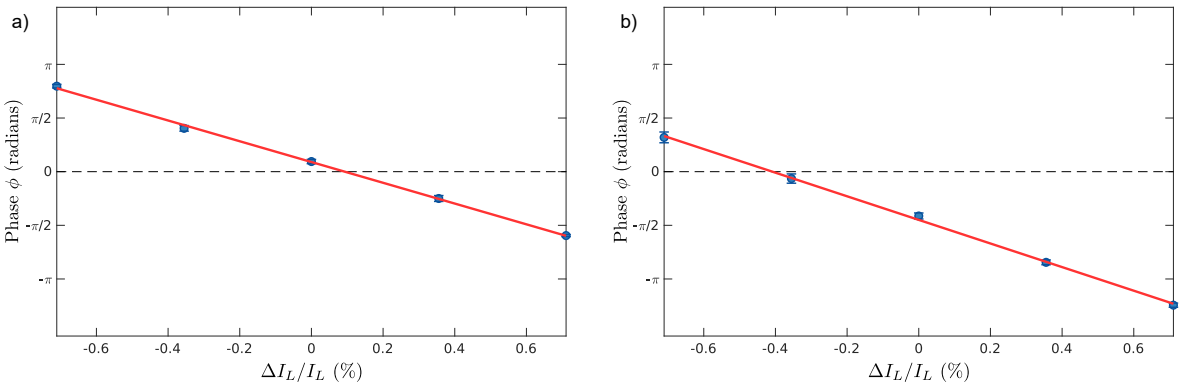

Figure 4.6: Phase acquired in a Ramsey spectroscopy sequence while varying the intensity I_L of the σ^+ component of the lattice beam a) HDT1 and b) HDT3. The intensity is changed in order to tune the light shifts such that the vectorial component cancels out the scalar component. The intensity at which the light shifts are canceled corresponds to zero phase acquired during Ramsey spectroscopy, shown by the dotted line. The Ramsey probe time for these measurements is set to 800 µs.

detuned from the resonance condition. Repeating this procedure with an adjusted microwave frequency yields a remaining detuning of (15.9 ± 1.9) Hz, as shown in Fig. 4.5(b). This procedure highlights how useful Ramsey spectroscopy is as a tool for precise measurements of frequency. It must be noted that this ≈16 Hz offset in frequency is over ≈9.2 GHz, showing the level of accuracy achievable with this technique.

The light shifts for each of the two polarization synthesized beams was canceled independently. The measurement scheme consists of loading and cooling the atoms in the 3D optical lattice and then turning off all laser beams except the lattice arm for which we want to tune the ellipticity. The microwave

frequency is set to the resonance condition as described above. For the lattice beam under investigation, we perform Ramsey spectroscopy and plot the Ramsey phase acquired as a function of the intensity I_L of the left-circularly polarized component. The Ramsey probe time is fixed, hence the phase acquired in the Ramsey sequence is proportional to the intensity I_L. From this measurement,we extract the optimal intensity for the left-circularly polarized beam, which is the intensity at which the phase acquired is zero. This point corresponds to the case where the frequency between the states $|\uparrow\rangle$ and $|\downarrow\rangle$ corresponds exactly to the resonance condition in free fall. The measurement to find the optimal intensity for HDT1 and HDT3 are shown in Fig. 4.6(a) and (b), respectively, using a Ramsey probe time of 800 µs. From the measurement we find that I_L for HDT1 has to be increased by 0.1% while I_L for HDT3 has to be reduced by 0.4%, in order to compensate the residual ellipticity of these laser beams.

4.4 Spatial analysis of coherence times

As we have discussed, inhomogeneous dephasing occurs when atoms acquire different phases due to the different frequencies between the two states $|\uparrow\rangle$ and $|\downarrow\rangle$. In our experiments, the atoms are trapped over a horizontal extent of 100 µm × 100 µm and in order to maintain a high coherence, atoms at every position should have the same resonance frequency. In this section we investigate the position dependent phase acquired by atoms due to inhomogeneities in the magnetic field generated for the quantization axis or the inhomogeneities in the light field at different positions of the lattice.

4.4.1 Measuring magnetic field inhomogeneities

The magnetic field for the quantization axis is generated by a pair of magnetic coils in a configuration similar to a Helmholtz configuration, enclosed within the mu-metal shielding. In section 4.2, we have shown the stability of the magnetic field, finding that there are negligible fluctuations in the field generated by the coils and also vanishing fluctuations due to external noise sources (see section 2.4.1). However, a gradient in the magnetic field, however stable, will lead to a position dependent frequency shift between the two states.

To measure the magnetic field gradient, we perform Ramsey spectroscopy on atoms in free fall and analyze the data in small sections of the image in order to extract the local frequency shift due to the magnetic field gradient. The images of size 490×490 pixels are broken down into smaller sections of size 10×10 pixels (~6×6 lattice sites). In order to cover a large region of interest, we initially position atoms at different regions in the lattice for the Ramsey measurement by means of state-dependent transport from the densely populated trap center. This is possible since the initial loading is consistently in the center of the image, where the vertical dipole trap helps confine the most number of atoms.

After the atoms are cooled and trapped in the MOT, they are loaded into the optical lattice. At the same time, the intensities of both the horizontal lattice and the vertical lattice are ramped up simultaneously. Following this, we compress the atomic ensemble by alternately turning off the horizontal and vertical beams such that the atoms can roll to the center of the vertical and horizontal traps, respectively. This way, we can confine the atoms to a small region centered around the VDT. After this compression, the atoms are state-dependently transported to the position we want to probe. Following this, an image is taken to record the position and the number of atoms. The lattice beam intensities are then lowered to the 'science-lattice' condition, where we have optimized the parameters for 3D ground state cooling. This corresponds to a trap depth of around 540 kHz for the horizontal lattice and a trap depth of around 200 kHz for the vertical lattice. After ground state cooling, all lattice beams are adiabatically turned off and the Ramsey sequence is executed with the two $\pi/2$-pulses interspaced with the Ramsey probe time

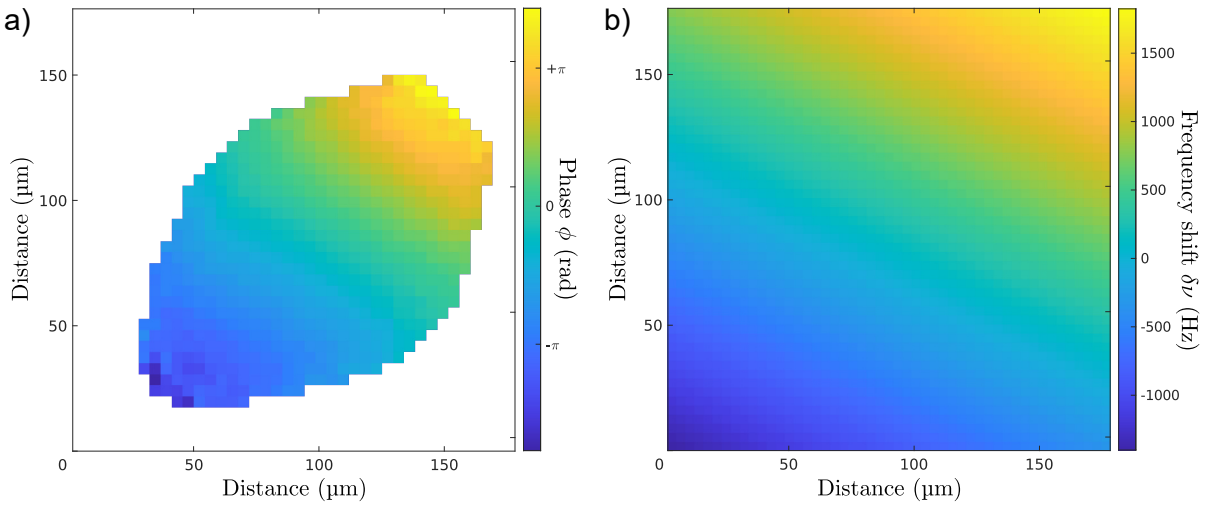

Figure 4.7: a) A phase map, corresponding to frequency shifts due to magnetic field gradients, extracted from the Ramsey spectroscopy of atoms in free-fall. The Ramsey fringes are analyzed section wise with each section of size 3.6 µm×3.6 µm. With the known Ramsey probe duration of 600 µs, the phases values are converted into a corresponding frequency shift $\delta\nu$ between the states $|\uparrow\rangle$ and $|\downarrow\rangle$. The white space corresponds to the region with no data due to too few number of atoms in that region. b) A 2D plane is fit to the frequency data extracted from (a) in order to extrapolate to the regions where no atoms were loaded.

of 600 µs. Consecutively, the lattice beams are turned back on the the 'science lattice' condition and a push-out beam is turned on to heat out all atoms in $|F = 4\rangle$. The remaining atoms are then imaged after increasing the trap depth of both the horizontal and veritcal lattice. The resulting Ramsey fringes are analyzed section-wise, with a section size of 3.6 µm×3.6 µm. The resulting phases for each of the Ramsey fringes is plotted in Fig. 4.7, where a clear gradient is visible. The 2D phase plot is converted to frequency and fitted with a plane, shown in Fig. 4.7(b). From the measurement we can calculate the magnetic field gradient along the direction of the quantization axis, since the frequency shift $\delta\nu$ is related to the magnetic field B through the linear Zeeman shift

$$\delta\nu = 2\pi \times \frac{\mu_0 \mathrm{B}}{h}(m_F g_F - m_{F'} g_{F'}) \tag{4.22}$$

where the μ_0 is the Bohr magneton, g_F and $g_{F'}$ the Landé factors and h the Plank constant. For the outermost hyperfine levels that we work with, $m_F = 3$ and $m_{F'} = 4$. The measured magnetic field gradient is $\approx$38mG cm^{-1}, which agrees well with the simulation performed in [78]. From the measurement, it is clear that the inhomogeneity of the magnetic field leads to inhomogenous dephasing. Since for most future experiments the region of interest will be confined to 10×10 lattice sites, which corresponds to about 6 µm×6 µm, this inhomogeneity will not be very detrimental. However, one can reverse the inhomogeneous dephasing by means of a spin echo, which will be explained in the next section. To get an estimate of the relevant coherence times, we hereafter analyze all coherence times section-wise. In Fig. 4.8 we can see the difference in the contrast extracted for a small region of 20×20 lattice sites versus the entire region of around 200×200 lattice sites where atoms are trapped for a measurement of coherence in free fall. As expected, the trend in the contrast for free-fall indicates a long coherence time. However, we cannot probe the Ramsey fringe in free fall for longer times since the atoms are free to fly out of the region of interest, or fly from one region another, thereby smearing the phase and reducing

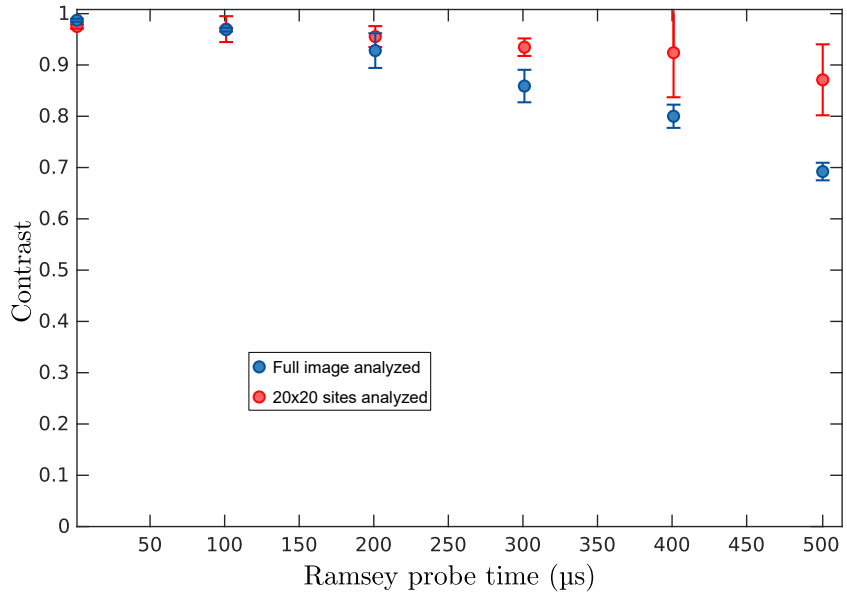

Figure 4.8: Measurement of Ramsey fringe contrast for free fall atoms as a function of the Ramsey time. Comparison of the contrast measured for Ramsey fringes analyzed over the entire image (blue) versus fringes analyzed for a small region of interest (red). The smaller region of interest corresponds to 3.6 µm×3.6 µm. By choosing a smaller region of interest, we ensure the inhomogeneous dephasing induced by the magnetic field gradient is small within the region of interest, exemplified by the higher contrast measured for the Ramsey fringes.

the contrast. To get a lower limit on the coherence time in free fall, we measure the T_2 time for atoms trapped in the vertical lattice, discussed later.

4.4.2 Measuring inhomogeneities of the optical lattice

In section 4.3.2, we discuss how atoms observe different amounts of light shifts leading to dephasing, due to different intensities of light seen by the atoms. The technique we used to cancel out the light shifts was performed taking into consideration the entire ensemble of atoms spanning an extent of ≈100×100 lattice sites. Therefore, we successfully canceled out an average light shift. However, there is a gradient of ellipticities across our dipole trap beams, which means that the we cannot cancel out the light shift locally for all regions from the method described in section 4.3.2. Similar to the investigation of the magnetic field gradient, we investigate whether there is a position dependent light shift due to the inhomogeneous profile of the lattice potential.

The inhomogeneity of the 3D lattice or any combination of lattice beams is measured using the procedure described in section 4.4.1. Ramsey spectroscopy is performed with atoms only trapped in a chosen combination of lattice beams and the resultant Ramsey fringe data is analyzed in smaller sections to extract the local light shift. In order to extract only the light shift, the frequency shift due to the magnetic field gradient (see section 4.4.1) is subtracted from the data. Fig. 4.9 shows the light shifts due to the three lattice beams HDT1, HDT2 and HDT3. For both HDT1 and HDT3, we can see a gradient transverse to the beam propagation.

Fig. 4.10 shows a measurement of the coherence times for atoms trapped in only HDT1. The same measurement set is analyzed with different sizes of the region of interest, using Eq. 4.7 in order to extract the coherence time. As is evident from the fits, when we choose a smaller region of interest of 20×20

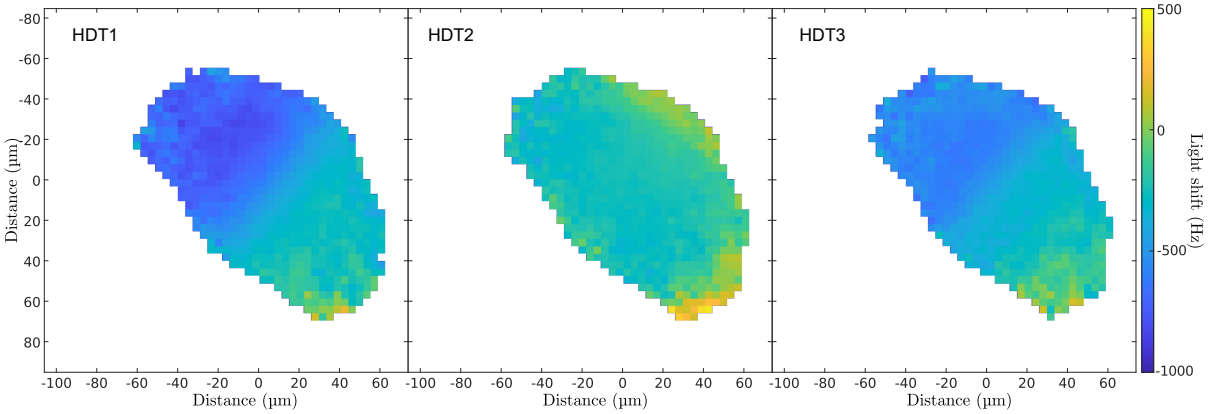

Figure 4.9: Inhomogeneities in the light shift induced by the three horizontal lattice beams. The light shifts are measured by performing Ramsey spectroscopy on atoms trapped in each of the lattice beams. Images obtained from the experiment are broken down into sections of size 10×10 pixels (3.6 μm×3.6 μm) and each of these sections is analyzed to extract the Ramsey phase.

lattice sites, we extract a larger coherence time (1.50 ± 0.12 ms) as opposed to the case where the entire image (≈170×170 lattice sites) is analyzed (0.80 ± 0.02 ms). These differences clearly indicate the need to choose a small region to perform our experiments. While the light shifts due to the individual beams may not seem large, they are more prominent when the three beams interfere to create the 2D lattice.

The Ramsey phase measured for each section lets us compute the shift in frequency between the states $|\uparrow\rangle$ and $|\downarrow\rangle$ with respect to the resonance condition in 'free-fall'. There is a noticeable gradient of light shift for beams HDT1 and HDT3, perpendicular to their direction of propagation. This could be a result of a non-zero ellipticity gradient. In contrast, we observe a more homogeneous light shift for HDT2, which propagates orthogonal to the beams HDT1 and HDT3, and being perpendicular to the quantization axis, it has zero polarization ellipticity.

A complementary measurement, where we extract the intensity variation (as opposed to differential light shift measurement with Ramsey) of our two-dimensional lattice is performed by spatially analyzing the microwave sideband spectrum. The difference in frequency between the carrier and the 1st order sidebands is the trap frequency, from which the trap depth can be computed. Hence, by analyzing the sideband position section-wise across the image, we can extract the change in local potential of the lattice, which corresponds to the change in intensity of the light field seen by the atoms. As we have discussed in section 3.1.2, our trap is not isotropic, hence we measure the two orthogonal trapping frequencies, along HDT1-3 and HDT2, as shown in Fig. 4.11.

The measurement procedure for microwave sideband spectroscopy is already discussed in section 3.4.3. We analyze the data section-wise with the size of each section corresponding to 10×10 lattice sites (3.6 μm×3.6 μm). Each of the three peaks of the sideband spectrum is fit with a Gaussian to extract the positions on the frequency scale. In Fig. 4.11, we plot the frequency difference between the position of the heating sideband and the carrier for the different analyzed sections. Although the cooling sideband could also be used for this measurement, it is typically much lower in amplitude than the heating sideband (for sideband cooled atoms that we use) and hence are prone to larger errors in determining the peak position. The inhomogeneity of the trapping frequencies across the analyzed data relates to an inhomogeneity in the trap depth. In Fig. 4.11(a) the lattice is opened along the direction of HDT1-3. One can see that the trap frequencies along the direction of HDT1-3 are homogeneous while there is a gradient transverse to

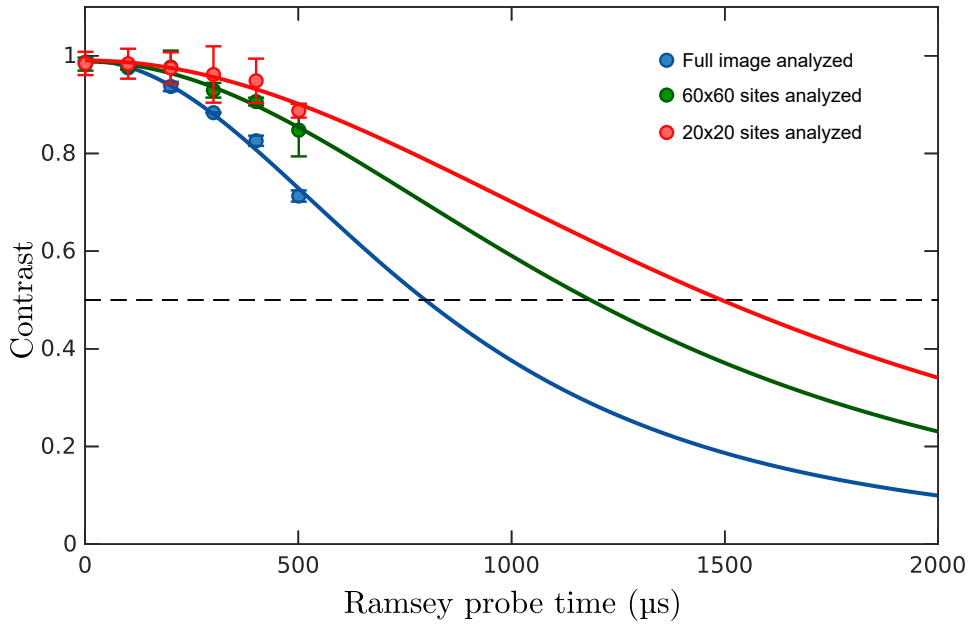

Figure 4.10: T_2 time measurement for atoms trapped in a running wave of HDT1. The three data sets correspond to the analysis performed in three different sized regions of interest (ROIs). We compare the contrast extracted from the Ramsey fringe fits for ROIs corresponding to 20×20 lattice sites (≈ 12 µm×12 µm), 60×60 lattice sites and the entire image (roughly 290×290 lattice sites). As expected from the inhomogeneous light shift distribution for HDT1 (see Fig. 4.9), we measure higher T_2 times as we decrease the region of interest.

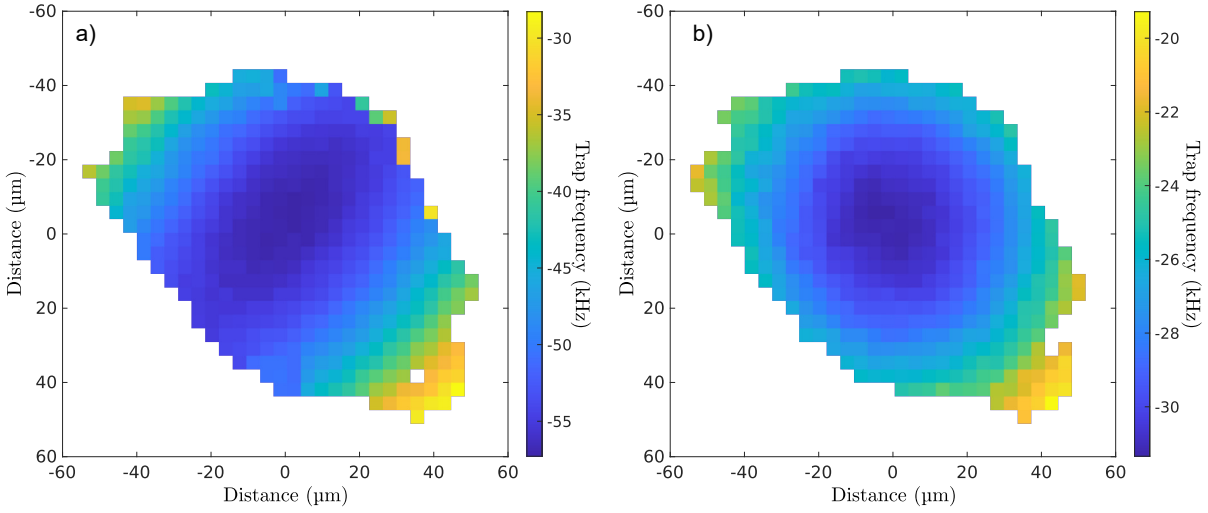

Figure 4.11: a) Spatial distribution of the trapping frequency along HDT1-3. Each pixel of this image corresponds to a size of 3.6 µm×3.6 µm. The trap frequencies are obtained by performing spatially resolved microwave sideband spectroscopy. The gradient of trap frequencies indicates the inhomogeneity of the trapping potential across the lattice. b) Spatial distribution of the trapping frequency along HDT2.

the two counter-propagating beams. This can be understood intuitively as the result of the homogeneity of the two lattice beams along their direction of propagation. Since the trap frequency along HDT1-3 results primarily from the interference of these two counter-propagating beams, the inhomogeneity in the trap frequencies follows that of the two beams. Likewise, the trap frequency along the direction of HDT2 also depends on the orthogonal beam, HDT2, resulting in a more isotropic gradient as can be seen in Fig. 4.11(b). The gradient in trap frequencies correspond to the change in trap depth from around 540 kHz at the center to around 300 kHz on the flanks.

The variation in trap depth underlines the need to only use a small region in the center of the trap where we have a homogeneous depth. Furthermore, we also learn that such a large variation in trap frequencies makes our sideband resolved microwave cooling ineffective for atoms that trapped on the flanks. In the sideband cooling scheme, we set the microwave frequency to the frequency of the cooling sideband that we extract from the spectrum. However, as we can see from Fig. 4.11, setting the microwave to just one frequency will not fulfill the cooling condition for all the atoms at once. Therefore, we need to devise a new scheme to cool all the atoms, for example, sweeping the microwave frequency over the range of trap frequencies that we measure. In retrospect, we believe this inhomogeneity limited us from optimizing our 3D cooling to its full potential. In order to find out the coherences we can achieve in a small region of the lattice, we perform a spatially resolved analysis of the T_2 time measurements for atoms trapped in the two-dimensional lattice created by the three horizontal beams: HDT1,HDT2 and HDT3, as shown in Fig. 4.12(a). For comparison, Fig. 4.12(b) shows the T_2 time measured when analyzing the entire image, corresponding to around 223 µs . In Fig. 4.12(a) we see that the coherence time of our qubit is much longer when we work in a small region of interest, reaching up to 1.5 ms.

In conclusion, we have demonstrated that the spatial inhomogeneities in our lattice are the limiting factors to achieving higher coherence times. There exist methods to suppress such inhomogeneous dephasing. For instance, dynamical decoupling [161, 162] has been shown to be a promising strategy for combating decoherence [163–167], where stroboscopic spin flips are applied in order to have an average coupling to the environment that is effectively zero. Another method to overcome inhomogeneous dephasing relies on introducing an additional light field to compensate for the differential light shifts caused by the trap [168–170]. Insofar as our near term experimental goals are concerned, it will suffice to work in a smaller region of interest.

Spin echo

While in the previous section we have shown that working in smaller patches alleviates the dephasing when compared to the entire image, there is a diagnostic tool to learn complementary information, where we 'reverse' this inhomogeneous dephasing : the spin echo [171]. Spin echoes have been successfully used in neutral atom experiments [146, 172–176]. For the spin echo measurement, we introduce a π-pulse between the two $\pi/2$-pulses of the Ramsey spectroscopy sequence described in section 4.1. The effect of adding a π-pulse in the middle of the free evolution is equivalent to a $t \rightarrow -t$ transformation and therefore, all the inhomogeneous dephasing sources are canceled by the time of the final $\pi/2$-pulse. On the Bloch sphere (see Fig. 4.1), the π-pulse corresponds to a rotation of the Bloch vector by 180° around the u-axis. The spin echo rephases all the dephasing caused due to inhomogeneities that do not vary in time. In Fig. 4.13, the results of the spin echo measurement are shown for atoms trapped in a 3D lattice. The Ramsey probe time here corresponds to the duration between the two $\pi/2$-pulses in the sequence. We extract an irreversible dephasing time of 4.5 ms, which is almost an order of magnitude better than what was reported by the earlier generation of this experiment [107].

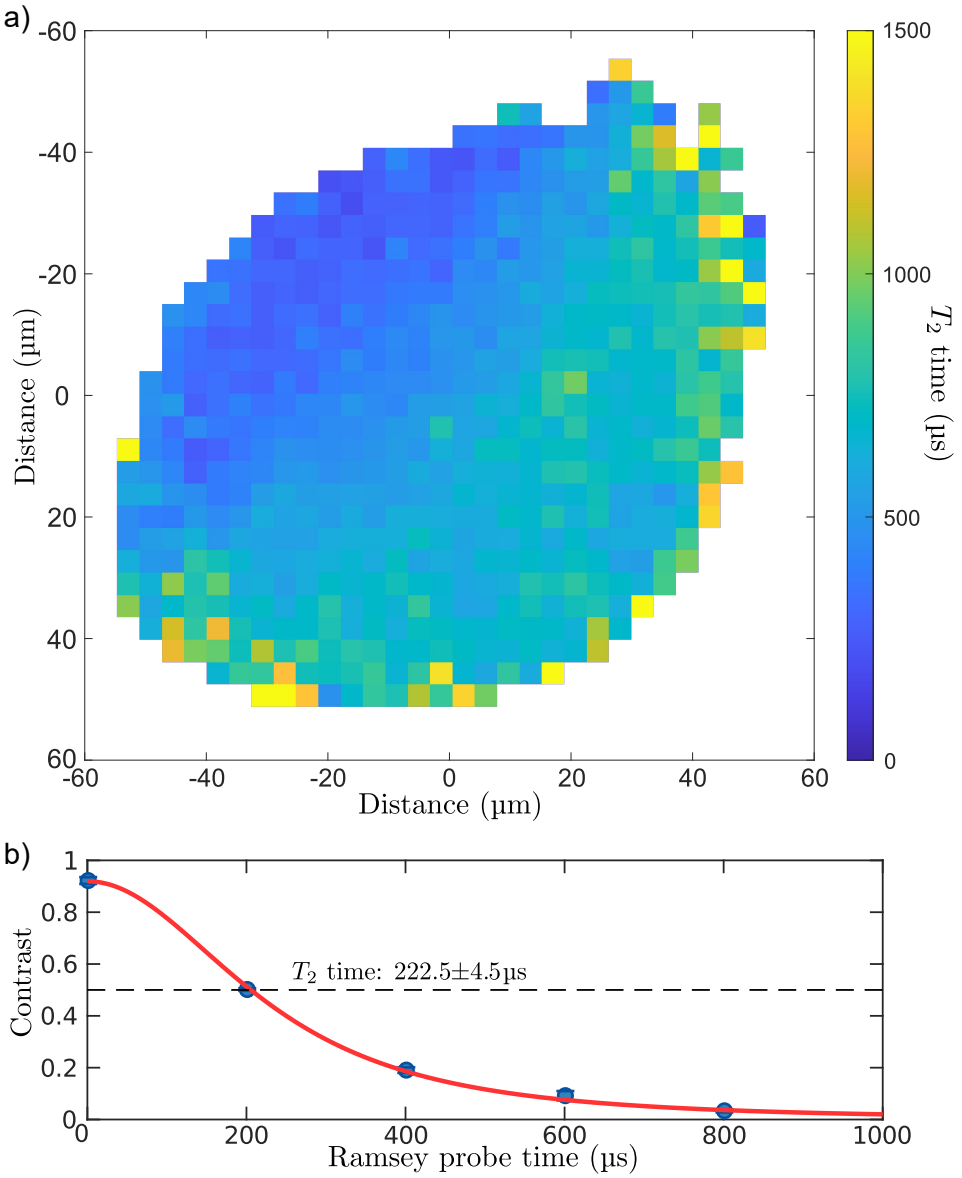

Figure 4.12: a) Spatial analysis of the coherence time in a 2D lattice created by the interference of the three horizontal dipole trap beams, HDT1, HDT2 and HDT3. Each pixel of the image is of size $\Delta x_p \approx 3.6\,\mu$m. The T_2^* time is extracted for each pixel by analyzing the contrast of the Ramsey fringe for that pixel for different Ramsey times. The plot indicates a gradient in the coherence of different patches, showing that we can achieve a T_2 time as high as 1.5 ms if we work within a small region of interest of the lattice. b) Coherence time measurement when the entire image in (a) is analyzed. The T_2 extracted from the fit (red line) based on Eq. 4.7 is 223 µs. This drop in contrast can be explained by the smearing out of the Ramsey fringe due to the inhomogeneous phase shifts across the entire image, leading to a drop in contrast of the fringe.

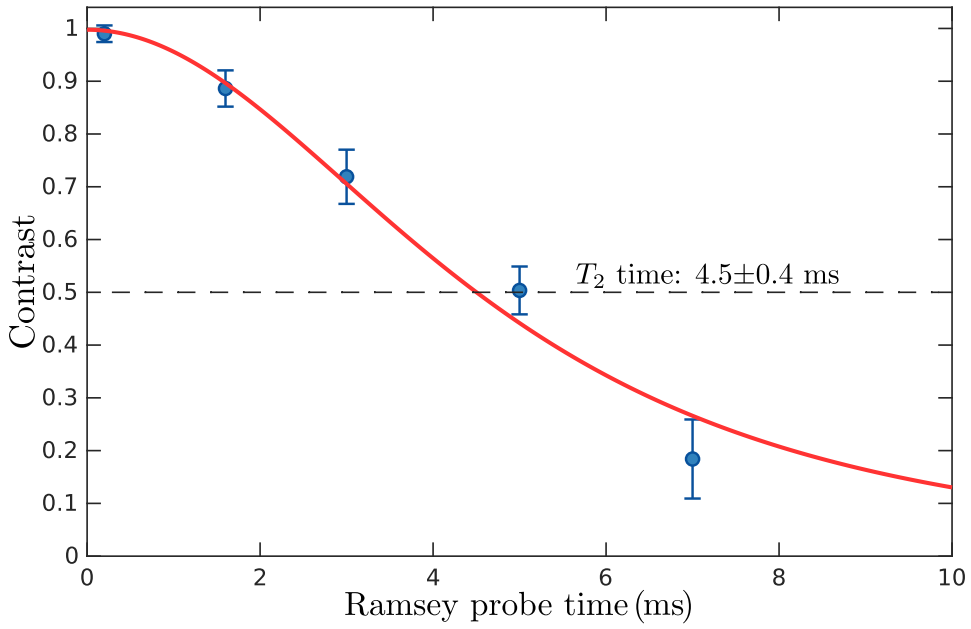

Figure 4.13: Coherence time measurement with a spin echo pulse introduced between the two $\pi/2$ pulses of the Ramsey sequence. The measurement is performed for different Ramsey times and fit with a model introduced in [130] (red line), yielding a T_2^{echo} time of 4.5 ± 0.4ms (time between the two $\pi/2$ pulses). The atoms are trapped in a two-dimensional lattice constructed from the interference of beams HDT1, HDT2 and HDT3.

4.5 Coherence in the vertical optical lattice

While the horizontal two-dimensional lattice is created by the interference of three beams tuned to a wavelength of 866 nm, the atoms are vertically trapped in the third dimension, in a 1D lattice created by a beam (at 1 064 nm) retro-reflecting on the surface of our microscope objective. We don't expect the light shift effects of this beam to be as prominent due to its large detuning, as opposed to the horizontal beams. Referring to Eq. 4.12 and Eq. 4.13, the values for the scalar and vectorial components for the light shift are

$$\eta_s = 1.48 \times 10^{-4}$$
$$\eta_v = -0.16$$

These values are an order of magnitude smaller than the corresponding values for the horizontal lattice beams. Furthermore, since the vertical lattice is propagating orthogonal to the quantization axis, the σ^+ and σ^- components are always equal. Therefore we don't expect any vectorial light shift contribution. A transverse profile of the vertical lattice has been imaged using Ramsey spectroscopy (see chapter 5), so we know already that the finite extent of a beam will lead to a gradient of light shifts as we move away from the center of the beam. Apart from contributing to dephasing, this also has a detrimental effect on our sideband cooling efficiency along the vertical direction, more of which is discussed in [109]. Fig. 4.14 shows a spin echo measurement for atoms trapped only in the vertical lattice. The small peaks in the contrast, as we see in the plot, have not been thoroughly investigated yet, however we believe it has to do with the transverse motion of the atoms in an inhomogeneous magnetic field, similar to what has been reported in Schrader et al. [177].

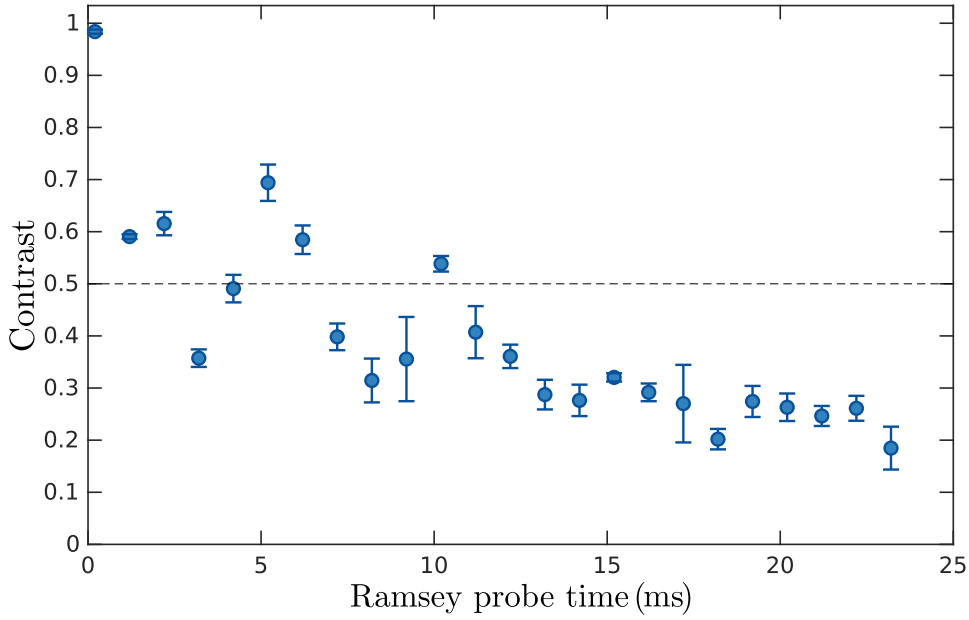

Figure 4.14: Coherence time measurement for atoms trapped in the vertical lattice (VDT), obtained by performing a spin echo sequence for different Ramsey probe times. The revival of the contrast has not been thoroughly investigated yet. We suspect it is because of the transverse motion of atoms in an inhomogeneous magnetic field, similar to what has been reported in Schrader et al. [177]

4.6 Statistical analysis of Ramsey fringe

In this section, I will present a technique where, from analyzing the statistics of a Ramsey spectroscopy measurement, we get rid of all homogeneous dephasing mechanisms, and are only sensitive to inhomogeneous dephasing mechanisms. This technique is complementary to spin echo analysis, where static inhomogeneous dephasing is removed and one can extract the homogeneous contribution from the contrast loss.. The idea behind this measurement is to look at the probability distribution of the survival of atoms in a Ramsey fringe, where the microwave phase is scanned from 0 to 2π . For a given phase ϕ of the second microwave pulse, the probability that we detect an atom after a Ramsey sequence is given by Eq. 4.4

$$p(\phi, S, C) = \frac{S}{2}[1 + C\cos(\phi)], \tag{4.23}$$

where C is the contrast and S the survival probability of atoms when no push-out pulse is applied. The probability of a detection is binomial distributed, since there are only two possible outcomes: the atom is either detected or it is not. Out of the total number of trials N_0, the probability of k detections is given by

$$f(N_0, k, p) = \binom{N_0}{k} p^k (1-p)^{N_0-k}, \tag{4.24}$$

where p is the function defined in Eq. 4.23. The distribution above corresponds to the probability at a single phase point ϕ. The probability for k successes from N_0 trials, when the phase of the second

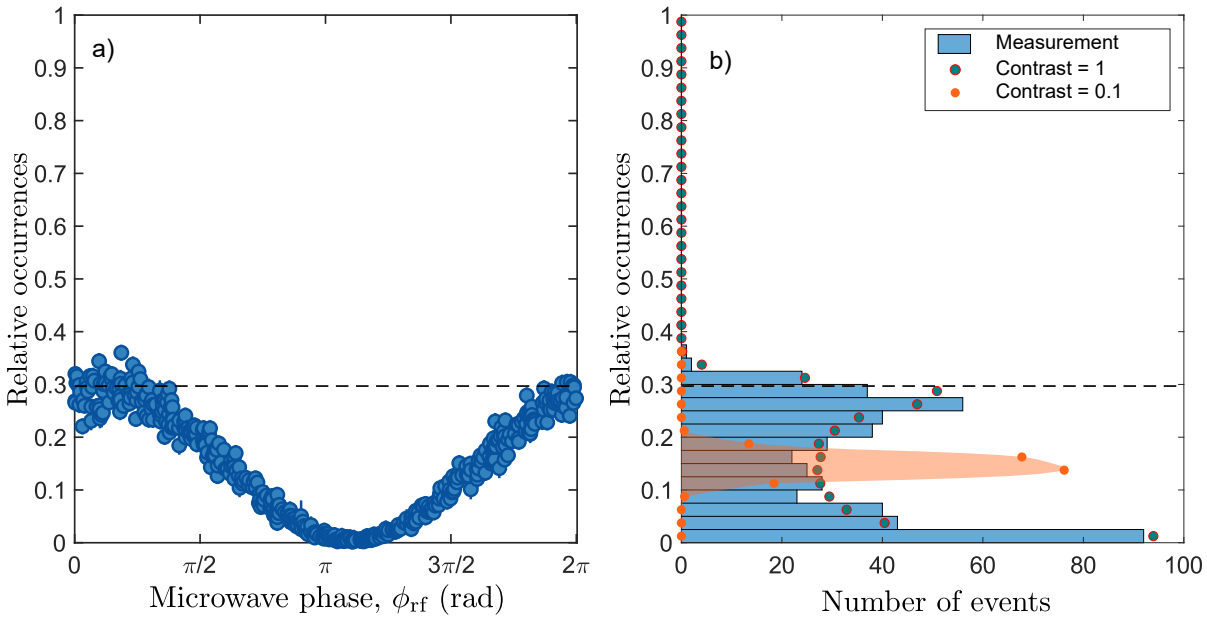

Figure 4.15: a) Measured signal of a Ramsey spectroscopy sequence, with probe time of 100 µs, for randomly chosen phase ϕ_{rf} of the second $\pi/2$ pulse. The scatter of the relative occurrences for a given phase ϕ_{rf} are attributed to dephasing mechanisms, and the resultant Ramsey model fit to the data would have a drop in contrast. b) A histogram of the relative occurrences for the data in a). The model in Eq. 4.26 is manually fit to the histogram, resulting in a contrast of 1. The average number of atoms per shot is $N_0 = 350$. For comparison, the expected distribution for a contrast of 0.1 shown (shaded in orange for better visibility).

$\pi/2$-pulse can take any value in the interval $[0,\pi]$, is given by

$$F(N_0, k, p) = \int_0^{\pi} \binom{N_0}{k} p^k (1-p)^{N_0-k} \, d\phi \tag{4.25}$$

In a single run of the Ramsey sequence, many atoms are loaded into the lattice, with the atom distribution follows poissonian statistics. If we assume that N_0 is the average number of atoms loaded in a run of the sequence, the probability of k detection events occurring, corresponding to N_k atoms is

$$\frac{N_k}{N_0} = \sum_{N=N_0-4\sigma}^{N_0+4\sigma} e^{-N_0} \frac{N_0^N}{N!} F(N_0, k, p) \tag{4.26}$$

where σ is the standard deviation, which for large N_0 can be approximated to $\sqrt{N_0}$.

To understand how such a distribution helps us extract the contribution of the inhomogeneous dephasing, let us first consider a Ramsey fringe such as in Fig 4.12. If we bin the relative population of $|\downarrow\rangle$ (y-axis in the figure) and plot a histogram of occurrences in each bin, we would expect a double peaked structure with a high number of counts around a relative survival of 0 and 1. This can be deduced from the fact that the slope is highest around a relative survival of 0.5 and almost flat around a relative survival of 0 and 1. As the contrast decreases, the peaks start moving towards the center and their height decreases until eventually for zero contrast we have a sharp peak at 0.5 relative survival (the Ramsey fringe would be a line at 50% relative population in $|\downarrow\rangle$). In Eq. 4.26, N_k corresponds to the number of counts in a bin

centered at k relative population in $|\downarrow\rangle$. Therefore, by plugging in different values of k from 0 to 1 in Eq. 4.26, we can reproduce the histogram and try to fit it to our measurements by tuning the contrast C (see Eq. 4.23).

The experimental sequence consists of performing Ramsey spectroscopy multiple times, each time choosing a random phase ϕ for the second $\pi/2$-pulse, as shown in Fig. 4.15(a). Finally we analyze the relative survival from all the runs and bin them to generate a histogram, as shown in Fig. 4.15(b). We then try to fit the histogram with the distribution in Eq. 4.26 by tuning the contrast (all other values are known). It must to noted that the asymmetry of the double peaked structure in Fig. 4.15(b) arises due to losses in a finite sample of atoms probed. This low survival also causes the tail we notice towards higher relative occurrences, due to fluctuations in the background survival. In the limit of infinite atoms, we expect the double peaked structure to be symmetric with sharp cut-offs at both the upper and lower peak.

Such a measurement is not affected by homogeneous dephasing since we are inspecting the survival statistics and not the phase of a Ramsey fringe. When performing the typical Ramsey spectroscopy to measure the coherence time, homogeneous dephasing causes a shot to shot fluctuation between two measurements, which leads to shifts of the Ramsey fringe and eventually smear out the Ramsey fringe signal. However, in this measurement, we don't require any phase coherence between the different runs of the sequence. Any shift in the Ramsey fringe can be interpreted to be accounted for by the random phase ϕ of the second $\pi/2$-pulse. On the other hand, inhomogeneous dephasing plays a role in changing the statistics of this measurement. Since in inhomogeneous dephasing, within one shot itself, atoms accumulate different phases, there will never be a case where all atoms are in either state $|\uparrow\rangle$ or $|\downarrow\rangle$ after the second $\pi/2$-pulse. Hence the relative survival never reaches 1 or 0. This corresponds to a reduction in the contrast for the histogram analysis we have discussed above. Hence, this measurement reveals the reversible dephasing time of our system, making it a good complement to the spin echo, where we measure the irreversible dephasing time. On analyzing the histogram for data taken at a longer Ramsey probe time of 1 ms, we see a drop in contrast to $\approx$70%. This drop in contrast indicates a shorter dephasing time from inhomogeneous contributions versus the homogeneous contribution we measure with spin echo.

4.7 Summary

In this chapter,using Ramsey spectroscopy as a tool, I have investigated some possible sources of decoherence. By performing Ramsey spectroscopy on atoms in free fall, we are able to measure the magnetic field inhomogeneity across the lattice, caused by the electromagnets generating the bias field. Furthermore, using atoms as a Ramsey magnetometer, we measure the magnetic field drifts in our system, and show that their negligible contribution to dephasing. I performed an in-situ measurement of the birefringence of the new ultra high vacuum cell using atoms as probes. The birefringennce measured is around an order of magnitude lower than that of the commercial fused-silica ultra-high vacuum cell used in the 1D quantum walk experiment, the predecessor to our experiment. Furthermore, by controlling the polarization ellipticity of the dipole beams, we are able to tune the vectorial light shifts to compensate for the scalar light shift, in order to minimize inhomogenous dephasing.

In the second half of this chapter, I discuss position resolved measurement of the coherence time, showing that inhomogeneities of the optical lattice are the limiting factor for long coherences times in our system. I show that by choosing regions of interest of size $\Delta x_p \approx 3.6\,\mu$m, we can achieve coherence times of the order of a millisecond. Finally, I also characterize the inhomogeneous dephasing in our system by statistically analyzing the Ramsey fringe. All the relevant coherence times in our system are tabulated in Table 4.2.

Description	T_2 time
Coherence time limited by magnetic field fluctuations	~4 ms
Coherence time in the absence of vectorial light shifts	~6 ms
Coherence time in a region of interest of size 10×10 lattice sites	~1.5 ms
Reversible dephasing time (T_2^*) in the 2D lattice	~4.5 ms
Reversible dephasing time (T_2^*) in the vertical lattice	~10 ms

Table 4.2: Relevant coherence times in our experiment. The measurements corresponding to these values are discussed in the text.

CHAPTER 5

Ramsey imaging of optical dipole traps

Precise knowledge of the optical trap potentials is essential for ultra-cold atom enabled quantum technologies, ranging from simulating model Hamiltonians, to extremely sensitive sensors and ultra-precise clocks [15, 24]. Most of these experiments rely on the clean and controllable trapping potentials generated by laser beams; however, they face a difficult challenge in precisely characterizing the geometry of these beams inside the inaccessible ultrahigh vacuum chamber, where atoms are trapped and manipulated. The precise alignment of the dipole trap laser beams is especially crucial for multi-beam setups (e.g., optical lattices) in order to minimize spatial inhomogeneities of the confining potential [178].

The majority of available techniques for reconstructing the local trapping potential are restricted to optical lattices, where the position-resolved shift of either motional sidebands or of parametric heating resonances is detected and related to the local light field intensity. Importantly, such procedures require an accurate prior knowledge of the laser beams' parameters and geometry. Only recently, *in-situ* imaging of an optical dipole trap has been demonstrated [179] by probing the differential light shift induced upon an ultranarrow optical transitions of alkali-earth atoms. While well suited to atomic species with narrow optical transitions, this method is not applicable to other species, such as alkali atoms, which are commonly used for quantum simulations and quantum computing. Hitherto, there is no simple in-situ technique to accurately image the trapping potential produced by a single running wave, without relying on a narrow optical transition.

In this chapter, I present an experiment where optical dipole trap beams are imaged with micrometer spatial resolution, by subjecting a small ensemble of atoms to a controllable amount of polarization ellipticity. Owing to the polarization ellipticity, atoms experience a differential light shift, which to first order is proportional to the dipole potential at the location of the atoms. Using Ramsey interferometry, we are able to image the optical dipole trap potential with optical wavelength resolution, and a spectral resolution two orders of magnitude below the Fourier limit $\nu_F = 1/t$, where t is the interrogation time. The high precision of the Ramsey technique also allows us to probe a non-linear response of the atomic ensemble to the ellipticity. We enhance the accuracy of the imaging protocol by developing a non-linear model to account for this systematic shift in the measured phase of the Ramsey interferometric fringe, which is caused by an inhomogeneous dephasing of the ensemble of atoms.

This imaging technique is demonstrated by extracting accurate information about the geometric parameters of each individual optical dipole trap. This allows us to align all four laser beams, forming a three-dimensional optical lattice, with wavelength precision. Using an ensemble of cesium atoms, we exemplify its versatility by imaging the potential created by single laser beams at different wavelengths λ: close to the fine structure D doublet (866 nm) and far detuned from it (1064 nm). In general, this

experiment can be performed with any atomic species possessing two long-lived states that are suited for Ramsey spectroscopy and an optical dipole transition from these states involving a nonvanishing spin-orbit interaction.

5.1 Conceptual scheme

In an optical dipole trap, the differential light shift between the two long-lived states $|a\rangle$ and $|b\rangle$ is proportional to $U(\vec{r})$, the trapping potential experienced by atoms at position $\vec{r}$. To reconstruct the potential, we take advantage of the dependence of the light shift on the ellipticity ϵ of the polarization of the trapping laser beam, which we can easily control

$$\delta(\vec{r}, \epsilon) = (\eta_s + \eta_v \epsilon) U(\vec{r})/h. \tag{5.1}$$

Here, η_s is the constant factor accounting for the scalar contribution to the differential light shift [130], η_v is a constant factor accounting for the vector contribution to the differential light shift [157], and h is the Planck constant. The two factors η_s and η_v depend only on the atomic properties and wavelength λ. The polarization ellipticity is defined as $\epsilon = (I_R - I_L)/(I_L + I_R)$, where I_L and I_R are the intensities of the left and right circular polarization components of the dipole trap laser beam.

The key idea behind imaging the dipole traps consists in transforming the polarization of the dipole trap laser beam from linear into elliptical (Fig. 5.1a), and measuring the differential light shift between $|a\rangle$ and $|b\rangle$, given by Eq. 5.1. A precise measurement of this shift is performed by Ramsey interferometry (Fig. 5.1c). By measuring the light shift $\delta(\vec{r})$ for two (or more) values of ϵ (Fig. 5.1e), it is straightforward to derive, by linear extrapolation, the vector light shift, $\delta_{v,\pm}(\vec{r}) = \pm\eta_v U(\vec{r})/h$, corresponding to a pure circular polarization, $\epsilon = \pm 1$. The dipole potential at position $\vec{r}$ is thus $U(\vec{r}) = \pm h\delta_{v,\pm}/\eta_v$, where the constant and polarization independent offset contribution from η_s has been accounted for. This relation shows that the vector polarizability, η_v, plays the role of the sensitivity factor of the Ramsey imaging technique, meaning that larger values of η_v leads to a more precise determination of the dipole potential.

Ramsey spectroscopy is well-suited for measuring the light shifts because the Ramsey signal can be very precisely modeled, amounting to fitting a cosine function (see Eq. 5.4), which depends on the phase and contrast. All dephasing effects in a Ramsey measurement contribute to a systematic shift in the phase and a reduction in contrast of the Ramsey fringe, while maintaining the cosinusoidal profile. In comparison, modeling a microwave spectrum is more involved, where the line shape depends on the shape of the microwave pulse and the temperature of atoms. To validate the statistical significance of the Ramsey model, we analyze the distribution of residuals of the least-square estimator used to obtain the physical parameters characterizing the Ramsey fringe. The histogram of the residuals derived from $> 10^4$ Ramsey fringes corresponding to one of the dipole trap beams shows a remarkable agreement with the theoretical distribution of a χ^2-distributed variate (Fig. 5.1d), given by the expression

$$f(x; k) = \frac{x^{\frac{k}{2}-1} e^{-\frac{k}{2}}}{2^{\frac{k}{2}} \Gamma(k/2)} \tag{5.2}$$

for k degrees of freedom, evaluated at value x. This agreement allows us to interpret the estimated fringe parameters as the most likely ones, meaning those that maximize the likelihood function, and thus in the limit of large data sets maximize the Fisher information.

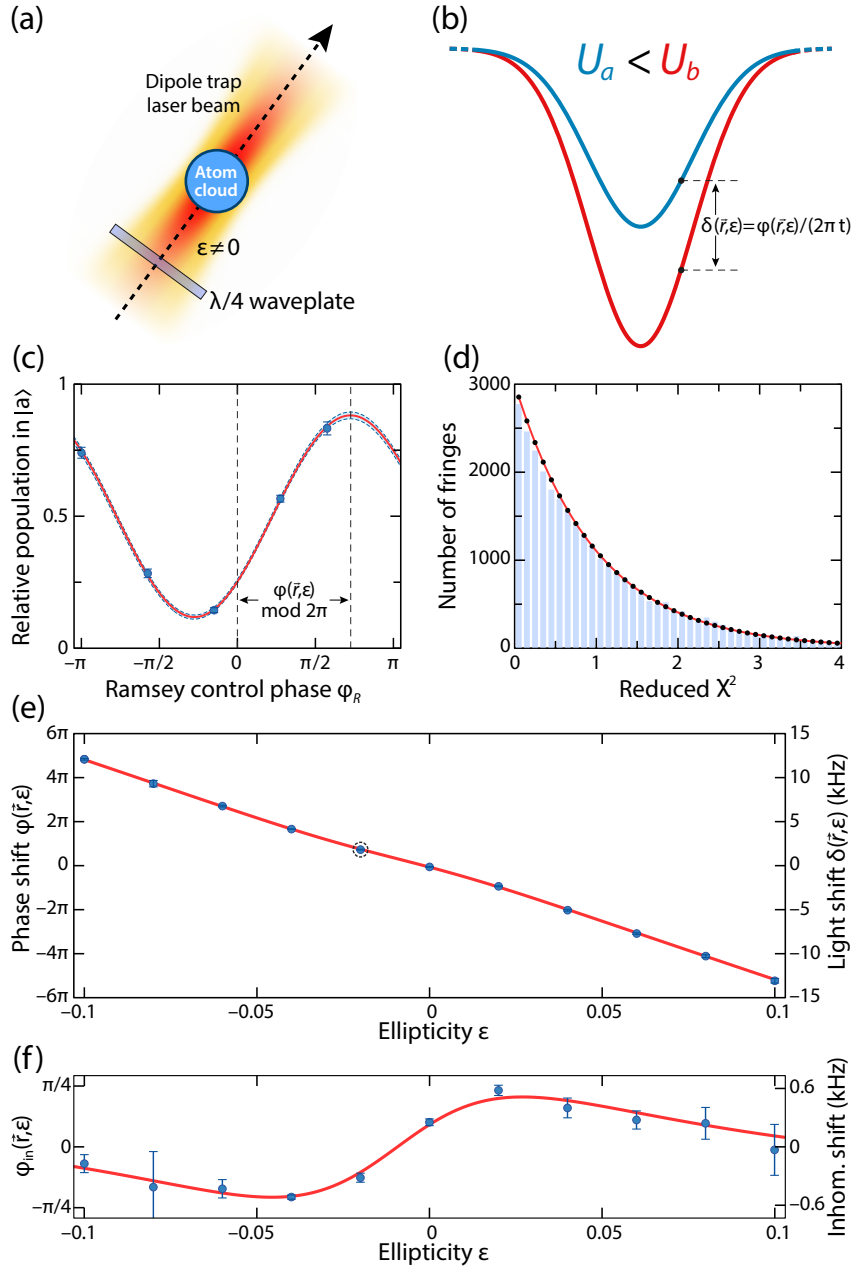

Figure 5.1: Dipole potential reconstruction by position-resolved phase tracking. (a) The dipole trap laser beam to be imaged is elliptically polarized ($\epsilon \neq 0$) before impinging onto the atom cloud. (b) The dipole potentials $U_a(\vec{r})$ and $U_b(\vec{r})$ experienced by atoms in states $|a\rangle$ and $|b\rangle$ differ by $h\delta(\vec{r})$ due to the nonzero ellipticity. In a Ramsey detection scheme, a position-dependent phase $\varphi(\vec{r},\epsilon) = 2\pi\delta(\vec{r},\epsilon)t$ is accumulated during a time t between the two states. (c) A typical Ramsey interference fringe showing the population $P_a(\vec{r},\epsilon,\varphi_R)$ as a function of the control phase φ_R, which is the relative phase between the two $\pi/2$ pulses, allowing the phase $\varphi(\vec{r},\epsilon)$ to be precisely tracked. (d) The distribution of reduced χ^2 values for all the Ramsey fringes analyzed for beam H3. This is in very good agreement with the theoretical expectation (solid line), validating the accuracy of the Ramsey imaging technique. (e) Measurement of the differential light shift at a given position $\vec{r}$ [see marked pixel in Fig. 5.2c] as a function of the ellipticity; the vertical offset is attributed to the scalar light shift $h\delta_s(\vec{r}) = \eta_s U(\vec{r})$. The Ramsey duration is set to 200 µs. The circled point corresponds to the Ramsey fringe in (c). (f) The non-linear contribution to the differential light shift, attributed to a finite thickness of the atomic sample along z (see text). This is represented by subtracting the linear contribution extracted in (e).

	^{133}Cs	^{87}Rb	^{23}Na
η_v	-0.16	-0.04	-1×10^{-3}
η_s	1.5×10^{-4}	6.8×10^{-5}	7.8×10^{-6}

Table 5.1: Reference values of η_v and η_s for a far-detuned dipole trap at 1064 nm. η_v is calculated for the maximally stretched hyperfine states of the electronic ground state for the given elements.

Alkali atoms

We consider the situation for the widely used alkali atoms, and choose two hyperfine states $|a\rangle = |F, m_F\rangle$ and $|b\rangle = |F', m'_F\rangle$ of the electronic ground state, where F and F' denote the quantum numbers of the total angular momentum of the atom, whereas m_F and m'_F represent the corresponding magnetic quantum numbers, with the quantization axis aligned in the direction of the laser beam we intend to image. Following a straightforward calculation [122], we obtain the following expression for the sensitivity (see Appendix B),

$$\eta_v = (g'_F m'_F - g_F m_F)\frac{\nu_2 - \nu_1}{3\nu - 2\nu_1 - \nu_2}, \tag{5.3}$$

where g_F and g'_F are the Landé factors of the states $|a\rangle$ and $|b\rangle$, ν_1 and ν_2 are the resonance frequencies of the D_1 and D_2 lines, and $\nu = c/\lambda$ is the frequency of the laser beam (c is the speed of light).

We note here that the vector light shift is nonzero ($\eta_v \neq 0$) for all transitions with the exception of clock-type transitions (when $g'_F m'_F = g_F m_F$). Moreover, because the Ramsey imaging technique leverages the atomic spin-orbit interaction, which for alkali atoms occurs in the p orbitals, its sensitivity factor η_v is directly proportional to the fine structure splitting, $\nu_2 - \nu_1$, which is larger for heavier atoms. For the same reason, the sensitivity increases for wavelengths closer to the fine structure, when the atomic spin-orbit interaction is resolved with higher precision.

Reference values for the differential polarizabilities η_s and η_v for a few commonly used alkali atoms are shown in Table 5.1. These values are computed for a far-detuned dipole trap at 1064 nm, where $|a\rangle$ and $|b\rangle$ are respectively chosen to be the doubly polarized and maximally stretched states for maximal η_v. The scalar contribution to the light shift is smaller as it originates from the hyperfine interaction.

5.2 Optical potential reconstruction

To demonstrate the Ramsey imaging of dipole traps, we individually reconstruct the dipole potential produced by four laser beams: three beams (H-beam-n with n=1, 2, 3) are tuned at 866 nm and propagate in a common horizontal plane, whereas the fourth beam (V beam) is tuned at 1064 nm and forms an optical standing wave in the vertical direction. The four laser beams are overlapped to form a three-dimensional (3D) optical lattice, as detailed in [68].

For each of the generated dipole traps to be imaged, the experimental sequence begins by loading an ensemble of a few thousand cesium atoms from a magneto-optical trap into the 3D optical lattice. The procedure of loading the lattice is performed in such a way as to have the atoms distributed over a relatively large region (60 µm×60 µm), covering ≈ 90% of the laser beams' cross section. Subsequently, we reduce the temperature of atoms to $T \approx 1$ µK by employing resolved sideband cooling techniques in all three dimensions.

Before conducting the Ramsey measurement of the differential light shift, we set the polarization ellipticity of the dipole trap laser beam we intend to image by inserting a quarter-wave plate in the beam

path, as illustrated in Fig. 5.1(a). The ellipticity ϵ can be measured with standard ellipsometry methods, e.g., using a rotating polarizer. Alternatively, we use a digital polarization synthesizer (see sec 3.2) to control the ellipticity, as for the imaging of H-beam-1 and H-beam-3.

For a fixed value of ellipticity ϵ, we perform Ramsey spectroscopy of the energy difference between the two states $|a\rangle = |F = 3, m_F = 3\rangle$ and $|b\rangle = |F = 4, m_F = 4\rangle$; see Fig. 5.1b. We begin by optically pumping the atoms into state $|b\rangle$, followed by adiabatically aligning the quantization axis in the direction of the laser beam to be imaged by rotating the bias magnetic field (of about 3 G) with three pairs of compensation coils.

After turning off all dipole trap laser beams except the one relevant for the image, the Ramsey sequence consisting of two $\pi/2$ pulses (of duration 1.5 μs) separated by a fixed interrogation time $t = 200\,\mu s$ is started. For the Ramsey pulses, we employ resonant microwave radiation; alternatively, one could use resonant optical Raman transitions[1].

The Ramsey signal

$$P_a(\vec{r}, \epsilon, \varphi_R) = \frac{1}{2} - \frac{C_0}{2} \cos[\varphi(\vec{r}, \epsilon) - \varphi_R] \tag{5.4}$$

is mapped onto the population distribution of atomic states $|a\rangle$ and $|b\rangle$. We perform state-selective detection of the density of atoms by removing atoms in state $|b\rangle$ with an optical push-out pulse, and then acquire a fluorescence image of the remaining atoms in state $|a\rangle$ through a high-numerical-aperture imaging system [58].

The imaging axis is directed along the vertical direction, therefore we can only spatially resolve the images on the horizontal x-y plane. We rewrite the position coordinate $\vec{r} = (\vec{\rho}, z\hat{e}_z)$, where $\vec{\rho} = (x, y)$ corresponds to a position on the x-y plane. The Ramsey signal is analyzed for each square pixel at position $\vec{\rho}$, where the relative population in state $|a\rangle$ exhibits a characteristic fringe as a function of the Ramsey control phase φ_R, which can be varied precisely by controlling the relative phase between the two $\pi/2$ pulses. In the expression (5.4) of the Ramsey fringe, C_0 denotes the contrast and $\varphi(\vec{\rho}, z, \epsilon) = 2\pi\delta(\vec{\rho}, z, \epsilon)t$ is the phase accumulated during the interrogation time t, in the rotating frame of the microwave field set to the resonance frequency between $|a\rangle$ and $|b\rangle$ for the given bias magnetic field. It is directly related to the differential light shift of Eq. 5.1.

For our analysis, we choose the pixel size $\Delta x_P \approx 3.6\,\mu m$, corresponding to 10 pixels of the EMCCD camera. It is important to note that owing to the nonvanishing kinetic temperature T, the atoms move on average by $\Delta x_K \approx 1\,\mu m < \Delta x_P$ during the Ramsey t. Depending on the target spatial resolution of the reconstructed dipole potentials, the thermal motion of atoms constrains the maximum Ramsey interrogation time t, which in turn affects the spectral resolution which scales with the Fourier limit ν_F. Thus, for a given temperature T, there is a trade-off between the spectral and spatial resolution that can be achieved by the Ramsey imaging technique presented in this work. Furthermore, it must also be noted that any non-zero ellipticity causes a differential force on the states $|a\rangle$ and $|b\rangle$, leading to a displacement between the two wave-packets. This can lead to a reduction in contrast of the Ramsey fringe, to the point that determining the phase becomes imprecise. However, this effect of the differential force is negligible in our case.

Figure 5.2 shows the potentials of the four dipole traps, reconstructed pixel by pixel from the spatially resolved Ramsey signal of Eq. 5.4 . Fig. 5.2(a-c) are potentials associated with the laser beams in the horizontal plane, forming a T-shaped geometry, while Fig. 5.2(d) corresponds to the transverse potential landscape of the V-beam which traverses along the line of sight. Fig 5.2(d) clearly shows that the V-beam is off-centered by around 16 µm from the intersection point of the three horizontal beams axes, illustrating

[1] Possible spatial inhomogeneities of the intensity of the Raman beams would have no systematic effect on thereconstructed dipole potentials

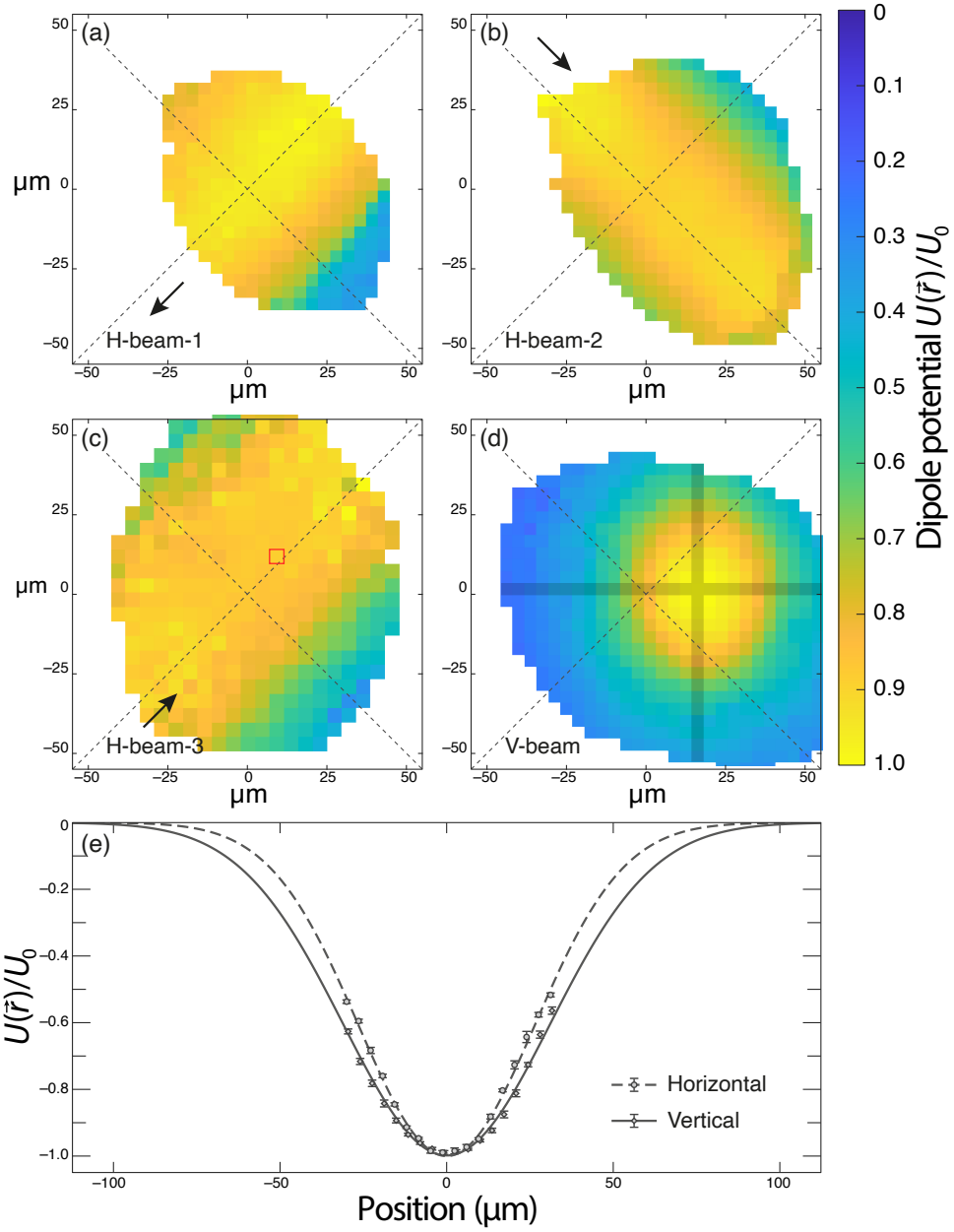

Figure 5.2: Ramsey imaging of four optical dipole traps produced independently by (a-c) three running waves at $\lambda = 866\,\text{nm}$ propagating in different directions lying in a common plane and (d) a standing wave at $\lambda = 1\,064\,\text{nm}$ oriented in the same direction of the imaging system. For convenience, a common axis system is represented by the dashed lines. No signal is shown in the outlying region because only a few or no atoms are loaded there from the magneto-optical trap. The arrows in (a-c) indicate the propagation direction of the running wave creating the dipole potential. A vertical and horizontal line of pixels is highlighted in (d), corresponding to the two axes of the elliptical beam shape, caused by astigmatism. The cross-section of the reconstructed potential along these axes is shown in (e). Each data point corresponds to a single pixel of the Ramsey image. The solid (dashed) lines show the Gaussian profile fitted to the data along the vertical (horizontal) cross-section. Note that the reconstructed potential $U(\vec{r})$ represents here the average over the line of sight weighted with the atom density (see text).

Laser beam	Waist (μm)	Position uncertainty (μm)
H-beam-1	82.25 ± 1.46	±0.43
H-beam-2	71.53 ± 0.31	±0.18
H-beam-3	76.53 ± 0.64	±0.75
V-beam-X	52.99 ± 0.54	±0.16
V-beam-Y	61.99 ± 0.83	±0.22

Table 5.2: Reconstructed waists of the four imaged dipole-trap laser beams shown in Fig. 5.2, whose intensity profile is nearly Gaussian. For the V-beam, which has a slightly elliptical shape, the waist for both astigmatic axes is reported. For the beam axis position, only its uncertainty is reported.

the capacity of our method to align optical beams at an inaccessible point in space with sub-μm precision. In addition to the horizontal lattice beams at 866 nm, we also show that this technique is applicable to imaging a far-detuned lattice beam at 1064 nm, as shown in Fig.5.2(d). Once we have a two-dimensional image of the laser beams, we can take a transverse cross-section to extract the beam waist, tabulated in Table 5.2. An exemplary fit for transverse cuts along the two principal axes of V-beam is shown in Fig. 5.2(e). The uncertainty on the beam waist and potential depth extracted from the transverse cross-sections for all the dipole trap beams is <1%, while the uncertainty on their position, determined by the center of the Gaussian fit, is of the order of a few hundred nm.

5.2.1 Non-linear phase shift in thick samples

While the linear model in Eq. 5.1 encapsulates the essence of the Ramsey imaging technique, there are corrections to this linear model owing to the distribution of atoms along the vertical direction for each pixel analyzed [130]. Atoms at different positions observe different amounts of light shifts, and hence the Ramsey phase measured for a given pixel is a weighted sum of the respective phases picked up along the vertical direction. This skewed distribution of atoms along the vertical direction has a two-pronged effect on the Ramsey signal: it leads to a reduction of contrast of the Ramsey fringe and to a non-linear shift in the Ramsey phase as a function of ellipticity. The total phase picked up by the atoms constitutes the linear contribution φ_{lin} (from Eq. 5.1) and the non-linear contribution φ_{in} due to the inhomogenous distribution along the vertical direction. To quantitatively account for the phase shift φ_{in}, we developed a model based on an assumption of a Gaussian distribution of atoms, parameterized by r_0 and σ, the offset from the imaged beam axis and the atom spread, respectively. The contribution to the Ramsey signal for such a distribution is

$$\langle e^{i\varphi(\vec{\rho},z,\epsilon)}\rangle = \int_{-\infty}^{\infty} e^{i\delta(\vec{\rho},z,\epsilon)t}\, p(z-z_0)\,\mathrm{d}z = C e^{i(\eta_s+\eta_v\epsilon)U_0(\vec{\rho})t/h} e^{i\varphi_{\mathrm{in}}}, \tag{5.5}$$

where $p(z)$ represents the probability distribution along the unresolved dimension, z_0 denotes an offset with respect to the optical axis of the imaged beam, C is the contrast of the Ramsey fringe, and $U_0(\vec{\rho})$ is the maximum trap depth at position $\vec{\rho}$. To compute the integral in Eq. (5.5), we assume that $p(z)$ is described by a Gaussian function of width σ, and that the potential $U(\vec{\rho}, z)$ is approximated by a harmonic potential of angular frequency ω. The expressions for the phase φ_{in} and contrast C can be extracted from

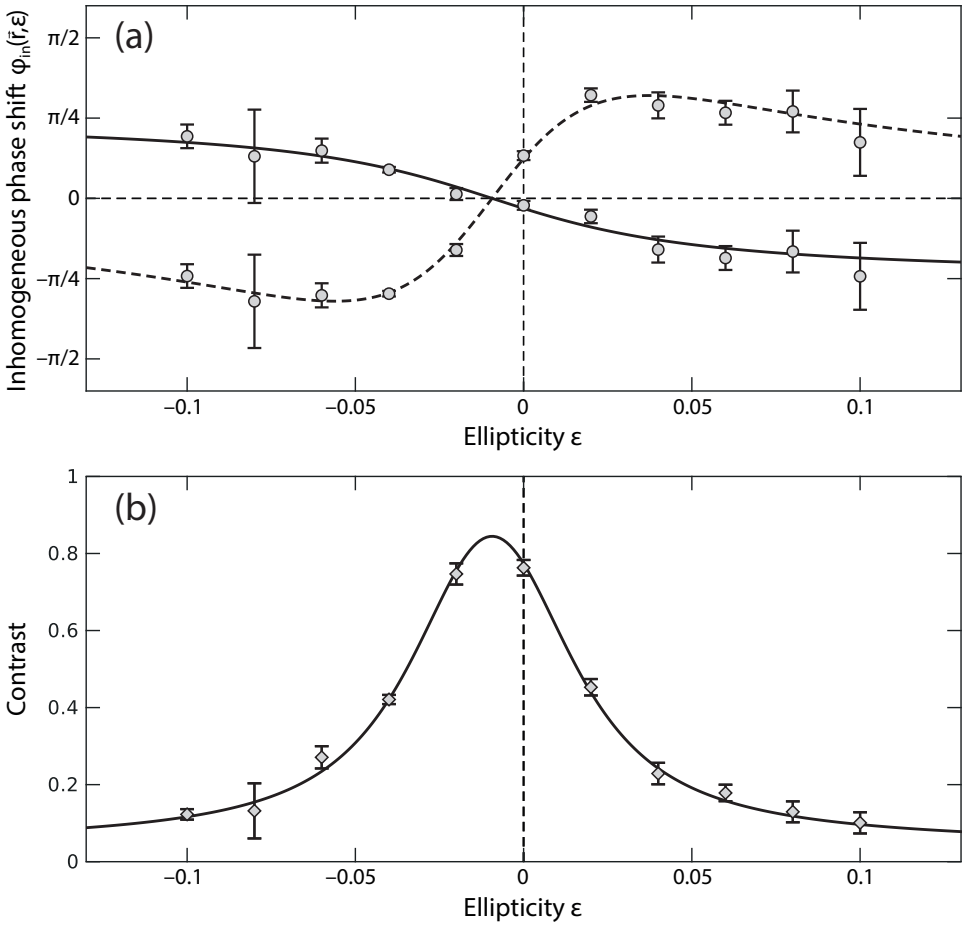

Figure 5.3: (a) Same data as in Fig. 5.1(f) showing the differential light shift as a function of the ellipticity, reproduced here for a close comparison to the two nonlinear terms in Eq. (5.6a). For each data set, the data are shown after subtracting all terms of the fitted model except for the one of interest, which is either the first (dashed line) or second term (solid line) in Eq. (5.6a). (b) The contrast for each of the Ramsey fringes analyzed in Fig. 5.1(e) is shown, the data is in good agreement with the model developed for a thick sample (see text), where the contrast modulates as a function of ellipticity ϵ (see Eq. (5.6b)).

Eq. (5.5),

$$\varphi_{\text{in}}(\epsilon) = \frac{\xi(\epsilon)}{1+\xi(\epsilon)^2}\left(\frac{z_0}{\sqrt{2}\sigma}\right)^2 - \arctan\left[\xi(\epsilon)\right], \tag{5.6a}$$

$$C(\epsilon) = \frac{C_0}{\left[1+\xi(\epsilon)^2\right]^{1/4}} \exp\left[-\frac{\xi(\epsilon)^2}{1+\xi(\epsilon)^2}\left(\frac{z_0}{\sqrt{2}\sigma}\right)^2\right], \tag{5.6b}$$

where $\xi(\epsilon) = (\eta_s + \eta_v\epsilon)\, m\omega^2\sigma^2/(\hbar/t)$ is a dimensionless quantity linearly proportional to the ellipticity ϵ. We fit this model simultaneously to both data sets (with an offset to the ellipticity), of phase and contrast for H-beam-3, as shown in Fig. 5.3, with the fits resulting in remarkable agreement with the model and generating the image shown in Fig 5.2(c). It must be noted that Fig. 5.3(a) shows the fits to the two non-linear terms in Eq. 5.6a, which have been obtained by subtracting the linear contribution

from Fig. 5.1(e). As is evident from Fig. 5.3(a), the non-linear behaviour of the phase shift manifests at larger ellipticities. The non-linear model improves our estimation of the trap depth, and in the case of imaging H-beam-3, the trap depth measured is 10% deeper than that measured using only the linear model. The atom spread we extract from the fit is between 10-15μm. We expect that these non-linear effects will vanish when imaging a single plane of atoms.

5.2.2 Imhomgeneous magnetic fields

A source of systematic uncertainty in the Ramsey imaging technique is any time invariant and spatially varying differential light shift, which can be caused by inhomogeneous magnetic fields, discussed in Section 4.4.1. Therefore, to improve the accuracy of this technique, it is beneficial to subtract such shifts. A gradient in magnetic field corresponds to a position dependent Zeeman shift. In order to measure this gradient we carry out the same Ramsey interferometric scheme but with the atoms in free fall, so that all measured frequency shifts can be attributed to magnetic field inhomogeneities. This gradient of frequency shifts is subtracted from all measurement we take for beam profiling.

5.2.3 Statistical precision

The Ramsey imaging technique relies on the accurate retrieval of the phase of a Ramsey fringe. We perform a fit to the data by minimizing the weighted mean squared error, thereby obtaining the most likely value for the phase of the Ramsey fringe. The uncertainty of the phase extracted from the fit $\delta\phi(\vec{r}, \epsilon)$ depends on the total number of atoms N and the contrast $C(\epsilon)$ of the Ramsey fringe[2]

$$\phi_{\mathrm{err}}(\vec{r}, \epsilon) = \frac{1}{[(1 - \sqrt{1 - C(\epsilon)^2})N]^{1/2}} \tag{5.7}$$

Here we assume the atom shot noise to be the dominant noise source. We extract the light shifts from the Ramsey fringe phases measured for ellipticities of the trapping beam in the range $\epsilon = \pm 0.1$, beyond which the contrast of the fringe falls below 10% (Fig. 5.3(b)). The light shift for ϵ outside the range of measurement is extrapolated from a linear fit to the measured data, with the corresponding error scaling as $\delta_{\mathrm{err}}(\vec{r}, \epsilon) = \sigma_0 \sqrt{3\epsilon^2/M}/\epsilon_M$, where M is the number of measurements, each with an error σ_0 and ϵ_M is the maximum ellipticity for which data has been acquired.

5.3 Conclusion

In conclusion, I have reported on a new technique for the precise in-vacuo imaging of laser beams by Ramsey interferometry. Using this technique, we reconstructed the optical potentials of all the four individual laser beams that constitute the 3D optical lattice. This simple yet precise beam-imaging method is a promising tool for experimental setups with a complex geometry of multiple laser beams, and with non-Gaussian beam shapes such as flat-top or hollow beams. This versatile technique is applicable for both near-resonant as well as far-detuned laser beams. We further improved the accuracy of this technique by modeling the non-linear phase shifts caused due to the thickness of the atomic sample probed. The Ramsey beam imaging technique promises to be an indispensable tool in complex cold atoms setups using alkali atoms, for precise alignment and characterization of the many lasers used in such experiments.

[2] A derivation for the uncertainty in the Ramsey phase is provided in Appendix C.

CHAPTER 6

Conclusion and outlook

In this thesis, I have presented our state-of-the-art setup of a two-dimensional state-dependent optical lattice. As part of a new generation of experiments in our group, we have tried to improve upon the older experiment that utilized a one-dimensional state-dependent lattice [107, 137, 149, 180]. With transport capabilities in two dimensions, we open up possibilities to a plethora of new and exciting experiments, albeit at the cost of technical complexity. In chapter 2, I described the primary components of our setup, with emphasis on the modifications made in recent years. We were able to improve the loading of atoms into our optical lattice from around 40 to roughly 2000 by optimizing the optics for the MOT. This increase in atom number was possible with the installation of a high power laser system [181]. Further, we designed and installed low-noise amplified photo diodes to suppress laser intensity noise of the optical lattice beams down to the shot noise [125].

Chapter 3 presents the results of the first trials of state dependent transport in two dimensions, paving the way for future experiments that will use this novel technique. Groh et al. [68] propose to use our setup to create spatial boundaries between distinct topological phases in order to study uni-directionless, dissipationless transport of topologically protected states using spin dependent discrete shift operations. The spin dependent optical lattice will also be used in the direct measurement of the exchange phase, as proposed by Roos et al. [182]. Lastly, Sajid et al. [69] propose to use discrete-time quantum walks in a two-dimensional lattice to construct anomalous Floquet Chern topological insulators. All these proposed experiments make use of quantum walks, the quantum analogue of the classical random walk. The number of steps taken in such a walk is finally limited by the coherence time of the atoms in the optical lattice. Hence, as a step towards prolonging the coherence of our system, we cool all atoms to the ground state, as discussed in section 3.4.

Continuing the emphasis on coherence times, in chapter 4 I present some techniques used to investigate the different dephasing contributions in our experiment, using Ramsey spectroscopy as the primary tool. To this end, we find that we can achieve coherence on the order of a few milliseconds, which means we can perform hundreds of steps of a quantum walk before dephasing kicks in. Our experiment has been setup as a two dimensional discrete quantum simulator (2D DQSIM). Quantum simulations rely on the advantage of a clean and controllable system provided by optical lattices. In order to ensure that our optical lattice beams are indeed defect free and precisely positioned, we developed a technique for in-situ Ramsey imaging of optical dipole traps, as explained in chapter 5. This technique enables us to reconstruct the dipole potential with micrometer spatial resolution, allowing for very precise alignment of the dipole beams. The Ramsey imaging technique promises to be a very valuable tool for experiments that employ dipole beams in complex geometries. In addition, we also shed light on some systematic uncertainties in obtaining the trap depth, particularly the inhomogeneous contribution due to the thickness

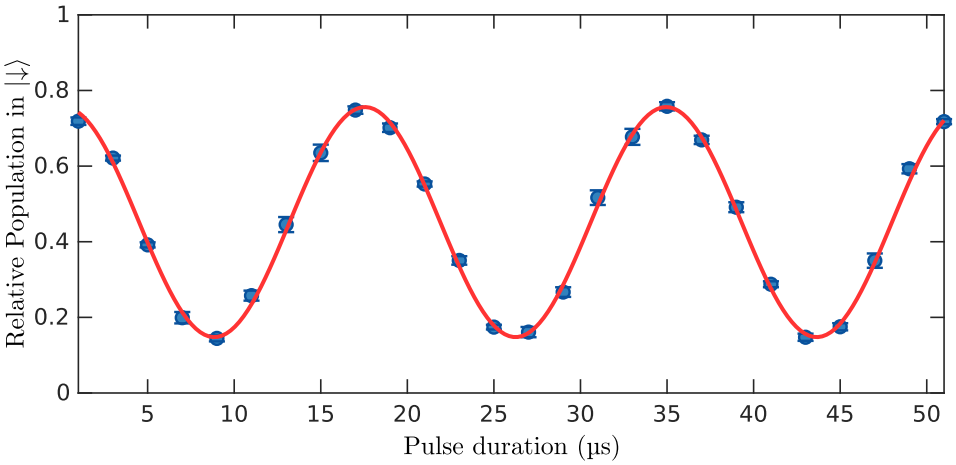

Figure 6.1: Rabi oscillations on the π qubit ($|F = 3, m_F = 3\rangle \leftrightarrow |F = 4, m_F = 3\rangle$) with an oscillation frequency of 57 kHz, extracted from the fit (solid red line). The amplitude of this oscillation is not 1 due to imperfections in the initial preparation of atoms in $|F = 3, m_F = 3\rangle$, and background losses.

of the atomic ensemble probed.

The DQSIM experiment has only just begun to reap the rewards of the development, mostly technical, of the past years. The future of the experiment is very promising, particularly given the high interest in quantum information processing and simulation, both fields that benefit from quantum walks [18, 75, 183]. Here I will present some proposed plans for this experiment.

6.1 Moving to the π qubit

Currently we work with a qubit that correspond to states $|\uparrow\rangle \rightarrow |F = 4, m_F = 4\rangle$ and $|\downarrow\rangle \rightarrow |F = 3, m_F = 3\rangle$. We have chosen a 'magic wavelength' for our optical lattice in order to independently control the position of the two states with σ^+ and σ^- polarized light. However, while $|\uparrow\rangle$ is only sensitive to σ^+ polarized light, $|\downarrow\rangle$ is not purely dependent on σ^- light, it sees a non-zero contribution from σ^+ light as well, as is clear from the expression for the two potentials $U_\uparrow$ and $U_\downarrow$,

$$\begin{pmatrix} U_\uparrow \\ U_\downarrow \end{pmatrix} = -k_0 \begin{pmatrix} 1 & 0 \\ 1/8 & 7/8 \end{pmatrix} \begin{pmatrix} I_{\sigma^+} \\ I_{\sigma^-} \end{pmatrix} \tag{6.1}$$

where k_0 is a proportionality constant that depends on the caesium polarizability. This cross-term poses a challenge during transport because it leads to an undesirable modulation of the trap depth for $|\downarrow\rangle$ while transporting $|\uparrow\rangle$. This differential potential wobbling leads to inhomogeneous dephasing [95], because of the differential light shifts observed by the two states. Furthermore, because of the wobbling, motional excitations for the two spin components differ during transport, both in phase and amplitude, leading to a reduction in overlap between the two wave functions.

To circumvent these issues, we can cool atoms to the 3D ground state, use intensity feed-forward techniques to compensate for the wobbling and use optimal control to design transport ramps where the motional excitations are kept in check [184]. An alternate approach we plan to follow is to change the qubit states to $|\uparrow\rangle \rightarrow |F = 4, m_F = 3\rangle$ and $|\downarrow\rangle \rightarrow |F = 3, m_F = 3\rangle$, which we call the π qubit. With this configuration, we can choose a new 'magic wavelength' at 869 nm such that there is no cross-talk,

and hence no wobbling during transport, ruling out the need for sophisticated compensation techniques. To work on the π qubit, we apply a π pulse after optically pumping atoms to $|F = 4, m_F = 4\rangle$ to bring them to $|F = 3, m_F = 3\rangle$. Thereafter, we tune the microwave to the $|F = 4, m_F = 4\rangle \leftrightarrow |F = 3, m_F = 3\rangle$ transition, which is $\approx$1.3 MHz red detuned to the $|F = 4, m_F = 4\rangle \leftrightarrow |F = 3, m_F = 3\rangle$ transition for our applied magnetic bias field. Figure 6.1 shows preliminary Rabi oscillations we performed on the π qubit.

6.2 Plane selection and single site addressing

In chapter 4 and 5, we have discussed the effect of inhomogeneous dephasing due to the the distribution of atoms in the vertical direction, which can be avoided by working with a single vertical plane of atoms. Furthermore, since we are interested in performing simulations on the two-dimensional plane, we plan to select a single vertical plane from the ensemble of atoms. Each plane is separated by 532 nm, half the wavelength of the vertical lattice. We have developed an all optical scheme [109] for plane selection, using a polarization gradient to create position dependent light shifts, as opposed to magnetic field gradients [103, 185, 186] where the Zeeman effect is used. The procedure begins with compressing the ensemble of atoms vertically [125] followed by turning on the optical polarization gradient beam to induce light shifts. Finally a standard microwave spectroscopy sequence will be performed, with the microwave frequency resonant with the atoms that are occupying the plane of our choice, and all other atoms being heated out of the lattice.

The 'correct' vertical plane to work with is ideally in the center of the optical lattice where the trap is most homogeneous, and in the focal plane of the objective lens. The depth of focus of our objective lens is ±250 nm [59]. In order to ensure that the chosen plane of atoms is in the focal plane we plan to perform spatial tomography of atoms trapped in a 3D lattice [187](in collaboration with Jacob Sherson's group). By manipulating the phase front of the point spread function of the atoms imaged, we will be able to localize atoms in different planes from a single shot fluorescence image [188] .The phase manipulation will be performed by a spatial light modulator[1] (SLM) in the imaging path.

In addition to imprinting phase masks, the SLM will be used in conjunction with the high NA objective to address individual atoms. Although this thesis describes measurements where all microwave/optical operations are common to all atoms trapped in the lattice, individual addressing of atoms will bring the experiment to the next level of control. Individual addressing will be achieved by impinging the target atoms with a laser beam focused through the high NA objective lens, resulting in an ac Stark shift of the target atoms [45, 47, 105, 106, 189, 190]. Microwave radiation tuned to the shifted resonance condition can then be used to manipulate the quantum states of these target atoms. Since the objective has an optical resolution of 460 nm, we don't expect the addressing beams to affect atoms neighboring the target atom. Individual addressing can be used for sorting atoms into arbitrary patterns [46, 58, 191], to implement a bottom up approach for preparing low-entropy states [58, 192] and for further applications in quantum chemistry [193], quantum simulation [16, 194, 195] and quantum information processing [196–198]. Robens et al. [44] have proposed a polarization synthesized optical-lattice atom-sorting (PSOLAS) algorithm to accomplish unity filling in a sqaure target of size 31×31 lattice sites, using atoms from an area of size 100×100 lattice sites (see Fig. 6.2). The algorithm works by identifying a pattern of atoms that best fits the empty lattice sites of the target square. Only these atoms are then addressed using a light pattern generated by the SLM in order to transfer them to a state different from the rest. They are them transported to the the target location using the state dependent lattices. Robens et al. show that for very conservative experimental parameters (achievable for the DQSIM experiment), it would take 12 iterations of the PSOLAS algorithm to achieve unity filling.

[1] LCoS SLM-100: Santec Corporation

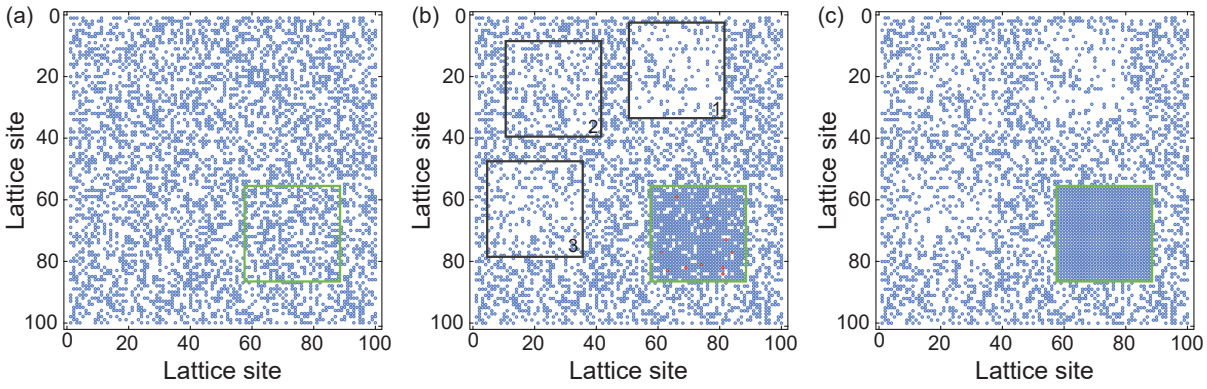

Figure 6.2: Conceptual illustration of PSOLAS, with the goal of creating unity filling in a target pattern of size 31×31 lattice sites (green square region). (a) The initial distribution of atoms in the 2D lattice, assuming a (conservative) 40% filling probability. (b) The distribution of atoms after 3 PSOLAS iterations. The black squares represent the regions where the atom patterns best matched the empty sites in the target square. The red pixels in the target square indicate lattice sites with double occupancy, which are caused from addressing crosstalk (assumed to be 10%) at the third iteration of PSOLAS. This simulation assumes perfect parity projection caused by light assisted collisions, which means the both atoms will be expelled out during imaging and these lattice sites will be empty for the next iteration of PSOLAS. (c) Final atom distribution, with unity filling achieved for the target square after 12 PSOLAS iterations. Figure taken from [58].

6.3 Two dimensional quantum walks and applications

Our experimental setup fulfills all the requirements to perform a discrete time quantum walk (DTQW) with a single atom. We use the microwaves to perform the coin operation and the state-dependent lattice enables the shift operation. A quantum walk in two dimensions is defined as

$$W_{2D} = S_y^{\uparrow} S_y^{\downarrow} C(\theta_2) S_x^{\uparrow} S_x^{\downarrow} C(\theta_1) \tag{6.2}$$

where $C(\theta)$ is the coin operator, rotating the spin state by angle θ. $S_{x,y}^{\uparrow,\downarrow}$ is the shift operator where the superscript corresponds to the spin state being shifted and the subscript corresponds to the direction of the shift. Already demonstrated for a one dimensional system [60], quantum walks in two dimensions will open up the possibilities to study the rich field of topological insulators [63, 68, 69, 199, 200].

Groh et al. [68] propose to demonstrate the robustness of topologically protected edge states with quantum walks. The idea is to create two distinct topological domains, each with a corresponding topological invariant, in our case the Rudner winding number [200]. At the boundary between these two regions lie topologically protected edge modes, as expected from the bulk-boundary correspondence principle [201]. Such topological regions and boundaries are created by implementing a position dependent coin angle for the coin operation of the DTQW. The positions dependent coin operation is performed by Raman lasers (as opposed to microwaves, which will be used for global coin operations) where the coin angle depends on the intensity of the beam. This spatially varying intensity pattern is created by the SLM and imaged onto the optical lattice through the high NA objective lens such that we can create very sharp boundaries, localized to a single lattice site. We then expect a quantum walker, populating the edge state, to perform a uni-directional and dissipationless propagation along boundary between the topological domains. Once we have demonstrated such a topologically protected state, we intend to go a step further by introducing controlled interactions to shed light upon the still nascent field

of topological phases with interacting particles [202–205].

Sajid et al. [69] also propose an experiment to demonstrate topological insulators, in this case anomalous Floquet Chern insulators, with DTQWs in the presence of an artificial magnetic field gradient. The protocol of the magnetic quantum walk is

$$W_M = FS_yCS_xC \tag{6.3}$$

where S and C are the shift and coin operators introduced above and F is the magnetic field operator. The magnetic field operator F is realized by flashing a light field for a fixed duration on the atoms, such that the differential light shift plays the role of the Zeeman shift induced by magnetic fields. In this scenario of an inhomogeneous 'magnetic-field' gradient, the topological domains are characterized by different magnetic fluxes, and at their boundaries we expect topologically protected edge states, which will be demonstrated by the uni-directional propagation of the walker.

Further planned experiments include the direct measurement of the exchange phase in a two particle interferometer, proposed by Roos et al. [182]. When the position of two identical particles is swapped, their quantum mechanical state remains the same except for an exchange phase, which is 0 for bosons and π for fermions. In the proposed experiment, the phase of the interference fringe reveals whether the exchanged particles are bosons or fermions. The experiment is designed such that the two particles never meet when their positions are swapped, such that the phase of the interference fringe can be attributed solely to the exchange operation. In line with this fundamental investigation, another experiment we envisage is to perform boson sampling [206] with neutral atoms. Boson sampling is a strong candidate to demonstrate the advantage of quantum computers over their classical counterparts, and has recently been demonstrated with photons with a quantum computational advantage of around 10^{14} [207]. Our state dependent lattice offer an ideal platform to demonstrate such quantum computational advantage using neutral atoms, since we can scale up the number of bosons used to around 100. As we move toward working with a larger number of atoms, future experiments will involve controlled interactions [172], for instance for the creation of cluster states [208–210]. As we can see, our two-dimensional discrete quantum simulator has a long pipeline of really exciting experiments lined up; the fun has just begun!

Bibliography

[1] G. Ramola, R. Winkelmann, K. Chandrashekara, W. Alt, P. Xu, D. Meschede and A. Alberti, "Ramsey Imaging of Optical Traps", Physical Review Applied 16.2 (2021) 024041, ISSN: 2331-7019 (cit. on p. iii).

[2] J. P. Dowling and G. J. Milburn, "Quantum technology: the second quantum revolution", Philosophical Transactions of the Royal Society of London. Series A: Mathematical, Physical and Engineering Sciences 361.1809 (2003) 1655, ed. by A. G. J. MacFarlane, ISSN: 1364-503X, arXiv: 0206091 [quant-ph] (cit. on p. 1).

[3] W. P. Schleich, K. S. Ranade, C. Anton, M. Arndt, M. Aspelmeyer, M. Bayer, G. Berg, T. Calarco, H. Fuchs, E. Giacobino, M. Grassl, P. Hänggi, W. M. Heckl, I. V. Hertel, S. Huelga, F. Jelezko, B. Keimer, J. P. Kotthaus, G. Leuchs, N. Lütkenhaus, U. Maurer, T. Pfau, M. B. Plenio, E. M. Rasel, O. Renn, C. Silberhorn, J. Schiedmayer, D. Schmitt-Landsiedel, K. Schönhammer, A. Ustinov, P. Walther, H. Weinfurter, E. Welzl, R. Wiesendanger, S. Wolf, A. Zeilinger and P. Zoller, "Quantum technology: from research to application", Applied Physics B: Lasers and Optics 122.5 (2016), ISSN: 09462171 (cit. on p. 1).

[4] M. Atzori and R. Sessoli, "The Second Quantum Revolution: Role and Challenges of Molecular Chemistry", Journal of the American Chemical Society 141.29 (2019) 11339, ISSN: 15205126 (cit. on p. 1).

[5] K. Bongs, M. Holynski, J. Vovrosh, P. Bouyer, G. Condon, E. Rasel, C. Schubert, W. P. Schleich and A. Roura, "Taking atom interferometric quantum sensors from the laboratory to real-world applications", Nature Reviews Physics 1.12 (2019) 731, ISSN: 25225820 (cit. on p. 1).

[6] L. Pezzè, A. Smerzi, M. K. Oberthaler, R. Schmied and P. Treutlein, "Quantum metrology with nonclassical states of atomic ensembles", Reviews of Modern Physics 90.3 (2018), ISSN: 15390756, arXiv: 1609.01609 (cit. on p. 1).

[7] G. Tóth and I. Apellaniz, "Quantum metrology from a quantum information science perspective", Journal of Physics A: Mathematical and Theoretical 47.42 (2014), ISSN: 17518121, arXiv: 1405.4878 (cit. on p. 1).

[8] E. Polino, M. Valeri, N. Spagnolo and F. Sciarrino, "Photonic quantum metrology", arXiv 024703.May (2020), ISSN: 23318422, arXiv: 2003.05821 (cit. on p. 1).

[9] N. M. Linke, D. Maslov, M. Roetteler, S. Debnath, C. Figgatt, K. A. Landsman, K. Wright and C. Monroe, "Experimental comparison of two quantum computing architectures", Proceedings of the National Academy of Sciences of the United States of America 114.13 (2017) 3305, ISSN: 10916490, arXiv: 1702.01852 (cit. on p. 1).

[10] L. Gyongyosi and S. Imre, "A Survey on quantum computing technology", Computer Science Review 31 (2019) 51, ISSN: 15740137 (cit. on p. 1).

[11] E. Knill, "Quantum computing with realistically noisy devices", Nature 434.7029 (2005) 39, ISSN: 00280836 (cit. on p. 1).

[12] A. Negretti, P. Treutlein and T. Calarco, "Quantum computing implementations with neutral particles", Quantum Information Processing 10.6 (2011) 721, ISSN: 15700755 (cit. on pp. 1, 35).

[13] J. R. Weber, W. F. Koehl, J. B. Varley, A. Janotti, B. B. Buckley, C. G. Van De Walle and D. D. Awschalom, "Quantum computing with defects", Proceedings of the National Academy of Sciences of the United States of America 107.19 (2010) 8513, ISSN: 00278424 (cit. on p. 1).

[14] R. Blatt and C. F. Roos, "Quantum simulations with trapped ions", Nature Physics 8.4 (2012) 277, ISSN: 1745-2473, arXiv: 0905.0118 (cit. on pp. 1, 15).

[15] I. Bloch, J. Dalibard and S. Nascimbène, "Quantum simulations with ultracold quantum gases", Nature Physics 8.4 (2012) 267, ISSN: 1745-2473 (cit. on pp. 1, 15, 59).

[16] M. Lewenstein, A. Sanpera, V. Ahufinger, B. Damski, A. Sen and U. Sen, "Ultracold atomic gases in optical lattices: Mimicking condensed matter physics and beyond", Advances in Physics 56.2 (2007) 243, ISSN: 00018732, arXiv: 0606771 [cond-mat] (cit. on pp. 1, 71).

[17] B. Villalonga, D. Lyakh, S. Boixo, H. Neven, T. S. Humble, R. Biswas, E. G. Rieffel, A. Ho and S. Mandrà, "Establishing the quantum supremacy frontier with a 281 Pflop/s simulation", Quantum Science and Technology 5.3 (2020) 034003, ISSN: 2058-9565 (cit. on p. 1).

[18] S. Lloyd, "Universal quantum simulators", Science 273.5278 (1996) 1073, ISSN: 00368075 (cit. on pp. 1, 70).

[19] I. M. Georgescu, S. Ashhab and F. Nori, "Quantum simulation", Reviews of Modern Physics 86.1 (2014) 153, ISSN: 15390756, arXiv: 1308.6253 (cit. on p. 1).

[20] J. I. Cirac and P. Zoller, "Goals and opportunities in quantum simulation", Nature Physics 8.4 (2012) 264, ISSN: 17452473 (cit. on p. 1).

[21] W. Hofstetter and T. Qin, "Quantum simulation of strongly correlated condensed matter systems", Journal of Physics B: Atomic, Molecular and Optical Physics 51.8 (2018), ISSN: 13616455 (cit. on p. 1).

[22] I. Bloch, J. Dalibard and S. Nascimbène, "Quantum simulations with ultracold quantum gases", Nature Physics 8.4 (2012) 267, ISSN: 17452473 (cit. on p. 1).

[23] I. Buluta and F. Nori, *Quantum simulators*, 2009 (cit. on p. 1).

[24] C. Gross and I. Bloch, "Quantum simulations with ultracold atoms in optical lattices", Science 357.6355 (2017) 995, ISSN: 10959203 (cit. on pp. 1, 59).

[25] P. J. Lee, M. Anderlini, B. L. Brown, J. Sebby-Strabley, W. D. Phillips and J. V. Porto, "Sublattice addressing and spin-dependent motion of atoms in a double-well lattice", Physical Review Letters 99.2 (2007) 1, ISSN: 00319007 (cit. on p. 1).

[26] P. Schauss, "Quantum simulation of transverse Ising models with Rydberg atoms", Quantum Science and Technology 3.2 (2018), ISSN: 20589565 (cit. on p. 1).

[27] A. Browaeys and T. Lahaye, "Many-body physics with individually controlled Rydberg atoms", Nature Physics 16.2 (2020) 132, ISSN: 17452481, arXiv: 2002.07413 (cit. on p. 1).

[28] D. Jaksch, C. Bruder, J. Cirac, C. Gardiner and P. Zoller,
"Cold Bosonic Atoms in Optical Lattices", Physical Review Letters 81.15 (1998) 3108,
ISSN: 0031-9007 (cit. on p. 1).

[29] H. Bernien, S. Schwartz, A. Keesling, H. Levine, A. Omran, H. Pichler, S. Choi, A. S. Zibrov,
M. Endres, M. Greiner, V. Vuletic and M. D. Lukin,
"Probing many-body dynamics on a 51-atom quantum simulator", Nature 551.7682 (2017) 579,
ISSN: 14764687, arXiv: 1707.04344 (cit. on p. 1).

[30] K. Wintersperger, C. Braun, F. N. Ünal, A. Eckardt, M. D. Liberto, N. Goldman, I. Bloch and
M. Aidelsburger,
"Realization of an anomalous Floquet topological system with ultracold atoms",
Nature Physics 16.10 (2020) 1058, ISSN: 17452481, arXiv: 2002.09840 (cit. on p. 1).

[31] S. Wilkinson, C. Bharucha, K. Madison, Q. Niu and M. Raizen,
"Observation of Atomic Wannier-Stark Ladders in an Accelerating Optical Potential",
Physical Review Letters 76 (1996) 4512, ISSN: 0031-9007 (cit. on p. 1).

[32] C. C. Chien, S. Peotta and M. Di Ventra, *Quantum transport in ultracold atoms*, 2015,
arXiv: 1504.02907 (cit. on p. 1).

[33] D. Greif, T. Uehlinger, G. Jotzu, L. Tarruell and T. Esslinger,
"Short-range quantum magnetism of ultracold fermions in an optical lattice",
Science 340.6138 (2013) 1307, ISSN: 10959203, arXiv: 1212.2634 (cit. on p. 1).

[34] A. J. Daley, M. M. Boyd, J. Ye and P. Zoller,
"Quantum computing with alkaline-earth-metal atoms",
Physical Review Letters 101.17 (2008) 1, ISSN: 00319007 (cit. on p. 1).

[35] L. Henriet, L. Beguin, A. Signoles, T. Lahaye, A. Browaeys, G. O. Reymond and C. Jurczak,
"Quantum computing with neutral atoms", Quantum 4 (2020) 1, ISSN: 2521327X,
arXiv: 2006.12326 (cit. on p. 1).

[36] Y. Cao, J. Romero and A. Aspuru-Guzik, "Potential of quantum computing for drug discovery",
IBM Journal of Research and Development 62.6 (2018) 1, ISSN: 21518556 (cit. on p. 1).

[37] A. K. Fedorov and M. S. Gelfand,
"Towards practical applications in quantum computational biology",
Nature Computational Science 1.2 (2021) 114, ISSN: 2662-8457 (cit. on p. 1).

[38] D. Solenov, J. Brieler and J. F. Scherrer, "The Potential of Quantum Computing and Machine
Learning to Advance Clinical Research and Change the Practice of Medicine.",
Missouri medicine 115.5 (2018) 463, ISSN: 0026-6620 (cit. on p. 1).

[39] C. Monroe, "Quantum information processing with atoms and photons",
Nature 416.6877 (2002) 238, ISSN: 0028-0836 (cit. on p. 1).

[40] F. Gaitan, "Finding flows of a Navier–Stokes fluid through quantum computing",
npj Quantum Information 6.1 (2020), ISSN: 20566387 (cit. on p. 1).

[41] J. Preskill, "Quantum computing in the NISQ era and beyond", Quantum 2.July (2018) 1,
ISSN: 2521327X, arXiv: 1801.00862 (cit. on p. 1).

[42] J. I. Cirac, "Quantum computing and simulation", Nanophotonics 10.1 (2020) 453,
ISSN: 2192-8606 (cit. on p. 1).

[43] D. Jaksch, J. I. Cirac, P. Zoller, S. L. Rolston, R. Côté and M. D. Lukin, "Fast Quantum Gates for Neutral Atoms", Physical Review Letters 85.10 (2000) 2208, ISSN: 0031-9007 (cit. on p. 1).

[44] C. Robens, J. Zopes, W. Alt, S. Brakhane, D. Meschede and A. Alberti, "Low-Entropy States of Neutral Atoms in Polarization-Synthesized Optical Lattices", Physical Review Letters 118.6 (2017) 1, ISSN: 10797114, arXiv: 1608.02410 (cit. on pp. 1, 71).

[45] Y. Wang, X. Zhang, T. A. Corcovilos, A. Kumar and D. S. Weiss, "Coherent Addressing of Individual Neutral Atoms in a 3D Optical Lattice", Physical Review Letters 115.4 (2015) 1, ISSN: 10797114, arXiv: 1504.02117 (cit. on pp. 1, 71).

[46] A. Kumar, T.-Y. Wu, F. Giraldo and D. S. Weiss, "Sorting ultracold atoms in a three-dimensional optical lattice in a realization of Maxwell's demon", Nature (2018), ISSN: 0028-0836 (cit. on pp. 1, 71).

[47] J. H. Lee, E. Montano, I. H. Deutsch and P. S. Jessen, "Robust site-resolvable quantum gates in an optical lattice via inhomogeneous control", Nature Communications 4.May (2013) 1, ISSN: 20411723 (cit. on pp. 1, 71).

[48] W. S. Bakr, J. I. Gillen, A. Peng, S. Fölling and M. Greiner, "A quantum gas microscope for detecting single atoms in a Hubbard-regime optical lattice", Nature (2009), ISSN: 00280836, arXiv: 0908.0174 (cit. on pp. 2, 12, 26).

[49] J. F. Sherson, C. Weitenberg, M. Endres, M. Cheneau, I. Bloch and S. Kuhr, "Single-atom-resolved fluorescence imaging of an atomic Mott insulator", Nature (2010), ISSN: 00280836, arXiv: 1006.3799 (cit. on pp. 2, 12).

[50] M. Martinez-Dorantes, W. Alt, J. Gallego, S. Ghosh, L. Ratschbacher, Y. Völzke and D. Meschede, "Fast Nondestructive Parallel Readout of Neutral Atom Registers in Optical Potentials", Physical Review Letters 119.18 (2017) 1, ISSN: 10797114, arXiv: 1706.00264 (cit. on p. 2).

[51] A. Alberti, C. Robens, W. Alt, S. Brakhane, M. Karski, R. Reimann, A. Widera and D. Meschede, "Super-resolution microscopy of single atoms in optical lattices", New Journal of Physics 18.5 (2016), ISSN: 13672630, arXiv: 1512.07329 (cit. on pp. 2, 13, 96).

[52] D. S. Weiss and M. Saffman, *Quantum computing with neutral atoms*, 2017 (cit. on p. 2).

[53] H. Levine, A. Keesling, G. Semeghini, A. Omran, T. T. Wang, S. Ebadi, H. Bernien, M. Greiner, V. Vuletić, H. Pichler and M. D. Lukin, "Parallel Implementation of High-Fidelity Multiqubit Gates with Neutral Atoms", Physical Review Letters 123.17 (2019) 1, ISSN: 10797114, arXiv: 1908.06101 (cit. on p. 2).

[54] L. Förster, M. Karski, J. M. Choi, A. Steffen, W. Alt, D. Meschede, A. Widera, E. Montano, J. H. Lee, W. Rakreungdet and P. S. Jessen, "Microwave control of atomic motion in optical lattices", Physical Review Letters 103.23 (2009) 1, ISSN: 00319007, arXiv: 0909.0678 (cit. on p. 2).

[55] M. Karski, F. Leonid, A. Andrea, A. Wolfgang, W. Artur and M. Dieter, "Direct Observation and Analysis of Spin Dependent Transport of Single Atoms in a 1D Optical Lattice", Journal of the Korean Physical Society 59.41 (2011) 2947, ISSN: 0374-4884 (cit. on p. 2).

[56] O. Mandel, M. Greiner, A. Widera, T. Rom, T. W. Hänsch and I. Bloch,
"Coherent transport of neutral atoms in spin-dependent optical lattice potentials.",
Physical review letters 91.1 (2003) 010407, ISSN: 0031-9007, arXiv: 0301169 [cond-mat]
(cit. on pp. 2, 15).

[57] D. Jaksch, H. .-J. Briegel, J. I. Cirac, C. W. Gardiner and P. Zoller,
"Entanglement of atoms via cold controlled collisions",
Physical Review Letters 82.9 (1999) 1975, ISSN: 10797114, arXiv: 9810087 [quant-ph]
(cit. on pp. 2, 15).

[58] C. Robens, J. Zopes, W. Alt, S. Brakhane, D. Meschede and A. Alberti,
"Low-Entropy States of Neutral Atoms in Polarization-Synthesized Optical Lattices",
Physical Review Letters 118.6 (2017) 1, ISSN: 10797114, arXiv: 1608.02410
(cit. on pp. 2, 24, 63, 71, 72).

[59] C. Robens, S. Brakhane, W. Alt, F. Kleißler, D. Meschede, G. Moon, G. Ramola and A. Alberti,
"High numerical aperture (NA = 0.92) objective lens for imaging and addressing of cold atoms",
Optics Letters 42.6 (2017), ISSN: 15394794 (cit. on pp. 2, 13, 71).

[60] M. Karski, L. Forster, J.-M. Choi, A. Steffen, W. Alt, D. Meschede and A. Widera,
"Quantum Walk in Position Space with Single Optically Trapped Atoms",
Science 325.5937 (2009) 174, ISSN: 0036-8075 (cit. on pp. 2, 15, 72).

[61] W. Dür, R. Raussendorf, V. M. Kendon and H. J. Briegel, "Quantum walks in optical lattices",
Physical Review A - Atomic, Molecular, and Optical Physics 66.5 (2002) 8, ISSN: 10941622
(cit. on p. 2).

[62] Y. Aharonov, L. Davidovich and N. Zagury, "Quantum random walks",
Physical Review A 48.2 (1993) 1687, ISSN: 10502947 (cit. on p. 2).

[63] T. Kitagawa, M. S. Rudner, E. Berg and E. Demler,
"Exploring topological phases with quantum walks",
Physical Review A - Atomic, Molecular, and Optical Physics 82.3 (2010), ISSN: 10502947,
arXiv: 1003.1729 (cit. on pp. 2, 72).

[64] M. Gong, S. Wang, C. Zha, M.-C. Chen, H.-l. Huang, Y. Wu, Q. Zhu, Y. Zhao, S. Li, S. Guo,
H. Qian, Y. Ye, F. Chen, C. Ying, J. Yu, D. Fan, D. Wu, H. Su, H. Deng, H. Rong, K. Zhang,
S. Cao, J. Lin, Y. Xu, L. Sun, C. Guo, N. Li, F. Liang, V. M. Bastidas, K. Nemoto, W. J. Munro,
Y.-h. Huo, C.-y. Lu, C.-z. Peng, X. Zhu and J.-w. Pan,
"Quantum walks on a programmable two-dimensional 62-qubit superconducting processor",
(2021), arXiv: 2102.02573 (cit. on p. 2).

[65] S. E. Venegas-Andraca, "Quantum walks: A comprehensive review",
Quantum Information Processing 11.5 (2012) 1015, ISSN: 15700755, arXiv: 1201.4780
(cit. on p. 2).

[66] A. Alberti and S. Wimberger,
"Quantum walk of a Bose-Einstein condensate in the Brillouin zone",
Physical Review A 96.2 (2017) 1, ISSN: 24699934, arXiv: 1705.00512 (cit. on p. 2).

[67] S. Panahiyan and S. Fritzsche, "Toward simulation of topological phenomena with one-, two-,
and three-dimensional quantum walks", Physical Review A 103.1 (2021), ISSN: 24699934,
arXiv: 2005.08720 (cit. on p. 2).

[68] T. Groh, S. Brakhane, W. Alt, D. Meschede, J. K. Asbóth and A. Alberti, "Robustness of topologically protected edge states in quantum walk experiments with neutral atoms", Physical Review A 94.1 (2016) 1, ISSN: 24699934, arXiv: 1605.03633 (cit. on pp. 2, 35, 62, 69, 72).

[69] M. Sajid, J. K. Asbóth, D. Meschede, R. F. Werner and A. Alberti, "Creating anomalous Floquet Chern insulators with magnetic quantum walks", Physical Review B 99.21 (2019) 1, ISSN: 24699969, arXiv: 1808.08923 (cit. on pp. 2, 35, 69, 72, 73).

[70] N. Shenvi, J. Kempe and K. B. Whaley, "Quantum random-walk search algorithm", Physical Review A - Atomic, Molecular, and Optical Physics 67.5 (2003) 523071, ISSN: 10502947, arXiv: 0210064 [quant-ph] (cit. on p. 2).

[71] A. M. Childs and J. Goldstone, "Spatial search by quantum walk", Physical Review A - Atomic, Molecular, and Optical Physics 70.2 (2004) 1, ISSN: 10502947, arXiv: 0306054 [quant-ph] (cit. on p. 2).

[72] M. Hillery, D. Reitzner and V. Bužek, "Searching via walking: How to find a marked clique of a complete graph using quantum walks", Physical Review A - Atomic, Molecular, and Optical Physics 81.6 (2010) 1, ISSN: 10502947 (cit. on p. 2).

[73] D. Reitzner, D. Nagaj and V. Bužek, "Quantum Walks", Acta Physica Slovaca. Reviews and Tutorials 61.6 (2011) 309, ISSN: 1336-040X, arXiv: arXiv:1207.7283v2 (cit. on p. 2).

[74] A. M. Childs, "Universal computation by quantum walk", Physical Review Letters 102.18 (2009) 1, ISSN: 00319007, arXiv: 0806.1972 (cit. on p. 2).

[75] A. M. Childs, D. Gosset and Z. Webb, "Universal computation by multiparticle quantum walk", Science 339.6121 (2013) 791, ISSN: 10959203, arXiv: 1205.3782 (cit. on pp. 2, 70).

[76] N. B. Lovett, S. Cooper, M. Everitt, M. Trevers and V. Kendon, "Universal quantum computation using the discrete-time quantum walk", Physical Review A - Atomic, Molecular, and Optical Physics 81.4 (2010), ISSN: 10502947, arXiv: 0910.1024 (cit. on p. 2).

[77] M. A. Broome, A. Fedrizzi, S. Rahimi-Keshari, J. Dove, S. Aaronson, T. C. Ralph and A. G. White, "Photonic boson sampling in a tunable circuit", Science 339.6121 (2013) 794, ISSN: 10959203, arXiv: 1212.2234 (cit. on p. 2).

[78] S. Brakhane, "The Quantum Walk Microscope", PhD thesis: University of Bonn, 2016 (cit. on pp. 3, 5, 6, 8, 11, 12, 19, 48).

[79] B. S. Mathur, H. Tang and W. Happer, "Light shifts in the alkali atoms", Physical Review 171.1 (1968) 11, ISSN: 0031899X (cit. on pp. 3, 40).

[80] A. A. Wood, L. D. Turner and R. P. Anderson, "Measurement and extinction of vector light shifts using interferometry of spinor condensates", Physical Review A (2016), ISSN: 24699934, arXiv: 1607.06898 (cit. on p. 3).

[81] K. Zhu, N. Solmeyer, C. Tang and D. S. Weiss, "Absolute polarization measurement using a vector light shift", Physical Review Letters 111.24 (2013) 1, ISSN: 00319007 (cit. on p. 3).

[82] S. Brakhane, W. Alt, D. Meschede, C. Robens, G. Moon and A. Alberti,
"Note: Ultra-low birefringence dodecagonal vacuum glass cell",
Review of Scientific Instruments 86.12 (2015) 1, ISSN: 10897623 (cit. on pp. 4, 13, 35, 41).

[83] E. L. Raab, M. Prentiss, A. Cable, S. Chu and D. E. Pritchard,
"Trapping of Neutral Sodium Atoms with Radiation Pressure",
Physical Review Letters 59.23 (1987) 2631, ISSN: 00319007, arXiv: arXiv:1009.2475v1
(cit. on p. 4).

[84] D. J. Wineland and W. M. Itano, "Laser cooling", Physics Today 40.6 (1987) 34, ISSN: 19450699
(cit. on p. 4).

[85] T. W. Hänsch and A. L. Schawlow, "Cooling of gases by laser radiation",
Optics Communications 13.1 (1975) 68, ISSN: 00304018 (cit. on p. 4).

[86] D. J. Wineland and H. Dehmelt,
"Proposed laser fluorescence spectroscopy on Tl+ mono-ion oscillator III (sideband cooling)",
Bull. Am. Phys. Soc. 20.637 (1975) (cit. on p. 4).

[87] D. J. Wineland, R. E. Drullinger and F. L. Walls,
"Radiation-pressure cooling of bound resonant absorbers",
Physical Review Letters 40.25 (1978) 1639, ISSN: 00319007 (cit. on p. 4).

[88] P. D. Lett, R. N. Watts, C. I. Westbrook, W. D. Phillips, P. L. Gould and H. J. Metcalf,
"Observation of atoms laser cooled below the doppler limit",
Physical Review Letters 61.2 (1988) 169, ISSN: 00319007 (cit. on p. 4).

[89] J. Dalibard and C. Cohen-Tannoudji,
"Laser cooling below the Doppler limit by polarization gradients: simple theoretical models",
Journal of the Optical Society of America B 6.11 (1989) 2023, ISSN: 0740-3224 (cit. on pp. 4, 6).

[90] C. Salomon, J. Dalibard, W. D. Phillips, A. Clairon and S. Guellatti,
"Laser Cooling of Cesium Atoms below 3μK .", Europhysics Letters 12.8 (1990) 683,
ISSN: 12864854 (cit. on p. 4).

[91] H. J. Metcalf and P. van der Straten, "Laser cooling and trapping of atoms",
Journal of the Optical Society of America B (2003), ISSN: 0740-3224 (cit. on p. 4).

[92] D. S. Weiss, E. Riis, Y. Shevy, P. J. Ungar and S. Chu,
"Optical molasses and multilevel atoms: experiment",
Journal of the Optical Society of America B 6.11 (1989) 2072, ISSN: 0740-3224 (cit. on p. 6).

[93] D. J. Wineland, J. Dalibard and C. Cohen-Tannoudji, "Sisyphus cooling of a bound atom",
Journal of the Optical Society of America B 9.1 (1992) 32, ISSN: 0740-3224 (cit. on p. 7).

[94] J. Hecht, "Short history of laser development", Optical Engineering 49.9 (2010) 091002,
ISSN: 0091-3286 (cit. on p. 7).

[95] A. Alberti, W. Alt, R. Werner and D. Meschede, "Decoherence models for discrete-time
quantum walks and their application to neutral atom experiments",
New Journal of Physics 16.12 (2014) 123052, ISSN: 1367-2630 (cit. on pp. 7, 11, 23, 35, 40, 70).

[96] X. Baillard, A. Gauguet, S. Bize, P. Lemonde, P. Laurent, A. Clairon and P. Rosenbusch,
"Interference-filter-stabilized external-cavity diode lasers", Optics Communications (2006),
ISSN: 00304018, arXiv: 0605046 [physics] (cit. on p. 8).

[97] R. Reimann, "Cooling and Cooperative Coupling of Single Atoms in an Optical Cavity", PhD thesis: University of Bonn, 2015 (cit. on p. 8).

[98] W. Alt, "Optical control of single neutral atoms", PhD Thesis: University of Bonn, 2004 (cit. on p. 8).

[99] C. Wieman and T. W. H??nsch, "Doppler-free laser polarization spectroscopy", Physical Review Letters 36.20 (1976) 1170, ISSN: 00319007 (cit. on p. 8).

[100] M. L. Harris, C. S. Adams, S. L. Cornish, I. C. McLeod, E. Tarleton and I. G. Hughes, "Polarization spectroscopy in rubidium and cesium", Physical Review A - Atomic, Molecular, and Optical Physics 73.6 (2006) 1, ISSN: 10502947, arXiv: 0509157 [physics] (cit. on p. 8).

[101] M. a. Nielsen and I. L. Chuang, *Quantum Computation and Quantum Information: 10th Anniversary Edition*, 2011, ISBN: 1107002176, arXiv: arXiv:1011.1669v3 (cit. on p. 10).

[102] R. Yamamoto, J. Kobayashi, T. Kuno, K. Kato and Y. Takahashi, "An ytterbium quantum gas microscope with narrow-line laser cooling", New Journal of Physics (2016), ISSN: 13672630, arXiv: 1509.03233 (cit. on p. 12).

[103] E. Haller, J. Hudson, A. Kelly, D. A. Cotta, B. Peaudecerf, G. D. Bruce and S. Kuhr, "Single-atom imaging of fermions in a quantum-gas microscope", Nature Physics 11.9 (2015) 738, ISSN: 17452481, arXiv: 1503.02005 (cit. on pp. 12, 71).

[104] L. W. Cheuk, M. A. Nichols, M. Okan, T. Gersdorf, V. V. Ramasesh, W. S. Bakr, T. Lompe and M. W. Zwierlein, "Quantum-gas microscope for fermionic atoms", Physical Review Letters (2015), ISSN: 10797114, arXiv: 1503.02648 (cit. on p. 12).

[105] C. Weitenberg, M. Endres, J. F. Sherson, M. Cheneau, P. Schauss, T. Fukuhara, I. Bloch and S. Kuhr, "Single-spin addressing in an atomic Mott insulator.", Nature 471.7338 (2011) 319, ISSN: 0028-0836, arXiv: 1101.2076 (cit. on pp. 13, 26, 71).

[106] T. Xia, M. Lichtman, K. Maller, A. W. Carr, M. J. Piotrowicz, L. Isenhower and M. Saffman, "Randomized benchmarking of single-qubit gates in a 2D array of neutral-atom qubits", Physical Review Letters 114.10 (2015) 1, ISSN: 10797114, arXiv: 1501.02041 (cit. on pp. 13, 71).

[107] C. Robens, "Testing the Quantumness of Atom Trajectories", PhD thesis: Uni Bonn, 2016 (cit. on pp. 13, 20, 23, 24, 30, 31, 52, 69).

[108] F. Kleißler, "Assembly and Characterization of a High Numerical Aperture Microscope for Single Atoms", Master thesis, 2014 (cit. on p. 13).

[109] R. Winkelmann, "Plane selection", PhD thesis: University of Bonn (cit. on pp. 14, 26, 38, 54, 71).

[110] M. Greiner, O. Mandel, T. Esslinger, T. W. Hänsch and I. Bloch, "Quantum phase transition from a superfluid to a Mott insulator in a gas of ultracold atoms", Nature 415.6867 (2002) 39, ISSN: 00280836 (cit. on p. 15).

[111] H. Häffner, C. F. Roos and R. Blatt, *Quantum computing with trapped ions*, 2008, arXiv: 0809.4368 (cit. on p. 15).

[112] M. Saffman,
"Quantum computing with atomic qubits and Rydberg interactions: progress and challenges",
Journal of Physics B: Atomic, Molecular and Optical Physics 49.20 (2016) 202001,
ISSN: 0953-4075, arXiv: 1605.05207 (cit. on p. 15).

[113] X. Li, "Toward a Neutral Atom Quantum Computer",
PhD thesis: The Pennsylvania State University, 2009 (cit. on p. 15).

[114] A. D. Ludlow, M. M. Boyd, J. Ye, E. Peik and P. O. Schmidt, "Optical atomic clocks",
Reviews of Modern Physics 87.2 (2015) 637, ISSN: 15390756 (cit. on pp. 15, 45).

[115] W. F. McGrew, X. Zhang, R. J. Fasano, S. A. Schäffer, K. Beloy, D. Nicolodi, R. C. Brown,
N. Hinkley, G. Milani, M. Schioppo, T. H. Yoon and A. D. Ludlow,
"Atomic clock performance enabling geodesy below the centimetre level",
Nature 564.7734 (2018) 87, ISSN: 14764687 (cit. on p. 15).

[116] R. Landauer, "Information is inevitably physical", *Feynman and Computation*, 2018 77,
ISBN: 9780429969003 (cit. on p. 15).

[117] G. K. Brennen, C. M. Caves, P. S. Jessen and I. H. Deutsch,
"Quantum logic gates in optical lattices", Physical Review Letters (1999), ISSN: 10797114,
arXiv: 9806021 [quant-ph] (cit. on p. 15).

[118] D. Schrader, S. Kuhr, W. Alt, M. Müller, V. Gomer and D. Meschede,
"An optical conveyor belt for single neutral atoms", Applied Physics B 73.8 (2001) 819,
ISSN: 0946-2171 (cit. on p. 15).

[119] N. Belmechri, L. Förster, W. Alt, A. Widera, D. Meschede and A. Alberti,
"Microwave control of atomic motional states in a spin-dependent optical lattice",
Journal of Physics B: Atomic, Molecular and Optical Physics 46.10 (2013) 104006,
ISSN: 0953-4075, arXiv: arXiv:1302.6208v1 (cit. on pp. 15, 26, 31, 32).

[120] A. Steffen, A. Alberti, W. Alt, N. Belmechri, S. Hild, M. Karski, A. Widera and D. Meschede,
"Digital atom interferometer with single particle control on a discretized space-time geometry",
Proceedings of the National Academy of Sciences 109.25 (2012) 9770, ISSN: 0027-8424,
arXiv: arXiv:1404.3994v1 (cit. on pp. 15, 35).

[121] C. Robens, S. Brakhane, W. Alt, D. Meschede, J. Zopes and A. Alberti,
"Fast, High-Precision Optical Polarization Synthesizer for Ultracold-Atom Experiments",
Physical Review Applied 9.3 (2018) 34016, ISSN: 23317019, arXiv: 1611.07952
(cit. on pp. 15, 20, 21, 23, 24, 43).

[122] R. Grimm, M. Weidemüller and Y. B. Ovchinnikov, "Optical Dipole Traps for Neutral Atoms",
Advances In Atomic, Molecular, and Optical Physics 42 (2000) 95, ISSN: 1049250X
(cit. on pp. 15, 62, 93).

[123] D. Döring, "Ein Experiment zum zustandsabhängigen Transport einzelner Atome",
Diplom thesis: University of Bonn, 2007 (cit. on p. 17).

[124] N. Peter, "Optimal quantum control of atomic wave packets in optical lattices",
PhD thesis: University of Bonn, 2018 (cit. on p. 17).

[125] M. Omar, "Atom cloud compression in a 3D optical lattice and laser intensity stabilisation using
an in-house developed photodiode amplifier", Master thesis: University of Bonn, 2019
(cit. on pp. 20, 22, 69, 71).

[126] M. Werninghaus,
"Controlling atom transport in a two-dimensional state-dependent optical lattice",
Master thesis: University of Bonn, 2017 (cit. on p. 22).

[127] P. Du, "Optical Intensity Control Based on Digital and Analog Systems",
Master thesis: University of Bonn, 2018 (cit. on p. 22).

[128] M. Gehm, K. O'Hara, T. Savard and J. Thomas,
"Dynamics of noise-induced heating in atom traps", Physical Review A 58.5 (1998) 3914,
ISSN: 1050-2947 (cit. on p. 23).

[129] T. Savard, K. O'Hara and J. Thomas,
"Laser-noise-induced heating in far-off resonance optical traps",
Physical Review A 56.2 (1997) R1095, ISSN: 1050-2947 (cit. on p. 23).

[130] S. Kuhr, W. Alt, D. Schrader, I. Dotsenko, Y. Miroshnychenko, A. Rauschenbeutel and
D. Meschede, "Analysis of dephasing mechanisms in a standing-wave dipole trap",
Physical Review A 72.2 (2005) 023406, ISSN: 1050-2947
(cit. on pp. 24, 35, 37, 40, 41, 54, 60, 65).

[131] S. E. Hamann, D. L. Haycock, G. Klose, P. H. Pax, I. H. Deutsch and P. S. Jessen,
"Resolved-Sideband Raman Cooling to the Ground State of an Optical Lattice",
Physical Review Letters 80.19 (1998) 4149, ISSN: 0031-9007, arXiv: 9801025 [quant-ph]
(cit. on p. 26).

[132] A. V. Taichenachev, A. M. Tumaikin, V. I. Yudin and L. Hollberg,
"Two-dimensional sideband Raman cooling and Zeeman state preparation in an optical lattice",
Quantum Electronics and Laser Science Conference (QELS 2000). Technical Digest.
Postconference Edition. TOPS Vol.40 (IEEE Cat. No.00CH37089) (1999) 1, ISSN: 1094-5695,
arXiv: 9911068 [physics] (cit. on p. 26).

[133] D. J. Han, S. Wolf, S. Oliver, C. McCormick, M. T. DePue and D. S. Weiss,
"3D Raman sideband cooling of cesium atoms at high density",
Physical Review Letters 85.4 (2000) 724, ISSN: 00319007 (cit. on p. 26).

[134] A. J. Kerman, V. Vuletić, C. Chin and S. Chu, "Beyond Optical Molasses: 3D Raman Sideband
Cooling of Atomic Cesium to High Phase-Space Density",
Physical Review Letters 84.3 (2000) 439, ISSN: 0031-9007 (cit. on p. 26).

[135] M. F. Parsons, F. Huber, A. Mazurenko, C. S. Chiu, W. Setiawan, K. Wooley-Brown, S. Blatt and
M. Greiner, "Site-Resolved imaging of fermionic li 6 in an optical lattice",
Physical Review Letters 114.21 (2015) 1, ISSN: 10797114, arXiv: 1504.04397 (cit. on p. 26).

[136] X. Li, T. A. Corcovilos, Y. Wang and D. S. Weiss, "3D projection sideband cooling",
Physical Review Letters 108.10 (2012) 1, ISSN: 00319007, arXiv: arXiv:1202.6631v1
(cit. on p. 26).

[137] L. Förster, "Microwave control of atomic motion in a spin dependent optical lattice",
PhD thesis: University of Bonn, 2010 1 (cit. on pp. 27, 31, 69).

[138] D. Leibfried, R. Blatt, C. Monroe and D. Wineland, "Quantum dynamics of single trapped ions",
Review of Modern Physics 75.1 (2003) 281, ISSN: 00346861 (cit. on pp. 30, 31).

[139] Q. A. Turchette, Kielpinski, B. E. King, D. Leibfried, D. M. Meekhof, C. J. Myatt, M. A. Rowe, C. A. Sackett, C. S. Wood, W. M. Itano, C. Monroe and D. J. Wineland, "Heating of trapped ions from the quantum ground state", Physical Review A - Atomic, Molecular, and Optical Physics 61.6 (2000) 8, ISSN: 10941622, arXiv: 0002040 [quant-ph] (cit. on p. 31).

[140] C. Monroe, D. M. Meekhof, B. E. King, S. R. Jefferts, W. M. Itano, D. J. Wineland and P. Gould, "Resolved-sideband Raman cooling of a bound atom to the 3D zero-point energy", Physical Review Letters 75.22 (1995) 4011, ISSN: 00319007 (cit. on p. 33).

[141] E. Torrontegui, S. Ibáñez, X. Chen, A. Ruschhaupt, D. Guéry-Odelin and J. G. Muga, "Fast atomic transport without vibrational heating", Physical Review A - Atomic, Molecular, and Optical Physics 83.1 (2011) 1, ISSN: 10502947, arXiv: 1010.3271 (cit. on p. 33).

[142] M. Schlosshauer, "Decoherence, the measurement problem, and interpretations of quantum mechanics", Reviews of Modern Physics 76.4 (2004) 1267, ISSN: 00346861, arXiv: 0312059 [quant-ph] (cit. on p. 35).

[143] A. W. Young, W. J. Eckner, W. R. Milner, D. Kedar, M. A. Norcia, E. Oelker, N. Schine, J. Ye and A. M. Kaufman, "Half-minute-scale atomic coherence and high relative stability in a tweezer clock", Nature 588.7838 (2020) 408, ISSN: 14764687 (cit. on p. 35).

[144] D. P. DiVincenzo, "The physical implementation of quantum computation", Fortschritte der Physik 48.9-11 (2000) 771, ISSN: 00158208, arXiv: 0002077 [quant-ph] (cit. on p. 35).

[145] T. Calarco, U. Dorner, P. S. Julienne, C. J. Williams and P. Zoller, "Quantum computations with atoms in optical lattices: Marker qubits and molecular interactions", Physical Review A - Atomic, Molecular, and Optical Physics 70.1 (2004) 1, ISSN: 10502947 (cit. on p. 35).

[146] S. Kuhr, W. Alt, D. Schrader, I. Dotsenko, Y. Miroshnychenko, W. Rosenfeld, M. Khudaverdyan, V. Gomer, A. Rauschenbeutel and D. Meschede, "Coherence Properties and Quantum State Transportation in an Optical Conveyor Belt", Physical Review Letters 91.21 (2003) 213002, ISSN: 0031-9007 (cit. on pp. 35, 52).

[147] N. F. Ramsey, "A molecular beam resonance method with separated oscillating fields", Physical Review 78.6 (1950) 695, ISSN: 0031899X (cit. on p. 36).

[148] S. Haroche, M. Brune and J. M. Raimond, "Atomic clocks for controlling light fields", Physics Today 66.1 (2013) 27, ISSN: 00319228 (cit. on p. 36).

[149] M. Karski, "State-selective transport of single neutral atoms", PhD Thesis: University of Bonn, 2010 1 (cit. on pp. 37, 69).

[150] B. Merkel, K. Thirumalai, J. E. Tarlton, V. M. Schäfer, C. J. Ballance, T. P. Harty and D. M. Lucas, "Magnetic field stabilization system for atomic physics experiments", Review of Scientific Instruments 90.4 (2019), ISSN: 10897623, arXiv: 1808.03310 (cit. on p. 38).

[151] A. Kastler, "Displacement of Energy Levels of Atoms by Light", Journal of the Optical Society of America 53.8 (1963) 902, ISSN: 0030-3941 (cit. on p. 40).

[152] Happer1962, "EBective Operator", Physical Review 163.1 (1967) (cit. on p. 40).

[153] N. Nemitz, A. A. Jørgensen, R. Yanagimoto, F. Bregolin and H. Katori, "Modeling light shifts in optical lattice clocks", Physical Review A 99.3 (2019) 1, ISSN: 24699934, arXiv: 1904.06070 (cit. on p. 40).

[154] G. A. Costanzo, S. Micalizio, A. Godone, J. C. Camparo and F. Levi, "Ac Stark shift measurements of the clock transition in cold Cs atoms: Scalar and tensor light shifts of the D2 transition", Physical Review A 93.6 (2016) 1, ISSN: 24699934 (cit. on p. 40).

[155] A. Steffen, W. Alt, M. Genske, D. Meschede, C. Robens and A. Alberti, "Note: In situ measurement of vacuum window birefringence by atomic spectroscopy", *Review of Scientific Instruments*, vol. 84, 12, 2013 12, arXiv: 1308.4959 (cit. on pp. 40–42, 44).

[156] I. H. Deutsch and P. S. Jessen, "Quantum-state control in optical lattices", Physical Review A 57.3 (1998) 1972, ISSN: 1050-2947, arXiv: 9801023 [quant-ph] (cit. on p. 40).

[157] F. Le Kien, P. Schneeweiss and A. Rauschenbeutel, "Dynamical polarizability of atoms in arbitrary light fields: General theory and application to cesium", European Physical Journal D 67.5 (2013), ISSN: 14346060, arXiv: 1211.2673 (cit. on pp. 41, 60).

[158] S. Brakhane and A. Alberti, "Technical Note: Stress-Induced Birefringence in Vacuum Systems", (2016) 6 (cit. on p. 43).

[159] J. Ye, H. J. Kimble and H. Katori, "Quantum state engineering and precision metrology using state-insensitive light traps", Science 320.5884 (2008) 1734, ISSN: 00368075 (cit. on p. 45).

[160] H. Kim, H. S. Han and D. Cho, "Magic polarization for optical trapping of atoms without stark-induced dephasing", Physical Review Letters 111.24 (2013) 1, ISSN: 00319007 (cit. on p. 45).

[161] L. Viola, E. Knill and S. Lloyd, "Dynamical decoupling of open quantum systems", Physical Review Letters 82.12 (1999) 2417, ISSN: 10797114, arXiv: 9809071 [quant-ph] (cit. on p. 52).

[162] W. Yang, Z. Y. Wang and R. B. Liu, "Preserving qubit coherence by dynamical decoupling", Frontiers of Physics in China 6.1 (2011) 2, ISSN: 16733487, arXiv: 1007.0623 (cit. on p. 52).

[163] G. S. Uhrig, "Keeping a quantum bit alive by optimized π-pulse sequences", Physical Review Letters 98.10 (2007) 7, ISSN: 00319007, arXiv: 0609203 [quant-ph] (cit. on p. 52).

[164] D. J. Szwer, S. C. Webster, A. M. Steane and D. M. Lucas, "Keeping a single qubit alive by experimental dynamic decoupling", Journal of Physics B: Atomic, Molecular and Optical Physics 44.2 (2011), ISSN: 09534075, arXiv: 1009.6189 (cit. on p. 52).

[165] Y. O. Dudin, L. Li and A. Kuzmich, "Light storage on the time scale of a minute", Physical Review A - Atomic, Molecular, and Optical Physics 87.3 (2013) 1, ISSN: 10502947 (cit. on p. 52).

[166] B. Naydenov, F. Dolde, L. T. Hall, C. Shin, H. Fedder, L. C. Hollenberg, F. Jelezko and J. Wrachtrup, "Dynamical decoupling of a single-electron spin at room temperature", Physical Review B - Condensed Matter and Materials Physics 83.8 (2011) 1, ISSN: 1550235X, arXiv: 1008.1953 (cit. on p. 52).

[167] M. J. Biercuk, H. Uys, A. P. Vandevender, N. Shiga, W. M. Itano and J. J. Bollinger, "Experimental Uhrig dynamical decoupling using trapped ions", Physical Review A - Atomic, Molecular, and Optical Physics 79.6 (2009) 1, ISSN: 10502947, arXiv: 0902.2957 (cit. on p. 52).

[168] A. Kaplan, M. Fredslund Andersen and N. Davidson, "Suppression of inhomogeneous broadening in rf spectroscopy of optically trapped atoms", Physical Review A 66.4 (2002) 045401, ISSN: 1050-2947, arXiv: 0204082 [physics] (cit. on p. 52).

[169] A. P. Hilton, C. Perrella, A. N. Luiten and P. S. Light, "Dual-color magic-wavelength trap for suppression of light shifts in atoms", Physical Review Applied 11.2 (2019) 1, ISSN: 23317019, arXiv: 1811.04508 (cit. on p. 52).

[170] A. G. Radnaev, Y. O. Dudin, R. Zhao, H. H. Jen, S. D. Jenkins, A. Kuzmich and T. A. Kennedy, "A quantum memory with telecom-wavelength conversion", Nature Physics 6.11 (2010) 894, ISSN: 17452481 (cit. on p. 52).

[171] E. L. Hahn, "Spin echoes", Physical Review 80.4 (1950) 580, ISSN: 0031899X (cit. on p. 52).

[172] M. Anderlini, P. J. Lee, B. L. Brown, J. Sebby-Strabley, W. D. Phillips and J. V. Porto, "Controlled exchange interaction between pairs of neutral atoms in an optical lattice", Nature 448.7152 (2007) 452, ISSN: 14764687 (cit. on pp. 52, 73).

[173] S. Yu, P. Xu, X. He, M. Liu, J. Wang and M. Zhan, "Suppressing phase decoherence of a single atom qubit with Carr-Purcell-Meiboom-Gill sequence", Optics Express 21.26 (2013) 32130, ISSN: 1094-4087 (cit. on p. 52).

[174] M. P. Jones, J. Beugnon, A. Gaëtan, J. Zhang, G. Messin, A. Browaeys and P. Grangier, "Fast quantum state control of a single trapped neutral atom", Physical Review A - Atomic, Molecular, and Optical Physics 75.4 (2007) 1, ISSN: 10502947, arXiv: 0609134 [quant-ph] (cit. on p. 52).

[175] J. Beugnon, C. Tuchendler, H. Marion, A. Gaëtan, Y. Miroshnychenko, Y. R. Sortais, A. M. Lance, M. P. Jones, G. Messin, A. Browaeys and P. Grangier, "Two-dimensional transport and transfer of a single atomic qubit in optical tweezers", Nature Physics 3.10 (2007) 696, ISSN: 17452481, arXiv: 0705.0312 (cit. on p. 52).

[176] M. F. Andersen, A. Kaplan and N. Davidson, "Echo Spectroscopy and Quantum Stability of Trapped Atoms", Physical Review Letters 90.2 (2003) 4, ISSN: 10797114, arXiv: 0208052 [quant-ph] (cit. on p. 52).

[177] D. Schrader, I. Dotsenko, M. Khudaverdyan, Y. Miroshnychenko, A. Rauschenbeutel and D. Meschede, "Neutral atom quantum register", Physical Review Letters 93.15 (2004) 1, ISSN: 00319007, arXiv: 0409037 [quant-ph] (cit. on pp. 54, 55).

[178] A. Mazurenko, S. Blatt, F. Huber, M. F. Parsons, C. S. Chiu, G. Ji, D. Greif and M. Greiner, "Implementation of a stable, high-power optical lattice for quantum gas microscopy", Review of Scientific Instruments 90.3 (2019), ISSN: 10897623, arXiv: 1806.08997 (cit. on p. 59).

[179] G. E. Marti, R. B. Hutson, A. Goban, S. L. Campbell, N. Poli and J. Ye, "Imaging Optical Frequencies with 100 μhz Precision and 1.1 μ m Resolution", Physical Review Letters 120.10 (2018) 103201, ISSN: 10797114 (cit. on p. 59).

[180] A. Steffen, "Single atom interferometers and Bloch oscillations in quantum walks", PhD: University of Bonn, 2013 (cit. on p. 69).

[181] K. K. Chandrashekara, "A high-power Ti:Sa laser system for atomic quantum walks experiments", Master Thesis: University of Bonn, 2020 (cit. on p. 69).

[182] C. F. Roos, A. Alberti, D. Meschede, P. Hauke and H. Häffner, "Revealing Quantum Statistics with a Pair of Distant Atoms", Physical Review Letters 119.16 (2017) 1, ISSN: 10797114, arXiv: 1706.04231 (cit. on pp. 69, 73).

[183] A. Schreiber, P. P. Rohde, K. Laiho, C. Hamilton, I. Jex and C. Silberhorn, "A 2D Quantum Walk Simulation of Two-Particle Dynamics", Science 336.6077 (2012) 55 (cit. on p. 70).

[184] M. R. Lam, N. Peter, T. Groh, W. Alt, C. Robens, D. Meschede, A. Negretti, S. Montangero, T. Calarco and A. Alberti, "Demonstration of Quantum Brachistochrones between Distant States of an Atom", Physical Review X 11.1 (2021) 011035, ISSN: 2160-3308, arXiv: 2009.02231 (cit. on p. 70).

[185] G. J. Edge, R. Anderson, D. Jervis, D. C. McKay, R. Day, S. Trotzky and J. H. Thywissen, "Imaging and addressing of individual fermionic atoms in an optical lattice", Physical Review A - Atomic, Molecular, and Optical Physics 92.6 (2015) 1, ISSN: 10941622, arXiv: 1510.04744 (cit. on p. 71).

[186] J. F. Sherson, C. Weitenberg, M. Endres, M. Cheneau, I. Bloch and S. Kuhr, "Single-atom-resolved fluorescence imaging of an atomic Mott insulator.", Nature 467.7311 (2010) 68, ISSN: 0028-0836, arXiv: arXiv:1006.3799v1 (cit. on p. 71).

[187] O. Elíasson, J. S. Laustsen, R. Heck, R. Müller, J. J. Arlt, C. A. Weidner and J. F. Sherson, "Spatial tomography of individual atoms in a quantum gas microscope", Physical Review A 102.5 (2020) 1, ISSN: 24699934, arXiv: 1912.03079 (cit. on p. 71).

[188] S. R. P. Pavani, M. A. Thompson, J. S. Biteen, S. J. Lord, N. Liu, R. J. Twieg, R. Piestun and W. E. Moerner, "Three-dimensional, single-molecule fluorescence imaging beyond the diffraction limit by using a double-helix point spread function", Proceedings of the National Academy of Sciences of the United States of America 106.9 (2009) 2995, ISSN: 00278424 (cit. on p. 71).

[189] C. Zhang, S. L. Rolston and S. Das Sarma, "Manipulation of single neutral atoms in optical lattices", Physical Review A 74.4 (2006) 42316, ISSN: 10502947 (cit. on p. 71).

[190] D. Viscor, J. L. Rubio, G. Birkl, J. Mompart and V. Ahufinger, "Single-site addressing of ultracold atoms beyond the diffraction limit via position-dependent adiabatic passage", Physical Review A - Atomic, Molecular, and Optical Physics 86.6 (2012) 1, ISSN: 10502947 (cit. on p. 71).

[191] D. Ohl de Mello, D. Schäffner, J. Werkmann, T. Preuschoff, L. Kohfahl, M. Schlosser and G. Birkl, "Defect-Free Assembly of 2D Clusters of More Than 100 Single-Atom Quantum Systems", Physical Review Letters 122.20 (2019) 203601, ISSN: 0031-9007 (cit. on p. 71).

[192] M. Endres, H. Bernien, A. Keesling, H. Levine, E. R. Anschuetz, A. Krajenbrink, C. Senko, V. Vuletic, M. Greiner and M. D. Lukin, "Atom-by-atom assembly of defect-free one-dimensional cold atom arrays", Science 354.6315 (2016) 1024, ISSN: 10959203 (cit. on p. 71).

[193] S. A. Moses, J. P. Covey, M. T. Miecnikowski, D. S. Jin and J. Ye, "New frontiers for quantum gases of polar molecules", Nature Physics 13.1 (2017) 13, ISSN: 17452481, arXiv: 1610.07711 (cit. on p. 71).

[194] P. T. Brown, D. Mitra, E. Guardado-Sanchez, R. Nourafkan, A. Reymbaut, C.-D. Hébert, S. Bergeron, A.-M. S. Tremblay, J. Kokalj, D. A. Huse, P. Schauß and W. S. Bakr, "Bad metallic transport in a cold atom Fermi-Hubbard system", Science 363.6425 (2019) 379, ISSN: 0036-8075 (cit. on p. 71).

[195] M. A. Nichols, L. W. Cheuk, M. Okan, T. R. Hartke, E. Mendez, T. Senthil, E. Khatami, H. Zhang and M. W. Zwierlein, "Quantum simulation: Spin transport in a Mott insulator of ultracold fermions", Science 363.6425 (2019) 383, ISSN: 10959203 (cit. on p. 71).

[196] B. Yang, H. Sun, C. J. Huang, H. Y. Wang, Y. Deng, H. N. Dai, Z. S. Yuan and J. W. Pan, "Cooling and entangling ultracold atoms in optical lattices", Science 369.6503 (2020) 550, ISSN: 10959203, arXiv: 1901.01146 (cit. on p. 71).

[197] L. Isenhower, E. Urban, X. L. Zhang, A. T. Gill, T. Henage, T. A. Johnson, T. G. Walker and M. Saffman, "Demonstration of a Neutral Atom Controlled-NOT Quantum Gate", Physical Review Letters 104.1 (2010) 010503, ISSN: 0031-9007 (cit. on p. 71).

[198] F. Schäfer, T. Fukuhara, S. Sugawa, Y. Takasu and Y. Takahashi, "Tools for quantum simulation with ultracold atoms in optical lattices", Nature Reviews Physics 2.8 (2020) 411, ISSN: 25225820, arXiv: 2006.06120 (cit. on p. 71).

[199] J. K. Asboth and J. M. Edge, "Edge-state-enhanced transport in a two-dimensional quantum walk", Physical Review A 91.2 (2015) 022324, ISSN: 1050-2947 (cit. on p. 72).

[200] M. S. Rudner, N. H. Lindner, E. Berg and M. Levin, "Anomalous edge states and the bulk-edge correspondence for periodically driven two-dimensional systems", Physical Review X 3.3 (2014) 1, ISSN: 21603308, arXiv: arXiv:1212.3324v1 (cit. on p. 72).

[201] J. K. Asbóth, L. Oroszlány and A. Pályi, *A Short Course on Topological Insulators*, vol. 919, Lecture Notes in Physics, Cham: Springer International Publishing, 2016, ISBN: 978-3-319-25605-4, arXiv: 1509.02295 (cit. on p. 72).

[202] S. De Léséleuc, V. Lienhard, P. Scholl, D. Barredo, S. Weber, N. Lang, H. P. Büchler, T. Lahaye and A. Browaeys, "Observation of a symmetry-protected topological phase of interacting bosons with Rydberg atoms", Science 365.6455 (2019) 775, ISSN: 10959203 (cit. on p. 73).

[203] X. Chen, Z. C. Gu, Z. X. Liu and X. G. Wen, "Symmetry-protected topological orders in interacting bosonic systems", Science 338.6114 (2012) 1604, ISSN: 10959203, arXiv: 1301.0861 (cit. on p. 73).

[204] A. C. Potter, T. Morimoto and A. Vishwanath, "Classification of Interacting Topological Floquet Phases in One Dimension", Physical Review X 6.4 (2016) 041001, ISSN: 2160-3308 (cit. on p. 73).

[205] R. Roy and F. Harper, "Abelian Floquet symmetry-protected topological phases in one dimension", Physical Review B 94.12 (2016) 125105, ISSN: 2469-9950 (cit. on p. 73).

[206] S. Aaronson and A. Arkhipov, "The Computational Complexity of Linear Optics", Theory of Computing 9.1 (2013) 143, ISSN: 1557-2862 (cit. on p. 73).

[207] H.-S. Zhong, H. Wang, Y.-H. Deng, M.-C. Chen, L.-C. Peng, Y.-H. Luo, J. Qin, D. Wu, X. Ding, Y. Hu, P. Hu, X.-Y. Yang, W.-J. Zhang, H. Li, Y. Li, X. Jiang, L. Gan, G. Yang, L. You, Z. Wang, L. Li, N.-L. Liu, C.-Y. Lu and J.-W. Pan, "Quantum computational advantage using photons.", Science 370.6523 (2020) 1460, ISSN: 1095-9203 (cit. on p. 73).

[208] H. J. Briegel and R. Raussendorf, "Persistent Entanglement in Arrays of Interacting Particles", Physical Review Letters 86.5 (2001) 910, ISSN: 0031-9007 (cit. on p. 73).

[209] J. I. Cirac and P. Zoller, "How to manipulate cold atoms", Science 301.5630 (2003) 176, ISSN: 00368075 (cit. on p. 73).

[210] R. Raussendorf and H. J. Briegel, "A one-way quantum computer", Physical Review Letters 86.22 (2001) 5188, ISSN: 00319007 (cit. on p. 73).

APPENDIX A

Hamiltonian of the 2D state-dependent optical lattice

As discussed in Chapter 3, our 2D state-dependent optical lattice can be decomposed into a two sub-lattices, each trapping atoms in state $|\uparrow\rangle$ or $|\downarrow\rangle$. The lattice is constructed by the interference of three beams, two of which (called HDT1 and HDT3) are polarization synthesized, while the third (HDT2) is fixed in polarization (see Figure 3.2). The Hamiltonians for the $|\uparrow\rangle$ and $|\downarrow\rangle$ system are

$$H_{\uparrow}(x,p) = \frac{p^2}{2m} - U_0\Bigg(\frac{3 + 2\cos(\phi_{1,\sigma^+} - \phi_{3,\sigma^+} + 4\pi x/\lambda_L) + 2\cos[\phi_{1,\sigma_+} + 2\pi(x-y)/\lambda_L]}{9} + \frac{2\cos[\phi_{3,\sigma_+} + 2\pi(x+y)/\lambda_L]}{9}\Bigg) \tag{A.1}$$

$$H_{\downarrow}(x,p) = \frac{p^2}{2m} - U_0\Bigg(\frac{12 + \cos(\phi_{1,\sigma^+} - \phi_{3,\sigma^+} + 4\pi x/\lambda_L) + 7\cos(\phi_{1,\sigma^-} - \phi_{3,\sigma^-} + 4\pi x/\lambda_L)}{36} + \frac{\cos[\phi_{1,\sigma^+} + 2\pi(x-y)/\lambda_L] + 7\cos[\phi_{1,\sigma^-} + 2\pi(x-y)/\lambda_L]}{36} + \frac{\cos[\phi_{3,\sigma^+} - 2\pi(x+y)/\lambda_L] + 7\cos[\phi_{3,\sigma^-} - 2\pi(x+y)/\lambda_L]}{36}\Bigg) \tag{A.2}$$

where U_0 is the trap depth, λ_L the lattice wavelength, m the mass of the cesium atom, p the momentum, and x and y the position. The angles ϕ_{1,σ^+} and ϕ_{1,σ^-} correspond to the phases of the $\sigma^{+,-}$ components of HDT1 and ϕ_{3,σ^+} and ϕ_{3,σ^-} to those of HDT3 (see Figure 3.2). When all angles are zero, the two potentials are overlapped and the Hamiltonians are identical, corresponding to the expression in Eq. 3.6.

APPENDIX B

Derivation of η_v, the sensitivity of the Ramsey imaging technique

Following equation (19) in [122], the potential of a ground state with total angular momentum F and magnetic quantum number m_F, for a laser beam with intensity $I(\vec{r})$ and frequency ν is given by:

$$U(\vec{r}) = \alpha\left(\frac{2 + Pg_F m_F}{\nu - \nu_2} + \frac{1 - Pg_F m_F}{\nu - \nu_1}\right)I(\vec{r})$$
$$\text{where} \quad \alpha = \frac{c^2\Gamma_1}{32\pi^3\nu_1^3} \approx \frac{c^2\Gamma_2}{32\pi^3\nu_2^3} \tag{B.1}$$

The expression is valid for both linear and circular polarization, with P characterizing the laser polarization (P=0,±1 for linearly and circularly $\sigma^{\pm}$ polarized light). g_F is the Landé factor, ν_1 and ν_2 the frequencies of the D1 and D2 transitions, c the speed of light, and Γ_1 (Γ_2) the natural line widths of the D1 (D2) transition.

The potential, expressed in terms of the right and left-circularly polarized components of a linearly polarized dipole trap beam is

$$U(\vec{r}) = \alpha\left[\left(\frac{2 + g_F m_F}{\nu - \nu_2} + \frac{1 - g_F m_F}{\nu - \nu_1}\right)I_R(\vec{r}) + \left(\frac{2 - g_F m_F}{\nu - \nu_2} + \frac{1 + g_F m_F}{\nu - \nu_1}\right)I_L(\vec{r})\right] \tag{B.2}$$

The light shift δ_{LS} between the two states $|\uparrow\rangle$ and $|\downarrow\rangle$ is the difference between the two potential for the respective states

$$\delta_{LS} = \frac{U_{\uparrow}(\vec{r}) - U_{\downarrow}(\vec{r})}{h} \tag{B.3}$$

where h is the Plank constant. Plugging in expression B.2, the light shift can be expressed as

$$\delta_{LS} = -\frac{(I_L(\vec{r}) - I_R(\vec{r}))(g_F m_F - g'_F m'_F)(\nu_1 - \nu_2)\alpha}{h(\nu - \nu_1)(\nu - \nu_2)} \tag{B.4}$$

where g_F (g'_F) and m_F (m'_F) are the Landé factor and magnetic quantum number for $|\downarrow\rangle$ ($|\uparrow\rangle$).

From Chapter 5, we know the relation between the light shift and the trapping potential U($\vec{r}$) experienced

by atoms

$$\delta_{LS} = \frac{\epsilon \eta_v U(\vec{r})}{h}$$
$$\text{where} \quad \epsilon = \frac{I_R(\vec{r}) - I_L(\vec{r})}{I_R(\vec{r}) + I_L(\vec{r})} = \frac{I_R(\vec{r}) - I_L(\vec{r})}{I(\vec{r})} \tag{B.5}$$

$U(\vec{r})$ can be written in terms of Eq. B.2, with $I_R(\vec{r}) = I_L(\vec{r}) = I(\vec{r})/2$ (for the linearly incident dipole beam). Substituting the value of $U(\vec{r})$ and δ_{LS} in Eq. B.5, one arrives at the expression for the sensitivity

$$\eta_v = (g'_F m'_F - g_F m_F) \frac{\nu_2 - \nu_1}{3\nu - 2\nu_1 - \nu_2}, \tag{B.6}$$

APPENDIX C

Uncertainty in determining the phase ϕ of a Ramsey fringe

In this section, I will derive the expression for the uncertainty in determining the phase ϕ of a Ramsey fringe, modeled as

$$f(S, C, \phi) = \frac{S}{2}(1 + C\cos(\phi_{mw}(i) - \phi)) \tag{C.1}$$

where S is the probability of survival of the atoms in the trap while performing the measurement, C is the contrast and ϕ the phase of the Ramsey fringe, and $\phi_{mw}(i)$ is the x-value of the i^{th} data point. When fitting the model in Eq. C.1 to M data values y_m, we minimize the expression

$$\chi^2 = \sum_{m=1}^{M} \left(\frac{y_m - f(S, C, \phi)_m}{\sigma_m} \right)^2 \tag{C.2}$$

which is equivalent to maximizing the 'likelihood function' (for Gaussian uncertainties). Here, χ^2 is our likelihood estimator and σ_m is the error for each data value. On performing a Taylor series expansion of Eq. C.1 around the minima (S_0, C_0 and ϕ_0) and substituting in Eq. C.2, χ^2 is rewritten as

$$\chi^2 = \sum_{m=1}^{M} \frac{((1/2)(-S - (C_0(S - S_0) + CS_0)\cos[\phi_0 - \phi_{mw}(m)] - C_0 S_0(-\phi - \phi_0)\sin[\phi_0 - \phi_{mw}(m)]) + y_m)^2}{\sigma_m^2} \tag{C.3}$$

Our function is parameterized by the three variables: S, C and ϕ. We are interested in the variance σ_ϕ^2 of the Ramsey phase. The likelihood function can be related to the χ^2 through

$$\chi^2(\phi) = -2\ln \mathcal{L}(\phi) + const. \tag{C.4}$$

The Cramér-Rao bound gives the lower bound of the variance of the estimator

$$\sigma_\phi^2 \geq \frac{1}{I(\phi)} \tag{C.5}$$

where $I(\phi)$ is the Fisher information

$$I(\phi) = \frac{1}{E\left[-\frac{\partial^2 \ln \mathcal{L}}{\partial^2 \phi} \right]} \tag{C.6}$$

For a large number of observations, $E\left[-\frac{\partial^2 \ln \mathcal{L}}{\partial^2 \phi}\right] \sim -\left.\frac{\partial^2 \ln \mathcal{L}}{\partial^2 \phi}\right|_{\phi_0}$. Therefore, the lower bound of the variance of the phase extracted from the Ramsey fringe fit is:

$$\begin{aligned}\sigma_\phi^2 &= \frac{2}{\left.\frac{\partial^2 \chi^2}{\partial \phi^2}\right|_{\phi_0}} \\ &= \frac{2}{\sum_{m=1}^{M} \frac{C_0^2 S_0^2 \sin[\phi_0 - \phi_{mw}(m)]^2}{2\sigma_m^2}}\end{aligned} \tag{C.7}$$

Here we make some assumptions to simplify the expression. Firstly, we assume that the background survival S_0 is 1. Such an assumption is realistic since the lifetime of atoms in the trap is in tens of seconds while the Ramsey experiments are typically conducted within a few milliseconds. Next we can convert the sum to an integral with the appropriate prefactors, $\sum_{m=1}^{M} \leftarrow \frac{M}{2\pi}\int_0^{2\pi} dm$. Finally, we model the noise for each data point [51]

$$\sigma_m = \sqrt{\frac{f(S,C,\phi) * (1 - f(S,C,\phi))}{n} + \frac{1}{\gamma n} + \frac{b^2}{\gamma^2 n^2}} \tag{C.8}$$

where n is the total number or measurements performed per data point, γ is the number of pre-amplified photoelectrons per atom imaged and b is the background pixel noise. Plugging this value of σ_m into Eq. C.7 and performing the integration, we can express the variance of the phase extracted from fitting the Ramsey fringe:

$$\sigma_\phi^2 = \frac{1}{Mn\left(1 - \sqrt{\frac{4b^2 + n\gamma(4+\gamma-C_0^2\gamma)}{4b^2+n\gamma(4+\gamma)}}\right)} \tag{C.9}$$

As expected, the higher the number of measurements, the smaller the uncertainty gets. Furthermore, the above expression also emphasizes the dependence on the contrast of the fringe, with lowest uncertainty when $C_0 = 1$.

Acknowledgements

I am indebted to many people for the very exciting, fun and fruitful time I had over the course of this PhD. I am sure that I will inevitably forget to thank a lot of people for their help, friendship and guidance during different periods of my PhD, I'm sorry for that. However, for the names that I do mention, I confess that it is near impossible to express all my gratitude in just these few paragraphs; I will try nonetheless.

First of all, I would like to thank Prof. Dr. Dieter Meschede for giving me the opportunity to pursue a PhD in his very friendly, diverse, and extremely motivated research group. I sincerely thank him for his guidance and motivation, particularly when things seemed bleak, and for his commitment to every group member's well-being.

A special thanks goes to Dr. Andrea Alberti, who has guided the DQSIM project through thick and thin, for his direct supervision and his contagious enthusiasm to try new things. His deep understanding of theoretical concepts and an insatiable hunger for physics, though at times unnerving, has mostly been a great source of inspiration. I would also like to thank Dr. Wolfgang Alt who, with his large reservoir of technical and scientific knowledge, almost always had a solution ready for the various problems we used to run to him with, saving us many hours of debugging in the lab. His ability to always be able to formulate simple arguments to explain complex topics reflects his deep understanding of the subject.

This PhD would not have been possible without the wonderful team I had the pleasure of working with. I would like to thank Stefan and Geol Moon for introducing me to the state-of-the-art DQSIM experiment, which they had so laboriously built up. I would like to thank Richard, who joined the team around the same time as me, for working together on the experiment and always ready to help, both in the lab and outside. I would also like to thank Peng Xu, who in spite of running his own research group back in Wuhan, was fully immersed in the DQSIM experiment. The DQSIM experiment, and in turn I, benefited a lot from the contribution of our tireless and motivated masters students: Max, Peng Du, Muhib and Karthik. For that, I would like to sincerely thank them, and wish them all the best for their own PhD projects.

Lab work can at times get frustrating. The best way to deal with it was to join the other frustrated people in the office. The office was a very special place; it was like being part of a family. I would like to thank all the office mates I had over the years for all the fun times we had in (and outside) the office: Carsten, Stefan, Moon, Jose, Tobi, Max, Richard, Muhib and Karthik. I also want to thank the other group members who were always ready to help and with whom I shared some good times outside the lab: Manolo, Eduardo, Sajid, Deepak, Miguel, Lukas, Pooja...

Our experiments would not have been possible without the support of the administration and the mechanical workshop. I want to sincerely thank Dietmar, Fien, and Annelise for taking care of all the administrative work. I would like to thank Herr Kalb for all the help with soldering and PCB printing, and Herr Brähler for helping with electronics.

My stay in Bonn would not have been half as nice, without the company of my friends, with whom I share so many happy memories. For this I would like to thank Hans (whom I've known the longest in Germany, and spent many new year's eves with, from that piece of 'modern art' we left on the sheet

of snow in Berlin to nearly being shot down by hunters in Nice), Jose (for all the engaging discussions, sometimes ending with the 'no. of documentaries watched' criteria, and for giving in and letting me drive for those five minutes in Sardinia, where Hans thought we were done for), Joseph (for all those *dum biryani* cooking sessions followed by the movies you slept through), Karthik (for all the interesting lunchtime chats), Manolo (for the long weekend bike rides where I discovered how beautiful this region is), Max (for all the goofing around in the office), Geol Moon (our in house K-pop sensation), Nabhojeet (who single-handedly ripped apart my old kitchen), Ripunjay (for long chats over coffee at BCP), and Tobi (for your sage financial advice; with all the money saved we should really get a GoPro that works when we need it to).

I am extremely lucky to have met Maitraiyee in Bonn; she has been the most thoughtful, loving and supportive partner I could have hoped for. Thank you for bearing with my erratic lab schedule and for visiting me twice (against all odds) during the last year to help me past the finish line. I am really looking forward to many more hiking adventures (without shortcuts) and vacations (where I help with some planning as well) with you.

Lastly, I would like to thank my wonderful family. I thank my parents for their unconditional love and all their sacrifices. I thank my sister for being very supportive, and always being able to lift my spirits. I also want to thank the rest of my family for their support throughout all these years, particularly Aditi, whom I visited at least once every year for her meticulously planned vacations, and Kabir, for his guidance over the years.